
Mode Locked Fiber Lasers: Theoretical and Experimental Developments

Carsten Krogh Nielsen

Department of Physics and Astronomy
University of Aarhus, Denmark

PhD thesis
December 2006

This thesis is submitted to the Faculty of Science at the University of Aarhus, Denmark, in order to fulfill the requirements for obtaining the PhD degree in Physics. The studies have been carried out under the supervision of Prof. Søren Rud Keiding.

Contents

Preface	v
Acknowledgments	vi
List of Publications	vii
1 Introduction	1
1.1 Mode-locked lasers	1
1.2 Fiber lasers	2
1.3 Photonic Crystal Fibers	3
1.4 Challenges of mode-locked fiber laser systems	4
Outline of the thesis	5
2 The Nonlinear Schrödinger Equation	7
2.1 Introduction	8
2.2 The nonlinear Schrödinger equation	8
2.2.1 The nonlinear Schrödinger equation in frequency domain	11
2.2.2 The nonlinear Schrödinger equation in time domain: . . .	12
2.2.3 Nonlinearities	13
2.2.4 Two polarization states	13
2.3 Analytical solutions	15
2.3.1 Dispersion	15
2.3.2 Self-phase modulation	16
2.3.3 Nonlinear polarization rotation	16
2.3.4 Soliton	18
2.3.5 Stimulated Raman Scattering	18
2.4 Numerical algorithm	19
3 Simulation of fiber lasers	21
3.1 Introduction	22
3.2 Gain medium	22

3.2.1	Ytterbium	23
3.3	Mode-locking mechanisms	24
3.3.1	Nonlinear polarization rotation	24
3.3.2	SESAM	24
3.4	Cavity losses	26
3.5	Laser cavity simulations	27
3.6	Numerical simulations of a 80 MHz fiber laser	28
4	Characterization techniques	33
	Measurement of fiber dispersion	34
4.1	Introduction	34
4.2	Experimental setup	35
4.3	Theory	36
4.4	Dispersion measurements	38
	Autocorrelation measurements	42
4.5	Introduction	42
4.6	Setup and theory	42
	Measurement of group birefringence	46
4.7	Polarization maintaining fibers	46
4.8	Measurement of the group birefringence	47
4.9	Summary	48
5	Solid core photonic bandgap fiber laser	49
5.1	Introduction	50
5.2	Fiber characterization	51
5.3	Laser design	52
5.4	Experimental results	54
5.5	Numerical simulations	56
5.6	Outlook	58
5.7	Summary	59
6	Self-similar all-polarization maintaining environmentally stable fiber laser	61
6.1	Introduction	62
6.2	Cavity design	64
6.3	Experimental results	66
6.3.1	Bound states	68
6.4	Outlook	70
6.5	Summary	70
7	Microjoule-level all polarization-maintaining femtosecond fiber source	71
7.1	Introduction	72
7.2	Theory	74
7.3	Experimental setup	80
7.4	Experimental results	81

7.5	Outlook	84
7.6	Summary	85
8	Dispersion compensation free mode-locked fiber laser and supercontinuum generation	87
8.1	Introduction	88
8.2	Experimental setup and results	89
8.3	Supercontinuum generation with a dispersion compensation free setup.	91
8.4	Outlook	93
8.5	Summary	94
9	Environmentally stable low repetition rate nonlinear polarization rotation based fiber laser	95
9.1	Introduction	96
9.2	Faraday mirror	98
9.3	Proposed laser configuration	101
9.4	Startup of mode-locked lasing	102
9.5	Experimentally implemented laser configuration	104
9.6	Experimental results	105
9.6.1	Amplification and supercontinuum generation	107
9.7	Numerical model and simulations	109
9.8	Intra cavity Raman continuum generation	114
9.9	All-polarization maintaining fiber laser	116
9.9.1	Experimental setup and results	118
9.10	Summary	120
9.11	Outlook	120
10	Summary and perspectives	121
	Bibliography	125

Preface

My interest in fiber lasers began roughly one year before starting as a Ph.D. student under the supervision of Prof. Søren Rud Keiding. I attended a lecture held by John Erland Østergaard from NKT and was intrigued by the close connection between the interesting physics and real life applications related to optical fibers. I soon became an active part of the femtogroup at The University of Aarhus, which besides Søren also included Jakob Juul Larsen (employed by NKT, and posted in Aarhus), Jan Thøgersen (TAP at The University of Aarhus) and the three Ph.D. students Henrik N. Paulsen, Karen M. Hilligsøe and Thomas V. Andersen. My interest in ultrafast phenomena related to optical fibers was further stimulated, as we went through the book, "Nonlinear Fiber Optics" by Agrawal [1] equation by equation. It was at that time I accepted to work on this Ph.D. project. The project is a collaboration between The University of Aarhus and the NKT-Photonics group. NKT-Photonics is a constellation of relatively small spin-off companies of which three have been relevant for this work: Koheras, Crystal Fibre and NKT-Research & Innovation (NKT-Research). Koheras primarily produces cw fiber laser with ultra narrow line widths. Crystal Fibre manufactures photonic crystal fibers. NKT-Research carries out relevant basic research to support further development of the companies within the NKT-Photonics group. My primary contact has been with NKT-Research, and more specifically, Claus Friis Pedersen, although I have worked together with many others at both Koheras, Crystal Fibre and NKT-Research. The NKT-Photonics adventure really took off in the year 2000 when the NKT-owned spin-off company, Giga was sold to Intel for about 1.3 billion Euros. A large amount of this money were reinvested into fundamental research. NKT-Academy was founded and numerous photonics-related Ph.D. projects were initiated in Denmark and abroad. The focus of my Ph.D. project was the development of new mode-locked fiber lasers. Neither NKT nor the group at the University of Aarhus had any prior knowledge of the development of such fiber lasers, but saw the rapid development of applications combined with exciting technologies at NKT as an potential future income. The focus at NKT was further moved into applications of mode-locked lasers at the collapse of the telecommunication market. Today the product of

perhaps biggest economic potential in NKT is their high average power supercontinuum white light source, based on an amplified mode-locked fiber laser and supercontinuum generation in nonlinear photonic crystal fibers.

During the Ph.D. project, the main part of the time was spent in Aarhus. However, at numerous occasions, I also visited and worked at NKT in Birkerød. Especially the lack of a fusion splicer for polarization maintaining fibers in Aarhus, where most of the tests on the mode-locked fiber lasers were carried out, resulted in many trips to NKT. In the summer of 2005, I was also fortunate enough to gain experience from working together with Jens Limpert and Thomas Schreiber in their group at the University of Jena, Germany.

Acknowledgments

During my time as a Ph.D student at the University of Aarhus, I've had a great time, and really enjoyed the versatile and interesting job, from which I have gained much experience - both on a theoretical, technical and personal level. There are many people that I would like to acknowledge for this time. I would like to thank my supervisor, Prof. Søren Rud Keiding for giving me the possibility of working with such an interesting field as fiber lasers, and giving me room to chose my own direction within this field. Further I've learned from Søren that it is important always to pay interest to broader research fields than just ones own. During my first years in the group, Jakob Juul Larsen was a great help in introducing me to all basic optics and ultrafast lasers, and further Jakob endured many hours of listening to my crazy ideas. Jakob functioned as external supervisor for the NKT-Academy students in Aarhus for about two years and was an enormous help for all of us. Jan Thøgersen has also always been a great help in the lab, and contributed with his huge knowledge of lasers.

The femtogroup have included many people over the years, and the spirits have always been high. This has helped in creating an pleasant and inspiring environment. Especially my co-worker, Thomas V. Andersen, has contributed with his outstanding drive and work moral. Also special thanks to Jakob Juul Larsen and Victoria Birkedal for proof-reading this thesis.

I also acknowledge the helpfulness of the people at NKT Research, Crystal Fibre and Koheras, and special thanks to Claus Friis Pedersen for his support and engagement in the work in Aarhus.

Finally, I would like to thank my wife, Lene, for supporting me through out my time as a Ph.D student, and for making it possible to have both long working hours and a well functioning family. Especially during the last year where we got our little daughter, and every thing had to be done by a tight schedule, she has made a great effort in making everything run smoothly.

List of Publications

Journal papers

- [I] K. M. Hilligsøe, T. V. Andersen, H. N. Paulsen, C. K. Nielsen, K. Mølmer, S. R. Keiding, R. Kristensen, K. P. Hansen, J. J. Larsen, "Supercontinuum generation in a photonic crystal fiber with two zero dispersion wavelengths", *Opt. Expr.*, **12**, no. 6, 1045-1054 (2004)
- [II] T. V. Andersen, K. M. Hilligsøe, C. K. Nielsen, J. Thøgersen, K. P. Hansen, S. R. Keiding, and J. J. Larsen, "Continuous-wave wavelength conversion in a photonic crystal fiber with two zero-dispersion wavelengths", *Opt. Expr.*, **12**, no. 17, 4113-4122 (2004)
- [III] T. V. Andersen, K. M. Hilligsøe, C. K. Nielsen, J. Thøgersen, K. P. Hansen, S. R. Keiding, and J. J. Larsen, "Continuous-wave wavelength conversion in a photonic crystal fiber with two zero-dispersion wavelengths (vol 12, pg 4113, 2004)", *Opt. Expr.*, **13**, no. 9, 3581-3582 (2005)
- [IV] C. K. Nielsen, T. V. Andersen, S. R. Keiding, "Stability Analysis of an All-fiber Coupled Cavity Fabry-Perot Additive Pulse Mode-Locked laser" *IEEE J. Q. Electr.*, **41**, no. 2, 198-204 (2005)
- [V] C. K. Nielsen, B. Ortaç, T. Schreiber, J. Limpert, R. Hohmuth, W. Richter, A. Tünnermann, "Self-starting self-similar all-polarization maintaining Yb-doped fiber laser", *Opt. Expr.*, **13**, no. 23, 9346-9351 (2005)
- [VI] T. Schreiber, C. K. Nielsen, B. Ortaç, J. Limpert, A. Tünnermann, " μ J-Level all-polarization-maintaining femtosecond fiber source.", *Opt. Lett.*, **31**, no. 5, 574-576 (2006)
- [VII] C. K. Nielsen, K. G. Jespersen, and S. R. Keiding, "A 158 fs 5.3 nJ fiber-laser system at 1 μ m using photonic bandgap fibers for dispersion control and pulse compression.", *Opt. Expr.*, **14**, no. 13, 6063-6068 (2006)

- [VIII] E. R. Andresen C. K. Nielsen, J. Thøgersen, and S. R. Keiding, "Fiber laser system for CARS microscopy.", In preparation.
- [IX] C. K. Nielsen and S. R. Keiding, "Environmentally stable all-fiber non-linear polarization rotation based mode-locked fiber laser.", submitted to *Opt. Lett.*

Conference papers

- [X] C. K. Nielsen, T. V. Andersen, E. Riis, A. Petersson, J. Broeng "Investigations of the coupling between the core mode and cladding modes in a double clad Yb-doped photonic crystal fiber" in *Proceedings of the 2004 Photonics West Conference, California USA*, no. 5335-26.
- [XI] K. M. Hilligsøe, T. V. Andersen, H. N. Paulsen, C. K. Nielsen, K. Mølmer, S. R. Keiding, K. P. Hansen, J. J. Larsen "Supercontinuum generation in a photonic crystal fiber with two closely lying zero dispersion wavelengths", *OSA Trends in Optics and Photonics Series 96 A*, p1567-1568
- [XII] K. M. Hilligsøe, T. V. Andersen, H. N. Paulsen, C. K. Nielsen, K. Mølmer, S. R. Keiding, K. P. Hansen, J. J. Larsen "Supercontinuum generation in a photonic crystal fiber with two closely lying zero dispersion wavelengths", *Conference on Lasers and Electro-Optics (CLEO)*, 1 p2 (2004)
- [XIII] C. K. Nielsen, B. Ortaç, T. Schreiber, J. Limpert, R. Hohmuth, W. Richter, A. Tünnermann, "Single pulse and bound state operation of a self-starting self-similar all-PM yb-doped fiber laser", *Proceedings of the 2006 Photonics West Conference, California USA* no. 6102-17
- [XIV] T. Schreiber, C. K. Nielsen, B. Ortaç, J. Limpert, A. Tünnermann, "μJ-Level all-polarization-maintaining femtosecond fiber laser.", ASSP Jan. 2006
- [XV] T. Schreiber, B. Ortaç, C. K. Nielsen, J. Limpert, A. Tünnermann, "Compact uJ-level all-polarization maintaining femtosecond fiber source", *Proceedings of the 2006 Photonics West Conference, California USA* no. 6102-11
- [XVI] C. K. Nielsen, K. G. Jespersen, T. V. Andersen, S. R. Keiding, "Dispersion compensation with solid-core photonic bandgap fiber in an yb doped mode-locked fiber laser", *Proceedings of the 2007 Photonics West Conference, California USA* no. 6453-23

Patents

- [XVII] C. K. Nielsen, "Environmentally stable all-fiber self-starting mode-locked fiber laser", Patent pending, EP05009990.2
- [XVIII] T. Schreiber, C. K. Nielsen, B. Ortaç, J. Limpert, A. Tünnermann, "Stabiler Modengekoppelter Kurzpuls-Faserlaser mit polarisationserhaltenden Fasern und sättigbarem Halbleiterspiegel", Patent pending, 05F46545-IOF

CHAPTER 1

Introduction

Ultrafast optics have for decades been a very rich research field, and today short pulsed laser systems find numerous applications in areas of fundamental research as well as for medical and industrial applications. For example ultrafast laser systems are used for time resolved studies in chemistry [2], optical frequency metrology [3], terahertz generation [4], two photon and CARS spectroscopy and microscopy [5], and optical coherence tomography [6]. Other medical related applications are eye laser surgery and dentist drills [7]. In the industry, ultrafast lasers are used for micro-machining and marking [8, 9]. The corner stone of ultrafast optics is the mode-locked laser, and developments of mode-locked lasers have been a huge research field in itself.

1.1 Mode-locked lasers

Mode-locking of a laser refers to a locking of the phase relations between many neighboring longitudinal modes of the laser cavity. Locking of such phase relations enables a periodic variation in the laser output which is stable over time, and with a periodicity given by the round trip time of the cavity. If sufficiently many longitudinal modes are locked together with only small phase differences between the individual modes, it results in a short pulse which may have a significantly larger peak power than the average power of the laser. The origin of mode-locking is best understood in the time domain. A laser in steady state is a feedback system, where the gain per round trip is balanced by the losses. If a nonlinear (i.e. nonlinear in terms of optical power) element is introduced into

the cavity, which introduces a higher loss at lower powers, the laser may favour a superposition of longitudinal modes corresponding to a short pulse with high peak power. However, a further requirement for obtaining stable mode-locking is that the pulse reproduces itself after one round trip (within a total phaseshift on all the longitudinal modes). The phase relations between different modes are affected by effects such as dispersion, gain bandwidth, nonlinear phase shifts etc. Although an infinite number of different pulses can be constructed as different superpositions of longitudinal modes, usually only a single pulse specified by its shape, duration, peak power and chirp is a stable solution of the cavity, and thus the output pulse characteristics can be designed and controlled by changing the physical parameters of the comprising laser elements.

Various mechanisms (both active and passive) exist for mode-locking lasers. For a review of active and passive mode-locking and its historical development, see e.g. reference [10]. For a review of mode-locked fiber lasers see e.g. references [11, 12], and for a more current review of fiber laser systems in general, see e.g. references [13, 14].

1.2 Fiber lasers

Traditionally, classical solid-state mode-locked lasers (i.e. lasers based on laser crystals like e.g. the Ti:Sapphire and the Nd:YAG lasers) have dominated the market, and in terms of reliability and long term stability these solid-state lasers are still the preferred choice. However, solid-state lasers also require stable laboratory-like environments with optical tables and stabilized room temperature. Furthermore, solid-state lasers have a high power consumption, and often require maintenance. If ultrafast optics are to gain grounds on much wider commercial markets, solutions to these limitations must be found.

The potential of making compact, rugged laser systems with low power consumption at relative low price make amplified fiber lasers a very promising alternative to classical solid state lasers. The key properties that make rare-earth doped fibers attractive as laser gain media are the high single pass gain combined with broad gain bandwidths and excellent beam quality. These qualities make fibers attractive as gain media in mode-locked lasers. The commercial market has been pioneered by especially one company, IMRA [15], but as the market has grown, more companies have joined the game and developed commercial fiber laser products. The development of fiber lasers has initially been driven by the massive development of telecommunication components, and for many years fiber lasers based on erbium technology have dominated the fiber laser market. Very recently companies like e.g. IMRA and Fianium [16] have also included fiber lasers based on ytterbium (yb) doped fibers in their assortment. A major reason for this recent development of fiber lasers is that fiber lasers can now be directly pumped by laser diodes. Combined with the huge progress and technological development of high power diode lasers, this gives a competitive edge compared to classical solid state lasers. Furthermore, the

development of double clad large mode area fibers for effective fiber amplifiers makes it possible to up-convert the spectral brightness of the multi-mode diode lasers, and thus realize high average power laser outputs with excellent beam quality. A large contribution to this development of large mode area fibers comes from the development of photonic crystal fibers.

1.3 Photonic Crystal Fibers

Photonic crystal fibers (PCFs) are fibers with a microstructured cross section. Usually PCFs are based on a periodic arrangement of fused silica and air holes running parallel to the propagation-axis of the fiber, but the term PCF also covers fibers comprising other combinations of materials with different refractive indexes. A diagram of the cross section of a typical PCF is shown in figure 1.1 (left). PCFs were first proposed and demonstrated by Russell in 1996 [17]. The periodic modulation of the refractive index in a PCF can result in photonic band gaps. This is similar to the creation of bandgaps in semiconductors because of the periodic arrangement of atoms in a lattice. In semiconductors, electrons of certain energies are prohibited because of these bandgaps. In a PCF, it is photons of certain wavelengths that are prohibited. A core in which light can be guided can be created by introducing a defect into the periodic structure. Light of certain wavelengths is then confined to this core if the surrounding structure exhibits a bandgap at these wavelengths [18]. This class of fibers are known as photonic bandgap (PBG) fibers.

Although PBGs have interesting features, of which some are explored in this thesis, it is perhaps PCFs with a solid core which have had the largest impact in the field of ultrafast optics so far. Solid core PCFs guide light similarly to standard step index fibers, but the increased flexibility in design gives PCFs some interesting properties over standard fibers. For example, if the scale of the microstructure is comparable to the wavelength of the guided light, the diffrac-

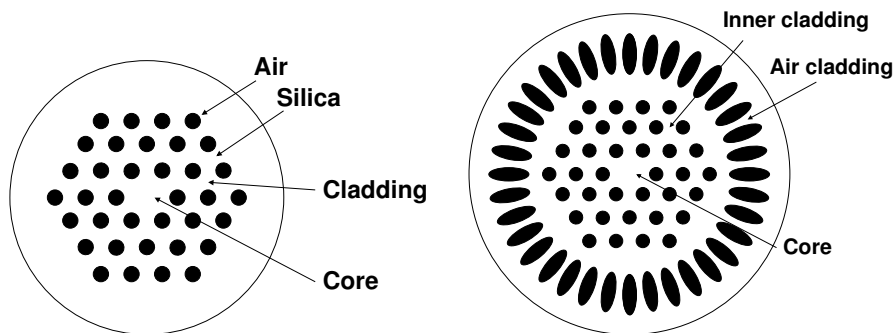


Figure 1.1: Left: Diagram of the cross section of a typical solid core standard PCF. Right: Diagram of a double clad PCF.

tion of the light penetrating into the cladding will play a dominant role on the guiding properties of the fiber. In practice this results in a strong influence on the dispersive properties of the fiber, and hence the dispersion of the fiber can be tailored by designing the cladding properly. This property is used in small core PCFs for supercontinuum generation. In chapter 8 and 9 different mode-locked laser sources are investigated for supercontinuum generation in small core PCFs. PBG fibers also exhibit very strong waveguide contributions to the dispersion, and in chapter 5 the use of a PBG fiber inside a mode-locked laser is investigated. PBG fibers with a hollow core exhibit very low nonlinearities, and in chapter 5 a hollow core PBG fiber is also used for external pulse compression after external amplification of the mode-locked laser.

It is possible to design single mode PCFs with much larger cores than step index fibers due to the large index difference between air and silica, and the design freedom make the creation of e.g. double clad and/or polarization maintaining (PM) fibers possible. A diagram of the cross section of a double clad PCF is shown in figure 1.1 (right). In chapter 7 amplification of a mode-locked laser to the micro-Joule level in a large core double clad PM PCF is demonstrated.

1.4 Challenges of mode-locked fiber laser systems

Although fiber lasers have many qualities making them superior to e.g. classical solid-state lasers, there are also many challenges which have to be overcome. To utilize the full potential of fibers, several things have to be fulfilled. Besides being able to produce comparable pulse energies, pulse durations and average powers, the fiber laser system should also prove equally stable and reliable. Primarily the fiber laser should be environmentally stable. Environmentally stable means that the output from the laser is not susceptible to changing environmental conditions such as changing temperatures, air convection etc. In chapter 6, 8 and 9 different approaches of making environmentally stable mode-locked lasers are presented. Furthermore, the fiber laser should preferably be implemented with no sections of free space optics to make it as stable, compact and cheap as possible. In chapter 9 a supercontinuum source is demonstrated which has no sections of free space optics and is based on an environmentally stable mode-locked laser.

Other important limitations in fiber lasers and amplifiers are the nonlinearities affecting the pulse due to the tight confinement and long interaction lengths in optical fibers. In chapter 7 amplification beyond the nonlinear limit without strong pulse distortions is demonstrated.

Outline of the thesis

In **Chapter 2**, the nonlinear Schrödinger equation is derived, and gives the theoretical background for pulse propagation in optical fibers.

In **Chapter 3**, a numerical model for fiber laser simulations is developed.

In **Chapter 4**, relevant characterization techniques for mode-locked lasers are introduced.

Chapter 5 presents a mode-locked fiber laser using solid core photonic bandgap fiber for intra cavity dispersion compensation.

Chapter 6 presents an environmentally stable mode-locked fiber laser generating parabolic pulses.

Chapter 7 introduces the theory of parabolic pulse amplification and presents the direct amplification of parabolic pulses to power levels exceeding the nonlinear limit.

Chapter 8 presents a dispersion compensation free oscillator and setup for supercontinuum generation to high average powers.

Chapter 9 presents an environmentally stable low repetition rate mode-locked fiber laser based on nonlinear polarization rotation.

Chapter 10 Summary and outlook.

CHAPTER 2

The Nonlinear Schrödinger Equation

In this chapter, the nonlinear Schrödinger equation (NLSE) will be derived. This equation is fundamental for the understanding of pulse propagation in optical fibers. It forms the theoretical basis for chapter 3, where the numerical model used for fiber laser simulations is introduced. Simplified analytical limits are also given at the end of this chapter to introduce different concepts of pulse propagation.

2.1 Introduction

An intriguing property of light is that it can be modeled well, and its interaction with the surroundings calculated with great accuracy. One of the most accurate models in physics describing the world around us, is Maxwell's well known equations for electromagnetic radiation. With this tool at hand, many systems involving light can in principle be modeled exactly. However, the complexity of the system is often a limiting factor and approximations have to be introduced to obtain either simpler analytical equations or numerical calculated results that converge in finite time. The successful development and massive progress in the field of laser and fiber optics is in part due to the accuracy of even simple models, and the ability to predict results for complex systems, such as e.g. mode-locked lasers.

Nonlinear pulse propagation in optical fibers can be accurately modeled by one or more coupled partial differential equations which, for historical reasons, are called the nonlinear Schrödinger equations (NLSE) (Not related to the quantum mechanical Schrödinger equation). The NLSE have been applied in fiber optics since the beginning of the eighties, where it was used to describe Mollenauer's first experimental observations of solitons in optical fibers [19]. The NLSE have also been applied in numerous other fields [1, 20–22]. Today it is used extensively to model pulse propagation in optical fibers [1, 23–32]. As will be evident throughout this thesis, the development of new mode-locked fiber lasers requires numerical models, and most experimental results obtained here, have been accompanied by numerical calculations both prior, during and subsequent to the experiments. Furthermore, both the analytical and numerical theory have been crucial to the initial understanding of the complicated mechanisms acting inside fiber lasers.

2.2 The nonlinear Schrödinger equation

The NLSE comes in a variety of different forms, depending on which approximations are appropriate. The starting point of this derivation is the wave equation, as obtained from Maxwell's equations with no source terms and under the assumption ($\nabla \cdot \mathbf{E} = 0$) [1]:

$$\nabla^2 \mathbf{E}(\mathbf{r}, t) = \frac{1}{c^2} \frac{\partial^2}{\partial t^2} \mathbf{E}(\mathbf{r}, t) + \mu_0 \frac{\partial^2}{\partial t^2} \mathbf{P}(\mathbf{r}, t). \quad (2.1)$$

$\mathbf{E}(\mathbf{r}, t)$ is the electric field and $\mathbf{P}(\mathbf{r}, t)$ the induced polarization. In linear media, the induced polarization is assumed to be proportional to the electric field, but in optical fibers, where the peak intensity of especially short pulses can be very high, this assumption is no longer valid, and higher order terms have to be included. The induced polarization can, however, be written as a sum of linear and nonlinear contributions:

$$\mathbf{P} = \mathbf{P}_L + \mathbf{P}_{NL} = \varepsilon_0 \chi^{(1)} : \mathbf{E} + \varepsilon_0 \chi^{(2)} : \mathbf{E}\mathbf{E} + \varepsilon_0 \chi^{(3)} : \mathbf{E}\mathbf{E}\mathbf{E} + \dots, \quad (2.2)$$

where $\chi^{(1)}$ is the linear, and $\chi^{(n)}$, $n > 1$ the nonlinear susceptibilities, and $\chi^{(3)}$: EEE denotes a tensor product, where all possible combinations of products between different polarizations are implicit as well as the integration over all times. The real part of $\chi^{(1)}$ relates to linear phase changes (and to the real part of the refractive index of the material), and the imaginary part to linear losses and gains. The real part of $\chi^{(2)}$ is responsible for second harmonic generation, but due to inversion symmetry in the amorphous SiO₂ [33] all even terms disappears, and hence $\chi^{(3)}$ is the only significant nonlinear term. $\chi^{(3)}$ relates to a variety of different nonlinear phenomena. In optical fibers $\chi^{(3)}$ originates from the interaction of the light with the electrons of the medium (Kerr nonlinearity) and with the optical phonons (Raman scattering).

The equations are significantly simplified if initially the electric field is assumed to be only linearly polarized and the fast oscillating parts is separated out:

$$\mathbf{E}(\mathbf{r}, t) = \frac{1}{2} \hat{x} [E(\mathbf{r}, t) \exp(-i\omega_0 t) + c.c.]. \quad (2.3)$$

ω_0 is the carrier or central frequency. The equation can now be Fourier transformed to frequency space, using the following convention for the Fourier transforms:

$$E(\mathbf{r}, \omega) = \int_{-\infty}^{\infty} \exp(i(\omega - \omega_0)t) E(\mathbf{r}, t) dt = \text{FT}\{E(\mathbf{r}, t)\} \quad (2.4)$$

$$E(\mathbf{r}, t) = \frac{1}{2\pi} \int_{-\infty}^{\infty} \exp(-i(\omega - \omega_0)t) E(\mathbf{r}, \omega) d\omega = \text{FT}^{-1}\{E(\mathbf{r}, \omega)\}. \quad (2.5)$$

The presence of ω_0 inside of the Fourier transform is simply a consequence of $E(\mathbf{r}, t)$ being slowly varying with respect to t . In frequency space the temporal convolution integral with $\chi^{(1)}(t - t_1)$ is replaced by a simple multiplication. Time derivatives are replaced by: $\frac{\partial}{\partial t} \rightarrow -i\omega$, $\frac{\partial^2}{\partial t^2} \rightarrow -\omega^2$, when working on $E(\mathbf{r}, t) \exp(-i\omega_0 t)$. On the right hand side, $\frac{\partial^2}{\partial t^2} P_{NL} \exp(-i\omega_0 t)$ is approximated with $\exp(-i\omega_0 t)(-\omega_0^2 - i\omega_0 \frac{\partial}{\partial t}) P_{NL}$ and hence equation 2.1 can be translated into a modified Helmholtz equation:

$$\nabla^2 E(\mathbf{r}, \omega) + \varepsilon(\omega) \frac{\omega^2}{c^2} E(\mathbf{r}, \omega) = -\mu_0 \omega_0^2 \text{FT}\{(1 + \frac{i}{\omega_0} \frac{\partial}{\partial t}) P_{NL}(\mathbf{r}, t)\}, \quad (2.6)$$

where $\varepsilon(\omega) = 1 + \chi^{(1)}(\omega)$, and where $\chi^{(1)}(\omega)$ is the Fourier transform of $\chi^{(1)}(t - t_1)$. $P_{NL}(\mathbf{r}, t)$ is the slowly varying induced polarization defined similarly to equation 2.3. By assuming weak coupling between the transverse and longitudinal degrees of freedom through the nonlinearity, the slowly varying part of the electric field, $E(\mathbf{r}, \omega)$, can, to a good approximation, be separated into a product of a function with longitudinal dependence, $A(z, \omega) \exp(i\beta_0 z)$, and a function with transversal dependence, $F(x, y, \omega)$:

$$E(\mathbf{r}, \omega) = F(x, y, \omega) \cdot A(z, \omega) \cdot \exp(i\beta_0 z), \quad (2.7)$$

where $A(z, \omega)$ can further be assumed to be a slowly varying function of z under the Slowly Varying Envelope approximation (SVEA). $F(x, y, \omega)$ is assumed to be normalized: $\int_{-\infty}^{\infty} dx dy F(x, y, \omega) = 1$. An important assumption for the derivation of the NLSE is that $F(x, y, \omega)$ is independent of ω so that it can be moved outside the Fourier transform:

$$E(\mathbf{r}, t) = \text{FT}^{-1}\{F(x, y, \omega) \cdot A(z, \omega) \cdot \exp(i\beta_0 z)\} \quad (2.8)$$

$$= F(x, y) \cdot \exp(i\beta_0 z) \cdot A(z, t), \quad (2.9)$$

where $A(z, t) = \text{FT}^{-1}\{A(z, \omega)\}$. This assumption corresponds to the assumption of a wavelength independent mode-field diameter (MFD). However, the MFD may vary considerably on a wavelength scale of ~ 100 nm. Hence this assumption is reasonable only for pulse widths smaller than this. β_0 is the wave number, chosen so that: $\beta_0 \equiv \beta(\omega_0)$, where $\beta(\omega)$ is found below. The Helmholtz equation, equation 2.6, can then be separated into equations of independent transverse and longitudinal parts:

$$\left(\frac{\partial^2}{\partial x^2} + \frac{\partial^2}{\partial y^2}\right)F(x, y) + \varepsilon(\omega)\frac{\omega^2}{c^2}F(x, y) = \beta^2 F(x, y) \quad (2.10)$$

$$F(x, y)\left(2i\beta_0\frac{\partial}{\partial z} + 2\beta_0(\beta - \beta_0)\right)A(z, \omega) = \mu_0\omega_0^2\text{FT}\left\{\left(1 + \frac{i}{\omega_0}\frac{\partial}{\partial t}\right)P_{NL}(\mathbf{r}, t)\right\}, \quad (2.11)$$

where the SVEA approximation was used to neglect a second derivative term: $\frac{\partial^2}{\partial z^2}A(z, \omega)$, and $(\beta^2 - \beta_0^2)$ was approximated with $2\beta_0(\beta - \beta_0)$ in equation 2.11. Both these approximations are justified as long as $\omega - \omega_0 \ll \omega$ [1]. In equation 2.10 $\beta = \beta(\omega)$ is the eigenvalue and $F(x, y)$ the eigenfunctions of the transverse field distribution, which have to be found for a given fiber geometry and fiber characteristics. $F(x, y)$ is usually referred to as modes. For step-index fibers $F(x, y)$ is a superposition of Bessel and Neuman functions. However, for most single mode fibers a Gaussian approximation of $F(x, y)$ is adequate. A fiber is called multi mode if more than one solution to equation 2.10 exists, but as only single mode fibers are treated in this thesis, the NLSE will only be derived for this case. Higher order transverse modes are usually unwanted in fiber optics and especially when short pulses are involved. They can lower the brightness, and lead to pulse break up due to different propagation velocities of the different modes. The waveguide contribution to the propagation constant, $\beta(\omega)$, also enters through equation 2.10.

In most dielectric materials, and also in optical fibers, the real part of $\varepsilon(\omega)$ dominates and even in high loss and high gain fibers, the imaginary part is only a small perturbation. Hence, the (real) refractive index, n , can be introduced as:

$$\varepsilon(\omega) = (n(\omega) + \Delta n(\omega))^2 \approx n(\omega)^2 + 2n(\omega)\Delta n(\omega), \quad (2.12)$$

where the imaginary part is included as a small perturbation in $\Delta n(\omega)$:

$$\Delta n(\omega) = \frac{i(\alpha(\omega) - g(\omega))c}{2\omega}. \quad (2.13)$$

$\alpha(\omega)$ represents the linear power loss and $g(\omega)$ the linear power gain (in units of m^{-1}). In first-order perturbation theory $\Delta n(\omega)$ does not affect the transverse field distribution, $F(x, y)$, but only the eigenvalues. Hence $\beta(\omega)$ in equation 2.11 is replaced with $\beta(\omega) + \Delta\beta(\omega)$, where:

$$\begin{aligned} \Delta\beta(\omega) &= \frac{\omega}{c} \int \int \Delta n(\omega) |F(x, y)|^2 dx dy \\ &= i \frac{\alpha(\omega)}{2} - i \frac{g(\omega)}{2}. \end{aligned} \quad (2.14)$$

The induced nonlinear polarization can be approximated by:

$$P_{NL}(\mathbf{r}, t) = -\varepsilon_0 2n_2 n(\omega_0) E(\mathbf{r}, t) \int_{-\infty}^{\infty} R(t - t_1) |E(\mathbf{r}, t_1)|^2 dt_1 \quad (2.15)$$

where only terms oscillating with ω_0 have been maintained. Terms oscillating with $3\omega_0$ have been neglected, as these correspond to third harmonic generation and require phase matching which is usually not present in the fiber. Equivalently one could say, that these terms oscillate so fast compared to the slowly varying terms, that their contributions average out. The nonlinear refractive index, n_2 , has been introduced. n_2 is proportional to the real part of $\chi^{(3)}$, and if $A(z, \omega)$ is chosen to be normalized to units of $\text{W}^{1/2}$, n_2 is in the order of $2 - 3 \cdot 10^{-20} \text{ m}^2/\text{W}$ in standard silica fibers, depending on the doping [1]. The imaginary part of $\chi^{(3)}$ relates to two photon absorption and emission, and is also negligible. $R(t - t_1)$ is the nonlinear response function normalized in a manner similar to the delta function, i.e., $\int_{-\infty}^{\infty} R(t - t_1) dt_1 = 1$. If only the interactions with the electrons are included, $R(t - t_1)$ can be approximated by a delta function, $\delta(t - t_1)$, as the electronic response of the material is almost instantaneous. This approximation is valid in the limit where the pulse spectrum corresponds to a transform limited pulse with a duration above $\sim 1 \text{ ps}$ [1]. In short mode-locked fiber lasers, this is also a reasonable assumption as stimulated Raman scattering is usually not present in the output, but as shown in chapter 9 this is not always the case. Also, if soliton dynamics are involved inside the laser, the Raman contribution to $\chi^{(3)}$ is highly relevant, as especially a soliton can experience a significant red shift over a short length of fiber due to this effect [1, 34]. With these assumptions, the NLSE in frequency domain can now be derived:

2.2.1 The nonlinear Schrödinger equation in frequency domain

Using again the approximation of equation 2.9, the transverse dependence of equation 2.11 can be integrated out by multiplying with $F^*(x, y)$, and integrat-

ing over x and y :

$$\begin{aligned} \frac{\partial}{\partial z} A(z, \omega) = & i(\beta - \beta_0)A(z, \omega) - \frac{\alpha(\omega)}{2}A(z, \omega) + \frac{g(\omega)}{2}A(z, \omega) \\ & + i\gamma \text{FT}\left\{\left(1 + \frac{i}{\omega_0} \frac{\partial}{\partial t}\right)A(z, t) \int_{-\infty}^{\infty} R(t - t_1)|A(z, t_1)|^2 dt_1\right\}, \end{aligned} \quad (2.16)$$

where the nonlinear coefficient, $\gamma = \frac{\omega_0 n_2}{c A_{\text{eff}}}$, has been introduced, and where:

$$A_{\text{eff}} = \frac{1}{\int \int dx dy |F(x, y)|^4} \quad (2.17)$$

is the effective area of the fiber. Equation 2.16 is the NLSE in frequency space including the self-steepening and shock formation term, $\frac{i}{\omega_0} \frac{\partial}{\partial t}$, and the full Raman integral. If the self-steepening term is neglected, and $R(t - t_1)$ approximated by a delta function, the NLSE in frequency domain reduces to:

$$\begin{aligned} \frac{\partial}{\partial z} A(z, \omega) = & i\beta(\omega)'A(z, \omega) - \frac{\alpha(\omega)}{2}A(z, \omega) + \frac{g(\omega)}{2}A(z, \omega) \\ & + i\gamma \text{FT}\{|A(z, t)|^2 A(z, t)\}. \end{aligned} \quad (2.18)$$

where $A(z, t) = \text{FT}^{-1}\{A(z, \omega)\}$, and where the propagation has been expanded in a Taylor series:

$$\begin{aligned} \beta(\omega)' &= \frac{n(\omega)\omega}{c} - \beta_0(\omega_0) - \beta_1(\omega_0)(\omega - \omega_0) \\ &= \sum_{m>1} \frac{1}{m!} \beta_m(\omega - \omega_0)^m; \quad \beta_m = \frac{\partial^m \beta}{\partial \omega^m} \Big|_{\omega=\omega_0} \\ &= \frac{1}{2} \beta_2(\omega_0)(\omega - \omega_0)^2 + \frac{1}{6} \beta_3(\omega_0)(\omega - \omega_0)^3 + \dots \end{aligned} \quad (2.19)$$

The β_1 term has furthermore been subtracted in order to retain a frame of reference moving with the pulse (with the velocity $1/\beta_1$). $\beta(\omega)'$ includes effects of group velocity dispersion, β_2 , and higher order dispersion, $\beta_{m>2}$. The coefficients, $\beta(\omega)'$, $\alpha(\omega)$ and $g(\omega)$ can all be measured and γ calculated (see below (subsection 2.2.3)). Equation 2.18 is hence in a form, which can be integrated numerically using experimental parameters. A method to measure $\beta(\omega)'$ is presented in chapter 4. Equation 2.18 was derived under the primary assumptions, that only a single polarization state is present, and that Raman nonlinearities could be neglected. It has been used for the calculations of oscillators and amplifiers in chapters 5-7.

2.2.2 The nonlinear Schrödinger equation in time domain:

The NLSE is usually presented in the time domain, and in the time domain $(\omega - \omega_0)$ is replaced with $i \frac{\partial}{\partial t}$, and $(\omega - \omega_0)^2$ with $-\frac{\partial^2}{\partial t^2}$. The time domain version

of the NLSE can now be found by simply Fourier transforming equation 2.18:

$$\begin{aligned} \frac{\partial}{\partial z} A(z, t) = & -i \frac{\beta_2}{2} \frac{\partial^2}{\partial t^2} A(z, t) - \frac{\alpha_0}{2} A(z, t) + \frac{g_0}{2} A(z, t) \\ & + i\gamma |A(z, t)|^2 A(z, t), \end{aligned} \quad (2.20)$$

where a constant linear loss and gain is assumed, and only the group velocity dispersion term included.

2.2.3 Nonlinearities

The nonlinear coefficient, $\gamma = \frac{\omega_0 n_2}{c A_{\text{eff}}}$ in equations 2.18 and 2.20, can be calculated, when the radial field distribution is known. For most step-index fibers a Gaussian radial dependence with a mode-field diameter (MFD), w , is set equal to the core diameter of the fiber, is a very good approximation for the field distribution [1]. The effective area of the fiber then reduces to: $A_{\text{eff}} = \pi(w/2)^2$, and from this γ can be calculated.

If the full Raman integral has to be included, the response function, $R(t - t_1)$ should include both the electronic and vibrational (Raman) contributions: $R(t - t_1) = (1 - f_R)\delta(t - t_1) + f_R h_R(t - t_1)$, where $f_R \approx 0.18$ is the fractional contribution of the delayed Raman response [1]. $h_R(t - t_1)$ can be approximated by the analytical function:

$$h_R(t - t_1) = \frac{\tau_1^2 + \tau_2^2}{\tau_1 \tau_2^2} \exp(-(t - t_1)/\tau_2) \sin((t - t_1)/\tau_1); \quad t_1 \leq t, \quad (2.21)$$

and $h_R(t - t_1) = 0$ for $t_1 > t$. Appropriate constants are $\tau_1 = 12.2$ fs and $\tau_2 = 32$ fs [1]. With this approximation for the Raman integral, the NLSE in equation 2.16 is now also suitable for numerical calculations.

2.2.4 Two polarization states

If more than one polarization state is present in the fiber (or equivalently if the laser light is not linearly polarized), the assumption (equation 2.3) leading to equations 2.16 and 2.18 has to be relaxed. Equation 2.3 is replaced with:

$$\mathbf{E}(\mathbf{r}, t) = \frac{1}{2} [(\hat{x}E_x + \hat{y}E_y) \exp(-i\omega_0 t) + c.c.], \quad (2.22)$$

and equivalently for the nonlinear induced polarization. Collecting terms of same polarization state, and retaining only terms with $\exp(-i\omega_0)$ dependence, the x and y component of the nonlinear induced polarization are given by:

$$P_{NL,x}(\mathbf{r}, t) = -\varepsilon_0 2n_2 n(\omega_0) [(|E_x|^2 + \frac{2}{3}|E_y|^2)E_x + \frac{1}{3}(E_x^* E_y)E_y] \quad (2.23)$$

$$P_{NL,y}(\mathbf{r}, t) = -\varepsilon_0 2n_2 n(\omega_0) [(|E_y|^2 + \frac{2}{3}|E_x|^2)E_y + \frac{1}{3}(E_y^* E_x)E_x]. \quad (2.24)$$

Here the response function, $R(t - t_1)$, has also been approximated with a delta function. Two coupled equations for the slowly varying parts of E_x and E_y can now be derived in a similar manner as above:

$$\begin{aligned} \frac{\partial}{\partial z} A_x(\omega) = & i\beta(\omega)' A_x(\omega) + i\frac{\Delta\beta_1}{2}(\omega - \omega_0)A_x(\omega) - \frac{\alpha(\omega)}{2}A_x(\omega) + \frac{g(\omega)}{2}A_x(\omega) \\ & + i\gamma\text{FT}\{|A_x(t)|^2 + \frac{2}{3}|A_y(t)|^2\}A_x(t) + \frac{i}{3}A_x(t)^*A_y(t)^2\exp(-2i\Delta\beta_0 z)\} \end{aligned} \quad (2.25)$$

$$\begin{aligned} \frac{\partial}{\partial z} A_y(\omega) = & i\beta(\omega)' A_y(\omega) - i\frac{\Delta\beta_1}{2}(\omega - \omega_0)A_y(\omega) - \frac{\alpha(\omega)}{2}A_y(\omega) + \frac{g(\omega)}{2}A_y(\omega) \\ & + i\gamma\text{FT}\{|A_y(t)|^2 + \frac{2}{3}|A_x(t)|^2\}A_y(t) + \frac{i}{3}A_y(t)^*A_x(t)^2\exp(2i\Delta\beta_0 z)\}, \end{aligned} \quad (2.26)$$

where $\Delta\beta_0 = \beta_{0,x} - \beta_{0,y} = \frac{\omega}{c}\Delta n$. and where $\Delta\beta_1 = \beta_{1,x} - \beta_{1,y} = \frac{\Delta n_g}{c}$. Δn is the (phase) birefringence of the fiber, and Δn_g is the group birefringence. In chapter 4 a method to measure the group birefringence is introduced. A frame of reference moving at the average velocity $2/(\beta_{1,x} + \beta_{1,y})$ have been chosen (information contained in the terms $\pm i\frac{\Delta\beta_1}{2}$), and hence the x polarized field moves with a relative velocity of $2/\Delta\beta_1$ compared to the frame of reference, and the y polarized field moves with a relative velocity of $-2/\Delta\beta_1$. The coefficients, $\beta(\omega)'$, $\alpha(\omega)$ and $g(\omega)$ can usually be assumed to be polarization independent. The interaction between the two different polarization states (and hence the difference to two separate NLSE for a single polarization state) is in the nonlinear term.

Two limits are interesting in this thesis: Highly birefringent fibers and non-birefringent fibers. For the later case, $\Delta\beta_0 = 0$ and $\Delta\beta_1 = 0$. To eliminate the $A_x^*A_y^2$ and $A_y^*A_x^2$ terms in equations 2.25 and 2.26, the polarization representation can be changed from linear to circular, by introducing:

$$A_+ = (A_x + iA_y)/\sqrt{2}, \quad A_- = (A_x - iA_y)/\sqrt{2}. \quad (2.27)$$

Equations 2.25 and 2.26 then reduce to:

$$\begin{aligned} \frac{\partial}{\partial z} A_+(\omega) = & i\beta(\omega)' A_+(\omega) - \frac{\alpha(\omega)}{2}A_+(\omega) + \frac{g(\omega)}{2}A_+(\omega) \\ & + i\frac{2\gamma}{3}\text{FT}\{|A_+(t)|^2 + 2|A_-(t)|^2\}A_+(t) \end{aligned} \quad (2.28)$$

$$\begin{aligned} \frac{\partial}{\partial z} A_-(\omega) = & i\beta(\omega)' A_-(\omega) - \frac{\alpha(\omega)}{2}A_-(\omega) + \frac{g(\omega)}{2}A_-(\omega) \\ & + i\frac{2\gamma}{3}\text{FT}\{|A_-(t)|^2 + 2|A_+(t)|^2\}A_-(t). \end{aligned} \quad (2.29)$$

In the high birefringence case, the $\exp(-2i\Delta\beta_0 z)$ and $\exp(2i\Delta\beta_0 z)$ terms oscillate so rapidly, that they can be neglected. It is hence most favourable to remain the linear polarization representation. Although the equations are solved in the frequency domain, for clarity, the time domain version of equations 2.25-2.29 are:

High birefringence approximation:

$$\begin{aligned} \frac{\partial A_x}{\partial z} &= -\frac{\Delta\beta_1}{2} \frac{\partial A_x}{\partial t} - i\frac{\beta_2}{2} \frac{\partial^2 A_x}{\partial t^2} + \frac{\beta_3}{3} \frac{\partial^3 A_x}{\partial t^3} \\ &+ i\gamma(|A_x|^2 + \frac{2}{3}|A_y|^2)A_x + (\frac{g_0}{2} - \frac{\alpha_0}{2})A_x \end{aligned} \quad (2.30)$$

$$\begin{aligned} \frac{\partial A_y}{\partial z} &= +\frac{\Delta\beta_1}{2} \frac{\partial A_y}{\partial t} - i\frac{\beta_2}{2} \frac{\partial^2 A_y}{\partial t^2} + \frac{\beta_3}{3} \frac{\partial^3 A_y}{\partial t^3} \\ &+ i\gamma(|A_y|^2 + \frac{2}{3}|A_x|^2)A_y + (\frac{g_0}{2} - \frac{\alpha_0}{2})A_y, \end{aligned} \quad (2.31)$$

Non-birefringence approximation:

$$\begin{aligned} \frac{\partial A_+}{\partial z} &= -i\frac{\beta_2}{2} \frac{\partial^2 A_+}{\partial t^2} + \frac{\beta_3}{3} \frac{\partial^3 A_+}{\partial t^3} + i\frac{\Delta\beta}{2} A_- \\ &+ i\gamma\frac{2}{3}(|A_+|^2 + 2|A_-|^2)A_+ + (\frac{g_0}{2} - \frac{\alpha_0}{2})A_+ \end{aligned} \quad (2.32)$$

$$\begin{aligned} \frac{\partial A_-}{\partial z} &= -i\frac{\beta_2}{2} \frac{\partial^2 A_-}{\partial t^2} + \frac{\beta_3}{3} \frac{\partial^3 A_-}{\partial t^3} + i\frac{\Delta\beta}{2} A_+ \\ &+ i\gamma\frac{2}{3}(|A_-|^2 + 2|A_+|^2)A_- + (\frac{g_0}{2} - \frac{\alpha_0}{2})A_-, \end{aligned} \quad (2.33)$$

A NLSE for two polarization directions is used in the model of the laser presented in chapter 9, and the two limits are relevant for modeling nonlinear polarization rotation (see below (subsection 2.3.3)) in polarization maintaining (PM) fibers (High-birefringence approximation) and non-PM fibers (Non-birefringence approximation). In the derivation of the NLSE for the two polarization directions, Raman contributions were not included in the nonlinearities. A NLSE for two polarization directions and with the inclusion of the Raman terms can be found in references [35–40], and information about the coefficients in reference [41].

2.3 Analytical solutions

To understand the physics behind the NLSE, it is beneficial to look at some limiting cases, which can be calculated analytically.

2.3.1 Dispersion

To illustrate the effects of dispersion on a pulse, a simple analytical calculation can be done if all other terms but the group velocity dispersion are neglected:

$$\frac{\partial}{\partial z} A(z, \omega) = i\frac{\beta_2}{2}(\omega - \omega_0)^2 A(z, \omega),$$

For an initial Gaussian pulse with no chirp and FWHM temporal duration, t_0 , the field can be written as:

$$A(0, t) = A_0 \exp \left(-2 \ln(2) \left(\frac{t}{t_0} \right)^2 \right) \quad (2.34)$$

After propagation through a fiber of length, L , and with group velocity dispersion, β_2 , the output can analytically be calculated to be a chirped Gaussian pulse:

$$A(L, t) = A_0 \exp \left(-2 \ln(2) \frac{1 + iC}{1 + C^2} \left(\frac{t}{t_0} \right)^2 \right), \quad (2.35)$$

where the C is given by: $C = 2\beta_2 L \frac{2 \ln(2)}{t_0^2}$. The chirp of the pulse, $c(t) = -\frac{\partial \phi}{\partial t}$, where ϕ is the phase, is then given by $c(t) = 4 \ln(2) C t / t_0^2$, and is linear in t . The FWHM temporal pulse duration has now increased to: $\sqrt{1 + C^2} t_0$. Spectrally nothing has happened (to the power spectrum), as only a quadratic phase has been added:

$$A(L, \omega) = \exp(i \frac{\beta_2}{2} L (\omega - \omega_0)^2) A(0, \omega),$$

2.3.2 Self-phase modulation

If nonlinearities are also present, the pulse also obtains a intensity dependent and hence nonlinear phase. This is referred to as self-phase modulation (SPM). To illustrate the effects of SPM, all other terms are again neglected:

$$\frac{\partial}{\partial z} A(z, t) = i\gamma |A(z, t)|^2 A(z, t).$$

This equation can also be integrated analytically to give:

$$A(L, t) = \exp(i\gamma L |A(0, t)|^2) A(0, t).$$

If the initial pulse is again assumed to be an unchirped Gaussian pulse (equation 2.34), then the chirp of the pulse has a nonlinear temporal dependence, and whereas nothing has happened to the temporal shape of the pulse, the spectrum is now no longer Gaussian, but has spectrally broadened. Figure 2.1 shows the pure SPM spectral broadening of a 100 fs Gaussian pulse centered at 1030 nm. As shown in chapter 6 and 7, a special class of pulses (parabolic pulses), only acquires a linear chirp in the presence of nonlinearities, and interesting properties of parabolic pulses are investigated in these chapters.

2.3.3 Nonlinear polarization rotation

If a general elliptically polarized pulse is launched into a fiber where nonlinearities are present, it will experience a nonlinear polarization rotation (NPR). To

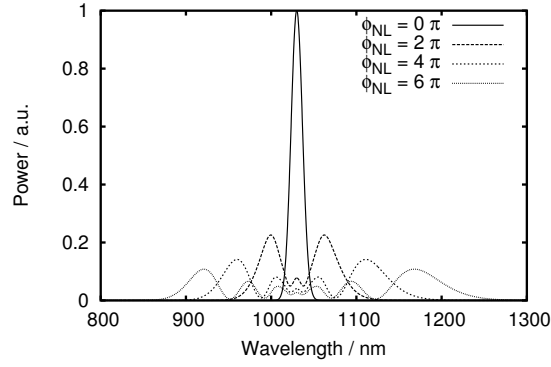


Figure 2.1: Pure SPM spectral broadening of a 100 fs Gaussian pulse centered at 1030 nm. The spectra are calculated at peak nonlinear phase shifts of 0, 2, 4 and 6π .

illustrate this, only the nonlinear terms of the NLSE for two polarization directions and in the non-birefringence approximation are maintained and all other terms neglected:

$$\begin{aligned}\frac{\partial A_+}{\partial z} &= i\gamma\frac{2}{3}(|A_+|^2 + 2|A_-|^2)A_+ \\ \frac{\partial A_-}{\partial z} &= i\gamma\frac{2}{3}(|A_-|^2 + 2|A_+|^2)A_-.\end{aligned}$$

These equations can also be integrated analytically to yield:

$$\begin{bmatrix} A_+(L) \\ A_-(L) \end{bmatrix} = \exp(i\frac{1}{2}(\Phi_+ + \Phi_-)) \begin{bmatrix} \cos(\frac{\Phi_+ - \Phi_-}{2}) & -\sin(\frac{\Phi_+ - \Phi_-}{2}) \\ \sin(\frac{\Phi_+ - \Phi_-}{2}) & \cos(\frac{\Phi_+ - \Phi_-}{2}) \end{bmatrix} \begin{bmatrix} A_+(0) \\ A_-(0) \end{bmatrix},$$

where:

$$\Phi_+ = \frac{2}{3}\gamma(|A_+(0)|^2 + 2|A_-(0)|^2) \quad (2.36)$$

$$\Phi_- = \frac{2}{3}\gamma(|A_-(0)|^2 + 2|A_+(0)|^2) \quad (2.37)$$

$$\Phi_+ - \Phi_- = \frac{2}{3}\gamma(|A_-(0)|^2 - |A_+(0)|^2), \quad (2.38)$$

and hence the polarization state rotates with an angle of $(\Phi_+ - \Phi_-)/2$. Notice that this angle is zero if the light is initially linearly polarized, as $|A_-(0)|^2 = |A_+(0)|^2$, and hence $\Phi_+ - \Phi_- = 0$. Also if the light is circular polarized, the polarization state is maintained.

2.3.4 Soliton

The soliton plays an important role in many areas of fiber optics, and as solitons are mentioned several times in this thesis, its analytical form is given here. The fundamental soliton is a solution of the simple NLSE:

$$\frac{\partial}{\partial z} A(z, t) = -i \frac{\beta_2}{2} \frac{\partial^2}{\partial t^2} A(z, t) + i \gamma |A(z, t)|^2 A(z, t),$$

which preserves both its temporal and spectral shape, as it propagates in the fiber. The fundamental soliton is found in the anomalous dispersion regime ($\beta_2 < 0$), and is characterized by a very characteristic sech shape:

$$|A(z, t)| = \left(\frac{|\beta_2|}{\gamma t_0^2} \right)^{1/2} \text{sech} \left(\frac{t}{t_0} \right),$$

and occurs when nonlinearities are exactly balanced by dispersion in the fiber.

2.3.5 Stimulated Raman Scattering

The Raman integral in the NLSE originates from inelastic scattering on the optical phonons in the fiber. On the creation of an optical phonon, the photon energy is reduced, and hence the wavelength of the photon increases. This effect effectively corresponds to a gain on the red side of the pulse, and the peak of this Raman gain is centered at about 13.2 THz from the central wavelength of the pulse. Starting from noise a new pulse will start to build up at this wavelength, and will eventually drain most of the energy from the original pulse. This is referred to as Stimulated Raman Scattering (SRS). The created pulse, called the 1th Stokes pulse will, when its peak power has increased sufficiently, start to create a new pulse, called the 2nd Stokes pulse, and so on. Chapter 9 presents a nice example of SRS. As the onset of SRS is a stochastic process, which depends on the peak power, fiber length, linear losses, etc., a threshold peak power can be calculated below which SRS can be neglected [1]:

$$P_{\text{peak}}^{\text{th}} = \frac{16 A_{\text{eff}}}{g_R L} \frac{\alpha L}{1 - e^{-\alpha L}}.$$

A_{eff} is the effective area of the fiber, g_R is the peak Raman-gain ($g_R \approx 10^{-13}$ m/W), α is the power loss per unit length and L is the length of the fiber.

In anomalous dispersive fibers where a soliton can be created, the mechanisms creating the soliton will try to maintain the solitonic shape of the pulse even in the presence of the Raman gain. The result is a soliton which gradually redshifts toward higher wavelengths instead of generating a 1th stokes pulse [1, 34]. As the soliton gradually loses energy, it compensates by changing its width, while maintaining its sech shape.

2.4 Numerical algorithm

To reduce computational workload it is worth noticing that $d\omega$ in the Fourier integral in equation 2.5 without loss of generality can be replaced by $d(\omega - \omega_0)$, and hence a new variable, $\omega_1 = \omega - \omega_0$ can be introduced. Equations 2.4 and 2.5 are now mathematically on the standard Fourier integral form, and standard fast Fourier algorithms can be used. All fields in the frequency space can now be centered at $\omega_1 = 0$, and restricted to the range where the pulse spectrum exists. Equivalently, the fields in the temporal space can be centered at $t = 0$, and extended only to a range containing the temporal pulse.

CHAPTER 3

Simulation of fiber lasers

A numerical model for fiber laser simulations is presented. The model is based on the nonlinear Schrödinger equation (NLSE) which was derived in chapter 2. The model further comprises effects of saturable gain, nonlinear losses and cavity losses in general, which are described in this chapter. The cavity is modeled as a sequence of different elements. In the simulations, a pulse is iterated from noise over many round trips until a steady solution is reached.

3.1 Introduction

The theory behind mode-locked lasers is well established. For classical solid state and dye lasers advanced analytical theories exists, and the master equation developed by Haus is perhaps one of the most successful models describing many types of mode-locked lasers [10, 42–46]. However, as the analytical theory is based on a linearization of the effect of all cavity elements on the pulse, the theory is only adequate if these effects are weak on each pass. In fiber lasers in general, and for the lasers in this thesis in particular, this is not the case, and hence more advance models based on numerical calculations have to be used. The models used in this thesis is based on solving the NLSE numerically. There are however additional effects which have to be included for adequate descriptions of a mode-locked fiber laser. First of all, a more advanced description of the gain medium is needed. Second, a model of the mode-locking mechanism has to be included, and finally cavity losses also has to be taken into account. These effects are described below, before an outline of a laser simulation is given. As an example simulations of an 80 MHz mode-locked fiber laser are presented.

3.2 Gain medium

The linear gain factor, $g(\omega)$, in the NLSE represents a small signal gain and, if $g(\omega)$ is constant as function of z , the power increases exponentially as $\exp(gz)$. However in real fibers, where a gain can be introduced by doping the fiber with appropriate optical active atoms, like e.g. rare earth atoms (Erbium, Ytterbium, Thulium, Neodymium, etc.), and by creating a population inversion by means of optical pumping, the gain experienced by a pulse depends on the intensity of the pulse. At increasing pulse intensities, the gain saturates. As the pulse duration as well as the round trip time is usually much shorter than the relaxation time of the excited states in the rare earth atoms, the population inversion in steady state operation only saturates as function of the average power of the pulse train. The lifetime of the excited state is ~ 10 ms in erbium and ~ 1 ms in ytterbium. If the fiber is pumped from one end, this further creates a nonuniform distribution of population inversion in the fiber due to the gradual absorption of the pump light. This nonuniform population inversion can be calculated using rate equations for the average power distribution in the fiber [47–52]. However, to simplify the numerical model and reduce computation time, this z dependence can to a good approximation be neglected if the doped fiber is really short. Hence the gain can be modeled by replacing:

$$g(\omega)/2 \rightarrow \frac{g(\omega)/2}{1 + \frac{P_{\text{ave}}(z)}{P_{\text{sat}}}}, \quad (3.1)$$

where P_{sat} is the saturation power and P_{ave} is the average power of the pulse train in the doped fiber. In linear cavities, the signal power enters the gain

medium from both sides, and hence the average power in the gain medium should be calculated as:

$$P_{\text{ave}}(z) = f_{\text{rep}} \int_{-T_R/2}^{T_R/2} |A(z, t)|^2 dt + P_{\text{ave}}^{\leftarrow}(z) \quad (3.2)$$

where f_{rep} is the repetition rate and $T_R = 1/f_{\text{rep}}$ the round trip time. $P_{\text{ave}}^{\leftarrow}(z)$ is the average power of the signal propagating in the opposite direction of the doped fiber. The inclusion of the average power from the signal propagating in the opposite direction is especially important if the gain fiber is located in a fiber laser where the loss on one side of the gain medium is much larger than on the other side. This is the case in many of the oscillators presented in this thesis. The result is a smaller amplification of the signal coming from the high loss side, due to saturation of the gain medium from the signal coming from the low loss side.

3.2.1 Ytterbium

All fiber lasers presented in this thesis are based on ytterbium doped fibers as the gain medium. Ytterbium has a very simple structure, and can be described as a 2 level system (see figure 3.1 (right)), where there is no excited state absorption of neither the pump nor the laser wavelengths [47, 51]. Figure 3.1 (left) shows the absorption and emission cross sections of ytterbium.

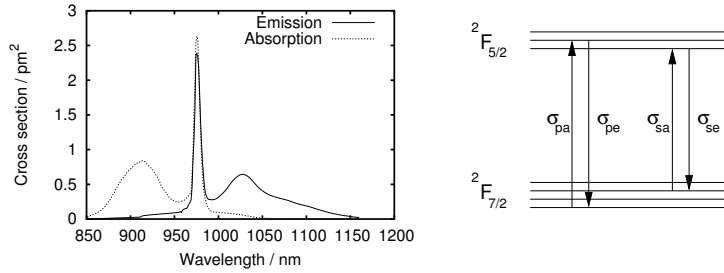


Figure 3.1: Left: The absorption and emission cross section for Yb^{3+} -doped silica [51]. Right: Energy band diagrams of ytterbium. (σ_{pa} , σ_{pe} , σ_{sa} , σ_{se} : pump and signal absorption and emission cross sections respectively.)

There are several reasons why ytterbium is an ideal candidate for mode-locked fiber lasers. Ytterbium has a high absorption at 976 nm, and for this wavelength there have been a large development of both single mode fiber pigtailed diode pump lasers and high power diode pump lasers (Single mode pump lasers at 976 nm have primarily been developed for use with Erbium in the telecommunication industry). Ytterbium further has a high quantum efficiency ($\sim 95\%$), as the lasing band is very close to the pump wavelength. Very

high doping concentrations are possible in ytterbium doped fibers, enabling very high single pass gains and high slope efficiencies (proportionality factor between output power and pump power) of up to $\sim 80\%$. This simplifies realizations of high efficiency fiber amplifiers [53], [VI], and hence necessary pulse energies and average powers for most applications are more easily reached with ytterbium based fiber laser systems. As seen in figure 3.1 (left), the emission band is also very broad and is hence cable of supporting very short pulses [54]. The gain of an ytterbium doped fiber can be well modeled by a Gaussian function with FWHM of ~ 40 nm and with a central wavelength at 1030 nm.

3.3 Mode-locking mechanisms

Beside the ability to model dispersion, gain, losses, nonlinearities, etc. in fibers, one important component is still missing to model mode-locked lasers. This is the nonlinear component used to make mode-locked lasing more favourable than cw lasing. For a laser to favour lasing in a mode with short pulses, an element or a combination of elements have to be present in the cavity, which introduces a higher loss at low power, so that a short pulse with higher peak power experiences a lower loss.

3.3.1 Nonlinear polarization rotation

One widely used possibility is to use nonlinear polarization rotation (NPR) in conjunction with a polarizer [10, 24, 42, 54–59]. By controlling the polarization state into a fiber with e.g. a set of wave-plates, the transmission through a polarizer on the other side of the fiber will be power dependent, and hence by proper adjustment of the wave-plates, an increasing transmission at increasing peak powers can be obtained. The laser presented in chapter 9 is based on this principle.

3.3.2 SESAM

Another possibility is to use a SESAM (Semiconductor Saturable Absorber Mirror). SESAMs are now both commercially available (see e.g. [60]) and fundamental in commercially available mode-locked fiber lasers (see e.g. [15, 16]). Although other mode-locking mechanisms have been investigated for fiber lasers [61–63], the most frequently researched mechanisms are NPR and SESAMs. The mode-locked lasers presented in chapters 5–8 are based on SESAM mode-locking.

A SESAM consists of a Bragg-mirror on a semiconductor wafer like GaAs, incorporating materials with an intensity dependent absorption. The saturable absorber layer consists of a semiconductor material with a direct band gap slightly lower than the photon energy [60]. Often GaAs/AlAs is used for the Bragg mirrors and InGaAs Quantum Wells for the saturable absorber material. During

the absorption electron-hole pairs are created in the film. As the number of photons increases, more electrons are excited, but as only a finite number of electron-hole pairs can be created, the absorption saturates. The electron-hole pairs recombined non-radiatively, and are after a certain period of time again ready to absorb photons.

Key parameters of the SESAM when designing mode-locked lasers are the recovery time of the SESAM, the modulation depth, the bandwidth, the saturation intensity and the non-saturable losses.

Generally the Bragg stack can be chosen to be either anti-resonant or resonant. SESAMs based on resonant Bragg stacks can have quite large modulation depths, but with the limited bandwidth of the resonant structure. Anti-resonant SESAMs can have quite large bandwidths (e.g. ~ 100 nm), but at the expense of a smaller modulation depth. A larger modulation depth can be obtained from an anti-resonant design at the expense of higher unsaturable losses. In solid state lasers where the single pass gain is low, the unsaturable losses of the SESAM must also remain low, but in fiber lasers where the single pass gain is much higher, unsaturable losses are less important.

The recovery time should ideally be as small as possible. Recovery times of same orders of magnitude as the pulse duration will cause asymmetric spectra if the pulse is chirped at the impact with the SESAM, and hence strongly affect the pulse dynamics inside the cavity. Even larger recovery times can limit the obtainable pulse duration from the laser. Because the relaxation time due to the spontaneous photon emission in a semiconductor is about 1 ns [60], some precautions have to be taken to shorten it drastically. Two technologies are used to introduce lattice defects in the absorber layer for fast non-radiative relaxation of the carriers: low-temperature molecular beam epitaxy (LT-MBE) and ion implantation. The relaxation time can be adjusted by adjusting the growth temperature in case of LT-MBE and the ion dose in case of ion implantation. SESAMs have been known to exhibit a bi-temporal recovery time [64] with the shortest time in the picosecond or sub-picosecond range. A bi-temporal recovery time is ideal for mode-locked lasers, because the short recovery time enables short pulses and the longer recovery time is needed to initiate mode-locking.

For a more extensive overview of SESAMs see e.g. [60, 65, 66] and for an extensive theoretical and analytical analysis of mode-locking of solid-state and dye lasers with saturable absorbers see e.g. [10, 43, 67, 68].

For fast saturable absorbers with recovery times much faster than the pulse length, the reflection can be modeled by:

$$q(t) = \frac{q_0}{1 + \frac{|A(t)|^2}{P_{SA}}}, \quad (3.3)$$

where q_0 is the non-saturated but saturable loss, $P_{SA} = E_{SA}/\tau_{SA}$ the saturation power, E_{SA} the saturation energy and τ_{SA} the recovery time. For SESAMs where the recovery time is of the order of the pulse length or more, a more ap-

propriate model of the SESAM is [10, 67]:

$$\frac{\partial}{\partial t}q(t) = -\frac{q - q_0}{\tau_{SA}} - q\frac{|A(t)|^2}{E_{SA}}. \quad (3.4)$$

In the limit where $\tau_{SA} \rightarrow 0$ equation 3.4 approaches equation 3.3. The differential equation in equation 3.4 can be numerically integrated to give $q(t)$, and from $q(t)$ the reflection from the SESAM can be calculated as:

$$R(t) = 1 - q(t) - l_0, \quad (3.5)$$

where l_0 is the linear unsaturable loss. Reflection of the slowly varying electric field can then be calculated as $A(t)\sqrt{R(t)}$. The saturation energy can be calculated as the product of the saturation fluence and the effective area on the SESAM. The saturation energy can therefore be decreased by focusing harder on the SESAM.

A general tendency of lasers mode-locked with saturable absorbers of finite recovery times is that the laser may tend to Q-switch mode-lock (i.e. emit a mode-locked pulse train which is highly amplitude modulated on a nanosecond time scale and hence resemble a nanosecond pulse with a mode-locked pulse train underneath the pulse envelope) [68]. The theory derived in reference [68] is quite general but has to be modified for fiber lasers (see e.g. reference [69] for modifications to the theory for a fiber laser working in the soliton regime). The tendency to Q-switch mode-lock is increased if the modulation depth is high. To avoid Q-switched mode-locking, the spot size on the SESAM can either be decreased, or the intra cavity average power increased (by either decreasing the output coupling or by increasing the pump power). However, the limit is set by the damage threshold of the SESAM. If the peak intensity of the pulse is increased above the damage threshold of the SESAM (typically 300 MW/cm²), the SESAM may be permanently damaged, and a small spot burned on the surface.

3.4 Cavity losses

It is important also to include losses in a simulation of a laser. In steady state the cavity losses per round trip are exactly canceled by the gain per round trip, and the intra cavity power hence depends on the losses. In a fiber laser propagation losses inside the fibers are usually negligible, but at intersections between different fibers and especially in the presence of components such as WDMs, couplers, isolators, etc, the losses can be quite large. In fiber lasers the single pass gain can be much larger than usual single pass gains in e.g. solid state lasers. A gain per round trip of 10-20 dB is not unrealistic. Hence much higher cavity losses are also acceptable in fiber lasers. Of course cavity losses should be minimized, as high losses only result in smaller laser outputs. As in other lasers, there is an optimum output coupling depending on the other losses of the cavity, and as the other losses are usually quite high, the optimum output coupling

is also usually quite high. The optimum output power also depends on the position of the output coupler, and highest output powers can be obtained if the output coupler is placed right after the gain medium. For a realistic model of a fiber laser, inclusion of the loss distribution is very important, as the limiting property in fiber lasers is the nonlinear phase shift. The nonlinear phase shift depends on the peak power of the pulse integrated over the cavity, and as the peak power of the pulse depends on the distribution of the losses, the inclusion of these plays an important role on the limit of obtainable output power. Losses (i.e. also wavelength dependent losses) between elements are easily included as a simple multiplication, as the fields are handled in the frequency domain.

3.5 Laser cavity simulations

With the model of all individual elements at hand, a model of a mode-locked fiber laser can be obtained by combining the individual elements in proper order. To find the pulse which is a stable solution to a cavity with a given set of parameters, one should start out with an initially long and noisy pulse, and applying the effect of each element of the laser one at a time. After every round trip, the sequence is simply repeated until the pulse has converged to a stable solution. Depending on the magnitude of the effect of individual elements, convergence may take longer or shorter time. If the wave shaping of some of the elements are strong, sometimes a stable solution can be found in less than 100 round trips, but if the effects are all weak, sometimes more than 10000 round trips are needed. The criteria which has to be fulfilled, to determine if the pulse has reach the steady state is that the pulse should reproduce itself within a phaseshift after every round trip. To check if this criteria is fulfilled, it is advantageous to monitor the root-mean-square (rms) temporal duration, the rms spectral width, the mean central wavelength and the pulse energy [25]. If all these parameters reaches a stable value within machine precision, the pulse is determined to be a stable mode-locked state. Under certain circumstances these parameters do not converge to a stable value but fluctuate around a stable value. In this case the laser is noise-like mode-locked. This usually occurs if the accumulated nonlinear phase shift is much larger than π :

$$\phi_{NL} = \gamma \int_{\text{cavity}} |a(z, t = 0)|^2 dz \gg \pi. \quad (3.6)$$

Real lasers in the noise-like regime may either continue to stay noise-like mode-locked or jump into a state of more than one pulse inside the cavity and thereby reduce the nonlinear phase shift per pulse to less than π . Usually both situations are unwanted and hence the laser should be operated outside the noise-like regime.

The number of data points used to represent the pulse should be chosen so large that both the temporal and spectral windows contain the entire pulse

(within machine precision) at every point in the cavity. 2048-8192 points are usually enough depending on the laser.

Combining the elements in sequence is straight forward, except when the coupling between pulses propagating both directions through the gain medium is included. However, as it is only the average power which saturates the gain medium, the average power of the pulse on each pass through the gain medium can be calculated and stored numerically as a function of position in the gain fiber. The average power of the pulse propagation in the opposite direction can hence be interpolated from the stored values from the previous pass.

3.6 Numerical simulations of a 80 MHz fiber laser

With the developed model at hand, it is now in principle possible to simulate a wide range of different mode-locked fiber lasers. The output from the laser depends on many different parameters, such as fiber characteristics, pump power, the arrangement of the comprising components and cavity length. One parameter is however dominant in the determination of the lasing regime, and this is the net cavity dispersion, $\Delta\beta_2$. In order to illustrate simulations with the numerical model and to illustrate the dependence of net cavity dispersion, calculations on a realistic 80 MHz fiber laser are now presented.

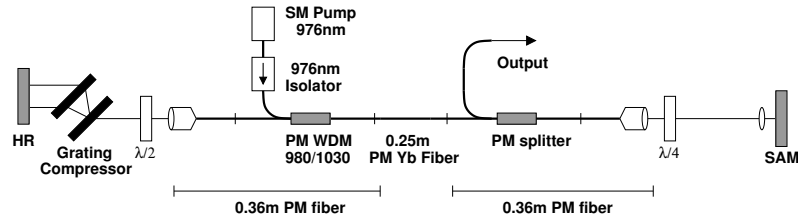


Figure 3.2: Diagram of the laser configuration.

To make the calculations as realistic as possible, the starting point is a laser configuration, as could have been realized in the lab. Figure 3.2 shows a diagram of the laser configuration. The laser is assumed to comprise polarization maintaining (PM) fibers only, and hence the polarization state can be assumed to be linear through out the cavity. The mode-locking mechanism is based on a saturable absorber mirror (SAM) with a modulation depth of 30 %, nonsaturable losses of 15 %, a saturation fluence of $\sim 100 \mu\text{J}/\text{cm}^2$, and a recovery time of 0.5 ps. Output coupling (OC) is taken through a polarization maintaining (PM) splitter and can be tuned by rotating a quarter wave plate. In the numerical simulations an OC of 60 % is used. A grating pair is used for intra cavity dispersion compensation. The total transmission through the grating compressor is assumed to be 70 %. The fiber is modulated with a dispersion of $\beta_2 = 0.024 \text{ ps}^2/\text{m}$, and a nonlinear coefficient of $\gamma = 3.5 \cdot 10^{-3} (\text{m W})^{-1}$ of the passive fiber and $\gamma = 7.4 \cdot 10^{-3} (\text{m W})^{-1}$ of the gain fiber. The lengths of

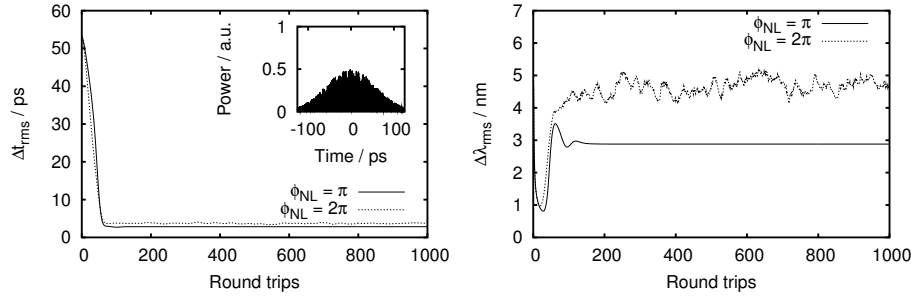


Figure 3.3: Left: Evolution of the rms temporal duration for two different nonlinear phase shifts and $\Delta\beta_2 = 0.02 \text{ ps}^2$. Insert: Input pulse. Right: Evolution of the rms spectral width for two different nonlinear phase shifts.

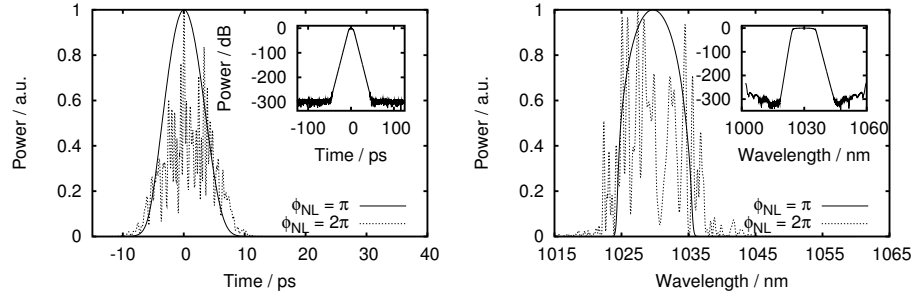


Figure 3.4: Left: Steady temporal shape of a pulse with $\phi_{NL} = \pi$ ($\Delta\beta_2 = 0.02 \text{ ps}^2$) and typical temporal shape of a pulse with $\phi_{NL} = 2\pi$. Right: Steady and typical spectral shapes for the two different nonlinear phase shifts. Inserts: logarithmic scale of the steady shapes corresponding to $\phi_{NL} = \pi$.

the fibers are chosen to be 0.36 m of passive fiber on both sides of 0.25 m gain fiber (ytterbium doped). The gain fiber is assumed to have Gaussian gain profile with a central wavelength at 1030 nm, a width of 40 nm, a peak small signal gain $g_0 = 25 \text{ dB}$ and a variable saturation power corresponding to a variable pump power.

For a given choice of $\Delta\beta_2$, the output depends on the pump power and depending on $\Delta\beta_2$, a higher or lower maximum pump power is acceptable, limited by the total nonlinear phase shift accumulated by the peak of the pulse. As it is usually of interest to operate an oscillator at the highest stable pump power (as this also corresponds to the highest output power), a number of simulations were conducted, where the net cavity dispersions $\Delta\beta_2$ was varied, and for each value of $\Delta\beta_2$, the pump power was adjusted to clamp the nonlinear phase shift at a fixed value: $\phi_{NL} = \pi$ after convergence. Figure 3.3 shows the evolu-

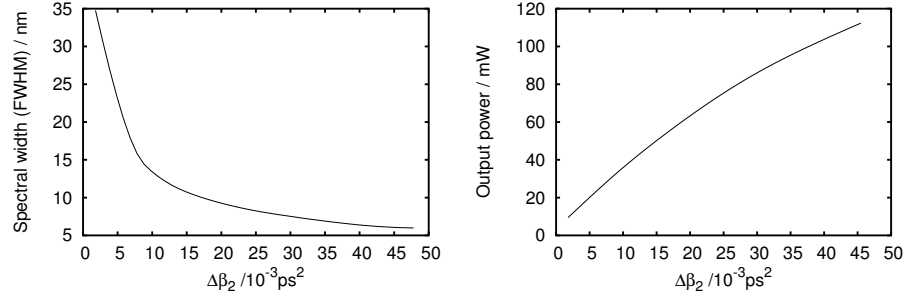


Figure 3.5: Left: Maximum spectral width vs. net cavity dispersion, $\Delta\beta_2$, at a pump power corresponding to a nonlinear phase shift, $\phi_{NL} = \pi$. Right: Maximum output power.

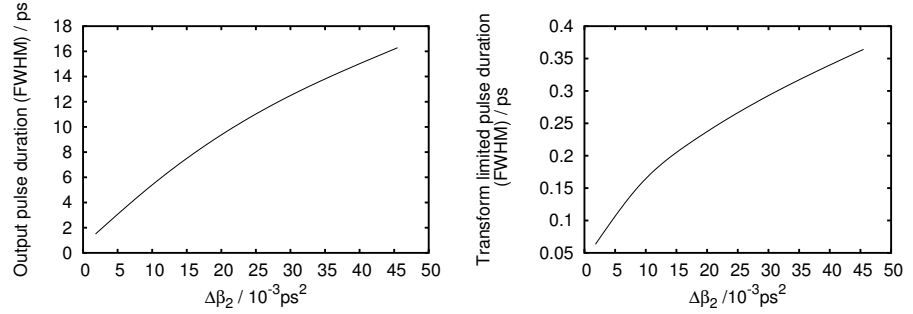


Figure 3.6: Left: Chirped output pulse duration width vs. net cavity dispersion, $\Delta\beta_2$, at a pump power corresponding to a nonlinear phase shift, $\phi_{NL} = \pi$. Right: Transform limited pulse duration after external pulse compression calculated from the spectral width.

tion of the rms temporal duration and spectral width for the particular case of $\Delta\beta_2 = 0.02 \text{ ps}^2$, and figure 3.4 shows the steady temporal and spectral shape of the pulse on both a linear and logarithmic scale. In the insert of figure 3.4 (left) the input pulse can also be seen.

For a total nonlinear phase shift much larger than $\sim \pi$, the calculations do not converge to a stable pulse, but to a noise-like pulse which fluctuates from round trip to round trip. In figure 3.3 the evolution of the rms temporal duration and spectral width can also be seen for the case where the pump power has been increased to give a nonlinear phase shift of $\phi_{NL} \sim 2\pi$ (dotted line). Figure 3.4 also shows a typical output pulses after convergence to the noise like state.

By varying $\Delta\beta_2$ while maintaining $\phi_{NL} = \pi$, trends of the maximum output power, the spectral width, the temporal duration, and the transform limited pulse duration calculated from the spectral width were calculated vs. $\Delta\beta_2$. The

results of the simulations can be seen in figures 3.5-3.6. The trends are clear: at small values of $\Delta\beta_2$, broader spectra, externally compressible to shorter pulses are possible. Also if external compression is not wanted, shortest output pulse durations is obtained for small values of $\Delta\beta_2$. However at smaller values of $\Delta\beta_2$, the maximum output power is also smaller. It is, however, interesting to notice, that at a net cavity dispersion of $\Delta\beta_2 = 0.047 \text{ ps}^2$, the dispersion of the grating compressor is zero, and hence stable mode-locked lasing is obtained without intra cavity dispersion compensation. This property is further investigated in chapter 8.

Calculations have only been carried out for positive values of net cavity dispersion, as the laser enters the soliton regime for negative values of $\Delta\beta_2$. In the soliton regime stable lasing is usually only obtained for much smaller values of nonlinear phase shift (i.e. $\sim 0.1 \pi$) and as the pulse is further almost transform limited inside the laser in the soliton regime, the peak power is also much higher. Therefore high values of ϕ_{NL} are reached at lower output powers.

As with all numerical models, it is important not to forget the real focus: obtaining and understanding experimental results, in order to contribute to the development of physical realizable systems. Therefore the data presented in this section should only be taken as guidelines and illustrations of what might be obtained experimentally. From simulations of the lasers presented in the rest of this thesis it is evident, that the model is quite accurate, and good agreements between simulations and experimental results have been obtained.

CHAPTER 4

Characterization techniques

This chapter describes some of the different developed setups for characterization of mode-locked fiber lasers and fiber components. A setup was developed to measure chromatic dispersion of optical fibers. The setup was used to measure dispersion of the fibers used in all other parts of this work. The setup was paid by and developed on request from NKT-Research and is now used at NKT-Research to measure the dispersion of fibers in their products. The work was done in collaboration with Thomas Vestergaard Andersen. The developed setup for autocorrelation measurements is also introduced, and the theory behind autocorrelation measurements briefly discussed. Finally the concept of polarization maintaining fibers is introduced and a short introduction is given to the measurement of group birefringence in optical fibers.

MEASUREMENT OF FIBER DISPERSION

4.1 Introduction

In the design of mode-locked fiber lasers, knowledge about the dispersion of a fiber is often of key importance. The dispersion influences on the pulse propagation in the fiber. In a cavity it is the net dispersion (the sum of the total dispersion of different sections calculated with sign) which has the strongest influence on the laser output. Although indirect methods exist to estimate the net cavity dispersion, by e.g. looking at the sidebands in the soliton regime [70], or by changing the net dispersion while monitoring the laser output, the best method is to measure the dispersion of each fiber sections separately. In other areas of fiber optics the fiber dispersion is also of key importance. For instance, supercontinuum generation in a nonlinear fiber depends critically on the position of the zero dispersion wavelength (ZDW) and on higher order dispersion terms and knowledge about higher order terms is also of key importance when using a fiber for e.g. four-wave mixing [II] or supercontinuum generation. As shown in chapter 5 knowledge of higher order dispersion terms is also relevant in fiber laser design.

The dispersion of an optical fiber can be measured in several ways. The commercial available systems for the telecommunication industry use the differential phase shift method, where light from a broadband light source is intensity modulated at high frequencies and sent through the fiber [71]. At the end of the fiber, different wavelengths have different phase shifts. The measurement of these different phase delays in the frequency domain relates to a delay in the time domain and, therefore, to the fiber dispersion. Commercial systems are rather expensive and usually limited to telecommunication wavelength range (1530-1625 nm), but exist with the possibility of extended wavelength range (1200-1700 nm). Furthermore, commercial systems require rather long fiber lengths (i.e. $\gg 10$ m). Therefore, it is of interest to look into other less expensive methods, which can be realized in the lab. The femtosecond time-delay technique [72] and the white light interferometry technique [73] are the most used techniques. The femtosecond time-delay technique is based on time of flight experiments but requires a tunable femtosecond laser. The white light interferometry technique is based on a rather simple setup, where the interference signal from a white light source in a Michelson interferometer (with the fiber under test in one arm) can be used to extrapolate the dispersion. In reference [73] the temporal interference signal is measured while scanning the length of the reference arm. A setup based on this technique has previously been developed in our group and is now used at Crystal Fibre to characterize their fibers. The setup only requires measurement of the interference signal with a simple photo diode, but requires very accurate temporal resolution (calibrated by a He-Ne laser in the interferometer) and very high stability over the rather long recording time. As an alternative solution the interference signal can be

measured spectrally with the reference arm fixed [74]. This method requires a optical spectrum analyzer with a high resolution, but reduces the recording time considerably, and hence also the requirement of high stability.

As an optical spectrum analyzer was available to us, the white light interferometry method with signal measurement in the spectral domain was the obvious choice. Furthermore, as the requirements on high stability were somewhat relaxed, it was possible for us to implement the interferometer with fiber pigtailed components. A solution which highly simplifies the use of the setup and the inclusion of the optical spectrum analyzer.

The spectral range of the setup is limited by the the light source. Initially the setup was only intended to be used to characterize fibers close to the emission spectrum of ytterbium, and hence a simple ytterbium ASE (Amplified Spontaneous Emission) source could be used as the light source. Later the setup was modified to use a fiber-pigtailed super continuum source now commercially available from Koheras [75]. This increased the spectral range to ~ 550 -1800 nm.

4.2 Experimental setup

Figure 4.1 shows a diagram of the experimental setup. The ASE source was based on a short piece of ytterbium doped fiber pumped through a WDM with a 150 mW 980 nm diode laser. Lasing was prevented by sending the output through two fiber pigtailed isolators spliced to the interferometer.

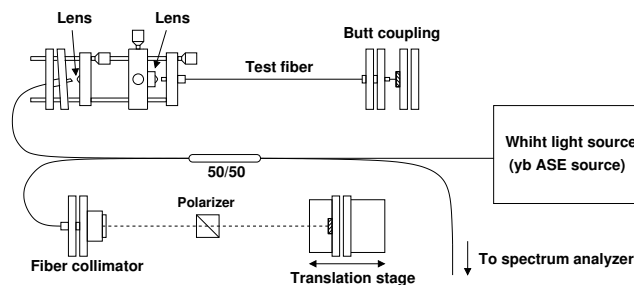


Figure 4.1: Diagram of the experimental setup of the white light interferometer.

The Michaelson-like interferometer was based on a 50:50 fused fiber coupler working as the beam splitter. In one arm the fiber under test could be inserted either by butt-coupling the fiber or by using a lens system to maxi-

mize the coupling between the standard fiber and the fiber under test. This lens setup was primarily used when measuring the dispersion of hollow core photonic bandgap (HC-PBG) fibers as a butt-coupling to such a fiber causes a Fresnel back-reflection at the interface due to different refractive indexes of the cores. The other end of the test fiber was butt coupled to a mirror. In the reference arm, the beam was collimated and reflected on a mirror positioned on a translation stage.

All the fibers in the setup were non-polarization maintaining (non-PM), but by avoiding bending the fibers strongly, a large change in polarization state between the two arms could be avoided. A small difference in polarization state only results in smaller fringes and is acceptable. If the fiber under test was polarization maintaining (PM) a bulk polarizer could be inserted in the reference arm to pick out the polarization state interfering with light from one of the polarization axis of the test fiber. The rotation angle of the polarizer was found by minimizing the beats in the spectral interference pattern.

The choice of a fiber based interferometer resulted in an increased sensitive to environmental perturbations and especially air convection influenced the measurement. The environmental perturbations resulted in a drifting fringe pattern, due to a changing phase difference between the two arms. To minimize this effect, the setup was placed in an air tight box. Due to the fast recording time of the optical spectrum analyzer, a sufficiently slow drift time was easily reached.

If the fibers in the two arms of the interferometer are of different length, it will result in a contribution to the measured dispersion. In addition the coupler and the lens coupling setup will also contribute to the measured dispersion. However, as dispersion of different elements adds linearly, the dispersion of the setup can be measured separately and subtracted and hence the balancing of the dispersion of the two arms is not critical.

As the light source is broadband and incoherent, the optical path length of the two arms must be matched. This is achieved by scanning the stage. Temporally an interference signal can be observed by scanning the stage, and figure 4.2 shows such a signal. The midpoint is referred to as "T=0". When the stage is close to "T=0" interference fringes can be observed in the spectrum.

4.3 Theory

If E_1 and E_2 are the time independent complex electric field amplitudes at the detector of the reference arm and test fiber arm respectively, and if $\phi_1(\omega)$ and $\phi_2(\omega)$ are the accumulated phases in the two arms, then the intensity is given by

$$I(\omega) = |E_1|^2 + |E_2|^2 + 2E_1E_2 \cos(\phi_2(\omega) - \phi_1(\omega)).$$

The frequency dependent phase difference contains a contribution from the setup, a contribution from the test fiber and a contribution from the free space section

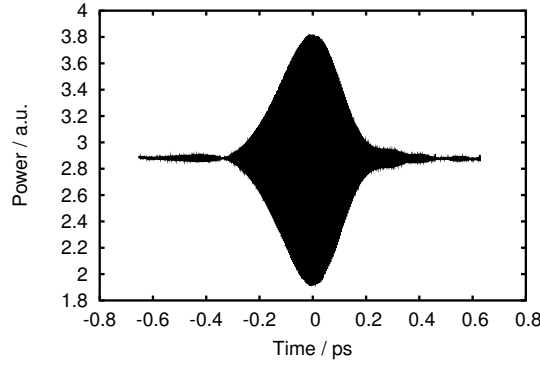


Figure 4.2: Temporal signal from the white light setup around the "T=0" point.

in the reference arm:

$$\Delta\phi(\omega) \equiv \phi_2(\omega) - \phi_1(\omega) = \Delta\phi_s(\omega) + \phi_f(\omega) - \frac{\omega}{c}d, \quad (4.1)$$

where d is the distance between the "T=0" point of the setup without test fiber and the "T=0" point with the fiber. $\Delta\phi(\omega)$ can be measured modulus 2π by measuring the spectral position of the fringes. The distance between two successive fringes corresponds to an increase or decrease in $\Delta\phi(\omega)$ of 2π . If the second derivative of the phase difference with respect to frequency is calculated, the contribution from the stage position disappears:

$$\frac{\partial^2}{\partial\omega^2}\Delta\phi(\omega) = \frac{\partial^2}{\partial\omega^2}\Delta\phi_s(\omega) + \frac{\partial^2}{\partial\omega^2}\phi_f(\omega).$$

$\frac{\partial^2}{\partial\omega^2}\Delta\phi_s(\omega)$ can be calculated from a separate but similar measurement without test fiber and subtracted from $\frac{\partial^2}{\partial\omega^2}\Delta\phi(\omega)$. The last term relates directly to the dispersion of the fiber:

$$\frac{\partial^2}{\partial\omega^2}\phi_f(\omega) = 2\beta_2(\omega)L,$$

where L is the length of test fiber, and β_2 is the group velocity dispersion. Once $\beta_2(\omega)$ is known, the usual dispersion parameter is easily calculated from the equation:

$$D = -\frac{2\pi c}{\lambda^2}\beta_2.$$

Higher order dispersion terms are contained in $\beta_2(\omega)$ and are found by expanding $\beta_2(\omega)$ around a center frequency ω_0 :

$$\beta_2(\omega) = \beta_2(\omega_0) + \beta_3(\omega_0)(\omega - \omega_0) + \frac{1}{2}\beta_4(\omega_0)(\omega - \omega_0)^2 + \dots \quad (4.2)$$

The propagation constant, $\beta(\omega)'$, which was introduced in equation 2.19 as a parameter in the nonlinear Schrödinger equation, and is relevant for laser cavity calculations, can now be found by integrating equation 4.2 twice:

$$\beta(\omega)' = \frac{1}{2}\beta_2(\omega_0)(\omega - \omega_0)^2 + \frac{1}{6}\beta_3(\omega_0)(\omega - \omega_0)^3 + \frac{1}{24}\beta_4(\omega_0)(\omega - \omega_0)^4 + \dots \quad (4.3)$$

where the integration constants have been set to zero, as they only correspond to a change of linear phase and a translation of the pulse on the time axis and hence are not relevant for the slowly varying envelope.

4.4 Dispersion measurements

To illustrate how the calculations are made, an example based on a hollow core photonic bandgap fiber (HC-PBG) fiber from Crystal Fibre is presented below. Figure 4.3 (left) shows a cross section of the fiber, and figure 4.3 (right) the transmission spectrum.

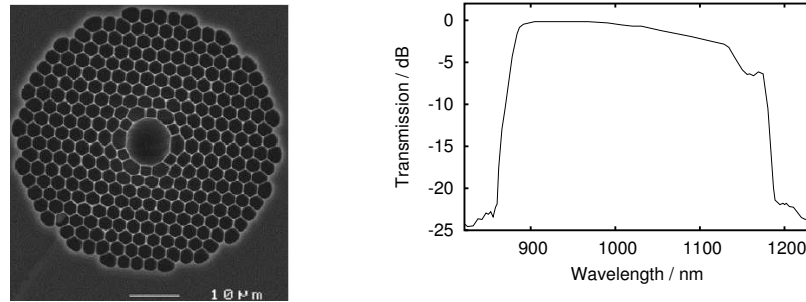


Figure 4.3: Left: SEM image of the cross section of the HC-PBG fiber. Right: Transmission spectrum through 2 m of the HC-PBG fiber.

The fiber is interesting because it has negligible nonlinearity and a high anomalous dispersion at 1030 nm and as shown in chapter 5 it can be used for pulse compression after external amplifications of a fiber laser without degrading pulse quality. Figure 4.4 shows a typical spectrum with interference fringes.

The phase difference can be constructed by noting that the phase must have increased or decreased with 2π at the peak of each fringe. As the $\Delta\phi(\omega)$ contains a quadratic term (the GVD), it will as a function of frequency have a local extremum point. By changing the linear term in eq. 4.1 (e.g. by moving the stage), the position of the extremum point can be moved. This turning point can be seen in figure 4.4 close to 1040 nm. The position of the turning point does not influence on the dispersion, but is usually best placed in the middle of the spectrum in order to get maximum resolution on the fringes. The sign

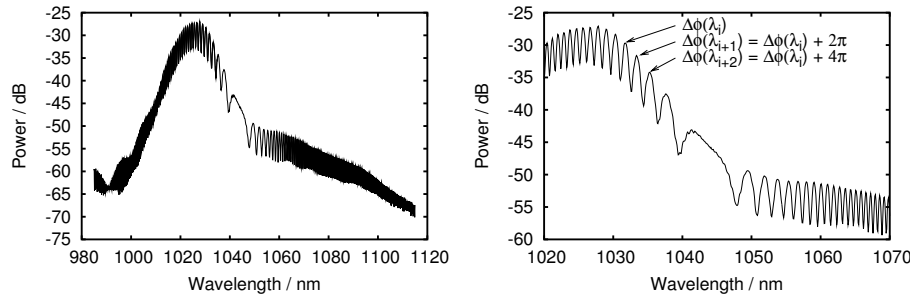


Figure 4.4: Left: Measured spectrum with interference fringes. The position of the turning point is found around 1040 nm where the slow modulation reveals that the linear term in the phase difference is zero. Right: Zoom on the region around 1045 nm. The phase difference can be constructed by adding 2π at each local maximum.

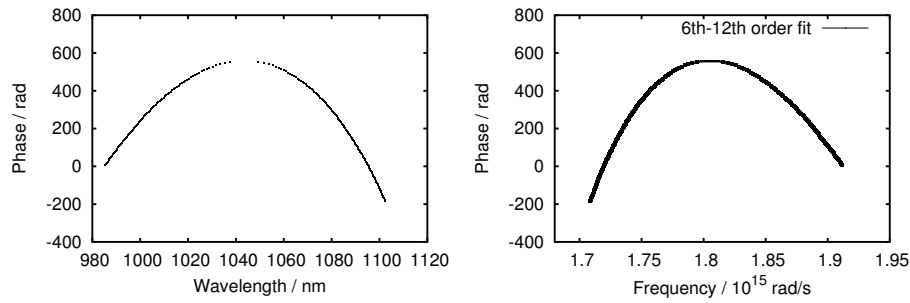


Figure 4.5: Left: Phase versus wavelength. Right: Phase versus frequency. Six polynomial fits of order 6 to 12 are shown, and all fit the the measured points well.

of the quadratic term in $\Delta\phi(\omega)$ can be found by noting that if the length of the stage arm is increased (linear term in eq. 4.1 decreased), the turning point will move towards longer wavelengths (lower frequencies) if the GVD is negative and towards shorter wavelengths if the GVD is positive. The resulting phase difference can be seen in figure 4.5.

The second derivative of the phase difference is found by fitting a polynomial to $\Delta\phi(\omega)$ and deriving it twice. The order of the polynomial must of course be chosen large enough, that the polynomial coincides with the measured points over the entire frequency range. Figure 4.5 (right) shows polynomial fits of order 6 to 12 to $\Delta\phi(\omega)$. For this particular measurement, polynomials of order higher than 5 gives accurate fits within the measured range. The resulting dispersions originating from the 6 different polynomials can be seen in figure 4.6 (left). As

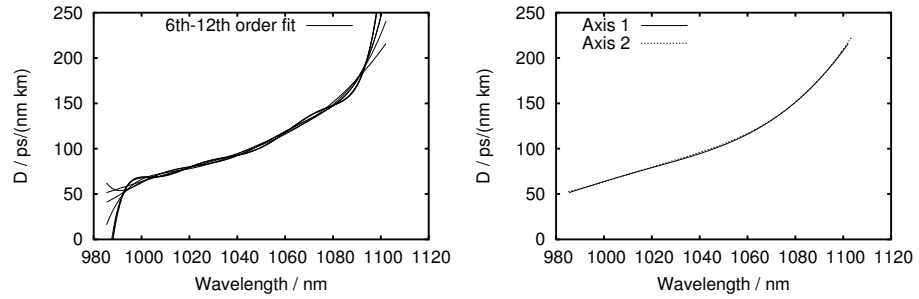


Figure 4.6: Left: The calculated dispersion of the HC-PBG fiber for the 6 different polynomials. The curves almost coincide in the middle of the interval while they differ significantly at the edges. Right: Dispersions of the two polarization axes of the fiber.

can be seen, the calculated dispersion depends on the order of the polynomial. However in the middle $\sim 80\%$ of the measured interval, the curves coincide within an acceptable uncertainty. Only at the edges, the dispersion is inaccurately determined. However, as it is unlikely that the slope of the dispersion changes drastically near the edges of the measured interval, one can choose the polynomial of lowest order, which also fits the data. In this case: order 6. The accuracy of the setup was tested by measuring the dispersion of well-known fibers such as SMF28 [76] and HI1060 Flexcore [77], and in both cases excellent agreement with known values were found.

The HC-PBG fiber was observed to be birefringent and the dispersion of both polarization axes were measured. Figure 4.6 (right) shows the measured dispersions of the two axes. The dispersion was found to be indistinguishable.

Even though the setup based on the ytterbium ASE source is well suited for measurements of the dispersion of components for ytterbium based fiber lasers in the relevant wavelength range, other applications require dispersion measurements over a broader range. For this purpose the ASE source was replaced with a super continuum white light source [75]. The super continuum is created in a nonlinear photonic crystal fiber (PCF) pumped at 1060 nm with a Q-switched laser. The nonlinear fiber could be spliced directly to the setup with low loss. In order to compensate for the limited bandwidth of the 2x2 50:50 coupler it was replaced by two 1x2 50:50 thin film couplers and the Michelson-like interferometer was changed into a Marc-Zender interferometer. With this approach more power was lost but by combining the two 1x2 couplers so that identical arms of the couplers were put in opposite arms of the interferometer, a coupling ratio far from the perfect 50:50 became acceptable and the setup could be used over the entire wavelength range of the super continuum source.

To illustrate the broad measurement range of the setup, the dispersion measured from 900-1300 nm of a nonlinear PCF and the dispersion measured from

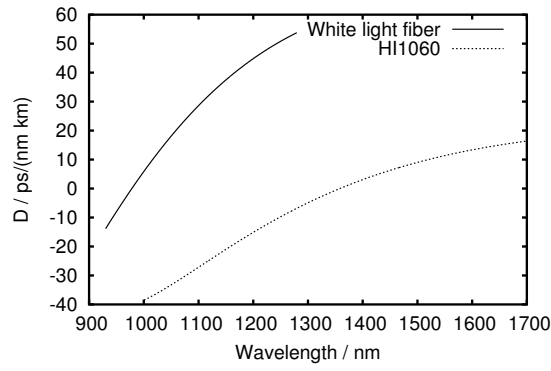


Figure 4.7: Measured dispersion of a nonlinear PCF with a ZDW at 975 nm and of a HI1060 Flexcore fiber.

1000-1700 nm of a HI1060 Flexcore fiber can be seen in figure 4.7. The standard fiber, HI1060, exhibits a high normal dispersion (i.e. $D < 0$) around $1 \mu\text{m}$, and the nonlinear PCF has a blue shifted ZDW at 975 nm and hence exhibits anomalous dispersion around $1 \mu\text{m}$. The setup has further been used to measure the dispersion of the solid core photonic bandgap fibers used in chapter 5.

AUTOCORRELATION MEASUREMENTS

4.5 Introduction

Experimentally, it is often important to be able to determine the duration of a pulse. The fundamental limit in pulse duration is set by the spectral width (and shape) of the pulse. This limit is known as the Fourier limit or transform limit, as it can be found by Fourier transforming the spectrum with zero phase. However, a pulse may have a nonlinear chirp which cannot be removed with simple dispersive elements such as prism or grating pairs. This results in a longer minimum pulse duration. As pulses from mode-locked lasers are often so short (i.e. $\ll 30$ ps), that even the fastest photo diodes cannot resolve the temporal shape of the pulse, an alternative approach has to be taken. The temporal duration of a pulse can be extrapolated by measuring the interference signal of the pulse with another short pulse as function of delay between the two pulses. Most conveniently, a pulse can be interfered with itself. The setup for this measurement is known as an autocorrelator, and the output as an autocorrelation trace.

4.6 Setup and theory

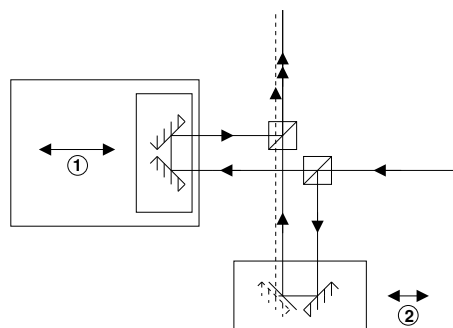


Figure 4.8: Diagram of the autocorrelator. The delay can be changed by scanning stage 1. By moving stage 2, the autocorrelator can be changed from interferometric to background free.

An autocorrelator is based on a Michelson interferometer, which splits the pulse into two pulses: one in each arm. The two pulses are recombined with an added temporal delay. Figure 4.8 shows a diagram of the Michelson interferometer which was built to make autocorrelation measurements. One arm of the autocorrelator could be scanned up to 350 ps, and was controlled by a computer. This enables both high resolution autocorrelation measurements and long range autocorrelation traces. With this autocorrelator, both interferometric

autocorrelation traces (overlapped beams) and background free autocorrelation traces (parallel but not overlapped beams) could be measured. To get an second order autocorrelation trace, the intensity must be squared. The easiest way to measure the interferometric autocorrelation trace is to use two-photon absorption on the surface of a photo diode which cannot see photons at the laser wavelength, λ_0 , but only with wavelength $\lambda_0/2$. In the range 680-1360 nm, a GaAsP photo diode is appropriate [78], and such a photo diode (Hamamatsu G1117) was used for the interferometric autocorrelation traces. For a background free autocorrelation trace, the beams must be crossed by focusing the two parallel beams with the same lens into a nonlinear crystal (e.g. a BBO crystal). On the output side three beams emerge. The middle one is the background free autocorrelation trace. The advantage of the background free autocorrelator is that it is easier to extract the pulse duration directly from the trace. The disadvantage on a daily basis is that it is more difficult to check if the autocorrelator is properly aligned. If the autocorrelator is not aligned correctly and one beam drifts as the delay is scanned, the background free autocorrelation trace can indicate a pulse duration which is shorter than the actual pulse duration.

The second order interferometric autocorrelation function is calculated as:

$$G_2(\tau) = \int_{-\infty}^{\infty} |(E(t) + E(t - \tau))^2|^2 dt, \quad (4.4)$$

where τ is the variable delay between the pulses, and $E(t) = A(t) \exp(-i\omega_0 t)$. For the case of a chirped Gaussian pulse (see equation 2.35) the autocorrelation trace can be calculated analytically:

$$\begin{aligned} G_2(\tau) \propto & 1 + 2 \exp\left(-\frac{2 \ln(2)}{1+C^2} \left(\frac{\tau}{t_0}\right)^2\right) \\ & + 4 \exp\left(-\frac{2 \ln(2)}{1+C^2} \frac{3+C^2}{4} \left(\frac{\tau}{t_0}\right)^2\right) \cos\left(\frac{\ln(2)C}{1+C^2} \left(\frac{\tau}{t_0}\right)^2\right) \cos(\omega_0 \tau) \\ & + \exp\left(-2 \ln(2) \left(\frac{\tau}{t_0}\right)^2\right) \cos(2\omega_0 \tau). \end{aligned} \quad (4.5)$$

An important ratio when aligning an interferometric autocorrelator is the ratio between the top of the autocorrelation trace and constant background:

$$G_2(0) : G_2(\infty) = 1 : 8. \quad (4.6)$$

Only if this ratio is fulfilled are the measured pulse durations trustworthy. Notice that $G_2(\tau)$ consists of four terms: a constant term, a Gaussian term with no oscillations, a Gaussian term oscillating with ω_0 and finally another Gaussian term oscillating with $2\omega_0$. In the limit of $C = 0$, all three Gaussian terms have similar widths, but in the limit where C is large, the width of the first Gaussian term exceeds the widths of the other terms. The top and bottom envelopes of the autocorrelation function are easily found by replacing $\cos(\omega_0 \tau) \rightarrow 1$, $\cos(2\omega_0 \tau) \rightarrow 1$ (top envelope) and $\cos(\omega_0 \tau) \rightarrow -1$, $\cos(2\omega_0 \tau) \rightarrow 1$ (bottom envelope) respectively in equation 4.5.

Figure 4.9 (left) shows the interferometric autocorrelation trace of a 100 fs pulse with zero chirp ($C = 0$), and figure 4.9 (right) shows the trace of a 100 fs pulse with a chirp of ($C = 27.7$) corresponding to propagation through 5 m of standard fiber at 1030 nm.

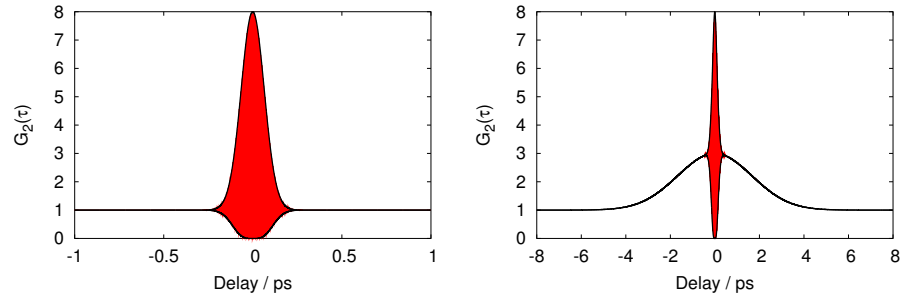


Figure 4.9: Left: Calculated autocorrelation trace of a 100 fs pulse with zero chirp ($C = 0$). Right: autocorrelation trace of a 100 fs pulse with a chirp of ($C = 27.7$) corresponding to propagation through 5 m of standard fiber at 1030 nm. Black curves: envelopes of the autocorrelation traces.

The background free autocorrelation trace is simply given by the non oscillating Gaussian term in $G_2(\tau)$, which can also be found from:

$$\begin{aligned} G'_2(\tau) &= \int_{-\infty}^{\infty} |E(t) \cdot E(t - \tau)|^2 dt \\ &\propto \exp\left(-\frac{2 \ln(2)}{1 + C^2} \left(\frac{\tau}{t_0}\right)^2\right) \end{aligned} \quad (4.7)$$

The ratio between the FWHM of the background free autocorrelation trace and the FWHM pulse duration is known as the deconvolution factor, and this depends on the temporal shape of the pulse. For a Gaussian pulse the deconvolution factor is simply $\sqrt{2}$. For a transform limited pulse with parabolic spectrum, the deconvolution factor is 1.33. For a transform limited Gaussian pulse ($C = 0$) the deconvolution factor between the FWHM of the top envelope of the interferometric autocorrelation trace and the FWHM pulse duration is 1.54. For pulses of unknown temporal shape and/or of unknown chirp (or even with higher order chirp), the best approach is to measure the power spectrum and Fourier transform the square root of this. The square of the Fourier transform is then the transform limited pulse and from this the autocorrelation trace can be calculated and compared to the measured autocorrelation trace. If the two traces coincide, the pulse duration is equal to the pulse duration of the calculated transform limited pulse. Otherwise a pulse retrieval algorithm can be used to match the calculated and measured traces by numerically adding chirp to the pulse.

An autocorrelation trace can be deceiving, as the detector averages the autocorrelation trace of many individual pulses. If all the pulses in the pulse train

are identical, there is no problem, as the average trace is then identical to the individual trace. However, if there are large fluctuations from pulse to pulse, the average trace may resemble that of figure 4.9 (right), but instead of indicating a chirped pulse which can be compressed by applying an appropriate amount of dispersion, the pulses could also be incompressible, as the phases of the individual pulses may be different and even very noisy. In fact figure 4.10 shows the numerically calculated autocorrelation trace averaged over 1000 round trips of the noise-like mode-locked state from the example at the end of chapter 3. This trace is indistinguishable from a trace of a noise-free but chirped mode-locked output.

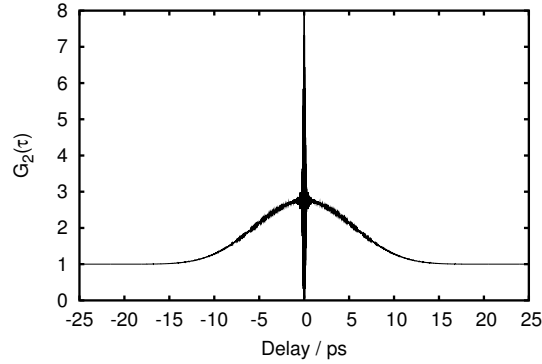


Figure 4.10: Autocorrelation trace of a noise-like mode-locked output.

To distinguish between noise-free chirped pulses and of noise-like pulses, other factors have to be taken into account. For example the spectral shape can be compared to calculated spectral shapes which differs if the pulses are noise-like. In the normal dispersion regime, the spectra tends to have very steep edges if the laser is noise-free, whereas noise-like mode-locking leads to Gaussian-like spectra. Alternatively the amplitude noise can be measured with an RF-spectrum analyzer. The ultimate test is however, if the pulses are externally compressible with e.g. a grating compressor.

MEASUREMENT OF GROUP BIREFRINGENCE

4.7 Polarization maintaining fibers

In a fiber with perfect hexagonal symmetry (or any higher than twofold rotational symmetry) two orthogonal polarized modes will be degenerate [79]. On the other hand, if the fiber is constructed to be asymmetric, so that it only has twofold rotational symmetry the propagation constants of two orthogonal polarized (i.e. linear polarized) modes, β_x and β_y , will in general be different, and the fiber is said to be birefringent. Birefringence is typically obtained through either form birefringence (asymmetric core shapes) or stress induced birefringence (by embedding stress rods in the material with different thermal expansion coefficients and hence incorporating a strain in the material).

If the propagation constants are expanded around a frequency, ω_0 :

$$\beta(\omega) = n(\omega) \frac{\omega}{c} = \beta_0 + \beta_1(\omega - \omega_0) + \beta_2(\omega - \omega_0)^2 + \dots, \quad (4.8)$$

where:

$$\beta_k = \left(\frac{\partial^k \beta}{\partial \omega^k} \right), \quad (4.9)$$

then β_0 and β_1 are related to the phase and group velocity respectively:

$$\beta_0 = \frac{\omega_0}{v_p} = n(\omega_0) \frac{\omega_0}{c} \quad (4.10)$$

$$\beta_1 = \frac{1}{v_g} = \frac{n_g}{c} = \frac{1}{c} \left(n(\omega_0) + \omega_0 \frac{\partial n}{\partial \omega}(\omega_0) \right) \quad (4.11)$$

where v_p is the phase velocity, v_g the group velocity, and n_g the group index. Physically speaking, the envelope of an optical pulse moves at the group velocity, while the phase underneath the envelope moves at the phase velocity. In a birefringent fiber both the β_0 and β_1 term will in general differ for the two different polarization directions. As shown in section 4.4, the group velocity dispersion, β_2 , and higher order terms can often be assumed to be identical for the two orthogonal polarization directions.

The group birefringence, Δn_g , is defined as: $\Delta n_g = |n_{g,x} - n_{g,y}|$ and knowledge about the group birefringence is important when working with pulse propagation in birefringent fibers, as it determines the walk-off between pulses launched in the different axis of the fiber.

In general the birefringence of a fiber is also an important property when designing mode-locked fiber lasers. If a fiber is birefringent, then light polarized only along one axis of the fiber is prohibited from coupling into the other polarization axis. This is true even if the fiber is twisted, so that the polarization axis turns along its length. If the twist is sufficiently slow, the light can gradually rotate its polarization state together with the polarization axis of the fiber.

Hence highly birefringent fibers are usually known as polarization maintaining (PM) fibers, and can for example be used to control the polarization state inside a fiber laser. For an overview of conventional PM fibers see reference [80]. The conventional PM fibers used in later chapters of this thesis are all PANDA fibers, and the birefringence in a PANDA fiber originates from two stress rods. Figure 4.11 shows a diagram of the cross section of the fiber.

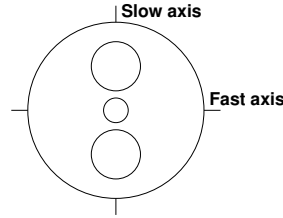


Figure 4.11: Cross section of a PANDA PM fiber.

In low birefringent or non-birefringent fibers stress applied to the fiber (e.g. by bending it) induces a birefringence which also affects the polarization state of the light. If the induced birefringence is comparable to or larger than the intrinsic birefringence, the fiber is known as a non-PM fibers. When working with long segments of fiber, i.e. longer than $\sim 0.5 - 1$ m, it is difficult to avoid bends on the fiber and hence uncontrollable polarization evolution. However, linear polarization evolution can be compensated by wave-plates on the output side. The real problem arises from thermal or air-convection induced changes of the bend induced birefringence of the fiber. This leads to a polarization evolution which is unstable over time, and is hence referred to as environmentally unstable. Environmentally stable polarization evolution can hence only be obtained with the use of PM-fibers. Environmentally stable fiber laser based on PM-fibers only will be the subject of chapter 6. However, schemes exist which intrinsically eliminate the linear polarization evolution of non-PM fibers and hence also the environmental instability. In chapter 9 such a scheme is investigated as an alternative approach to creating environmentally stable fiber lasers.

4.8 Measurement of the group birefringence

The group birefringence can be measured with the so-called crossed polarizer technique [81, 82]. If linearly polarized light is launched into a PM fiber with an angle of 45° between the polarization axis of the light and the axis of the fiber, the polarization state of the light emitted from the other end of the fiber will depend on the phase difference between the two axes: $\Delta\phi = \Delta\beta L$, where L is the length of the fiber. If the emitted light is transmitted through a polarizer also at an angle of 45° to the axis of the fiber, the transmission will depend on this phase shift. Only if $\Delta\phi = 2\pi$ will the transmission be maximum. If the fiber is birefringent, $\Delta\phi$ depends on the wavelength of the light and if the light

transmitted through the fiber is from a broadband light source, the transmitted spectrum will have spectral fringes. The group birefringence can be found from these spectral fringes, by noting that:

$$\frac{\partial}{\partial \lambda} \Delta \phi = -\frac{2\pi c}{\lambda^2} L \frac{\partial}{\partial \omega} \Delta \beta = -\frac{2\pi}{\lambda^2} L \Delta n_g. \quad (4.12)$$

The distance between two successive fringes corresponds to an increase in $\Delta \phi$ of 2π , and hence:

$$\Delta n_g = \frac{\lambda^2}{L \Delta \lambda}, \quad (4.13)$$

where $\Delta \lambda$ is the fringe separation.

To exemplify the method, the group birefringence of the HC-PBG fiber used in chapter 5 (shown in figure 4.3) was measured. An ytterbium ASE source was used as light source and a fringe separation of 10.3 nm was measured at 1030 nm on a 3.34 m long piece of fiber. This corresponds to a group birefringence of $3.1 \cdot 10^{-5}$ and a group velocity mismatch of 103 fs/m. In contrast to standard PM fibers, the birefringence in this fiber is a result of a deviation from the intended symmetric shape.

4.9 Summary

In summary three different setups for characterization of mode-locked fiber lasers and fiber components have been presented. The setup for measurement of fiber dispersion have been applied to measure the dispersion of all the fibers used in the mode-locked lasers in this thesis. The autocorrelator was used to characterize the outputs from the constructed lasers, and finally the setup for measurement of group birefringence have been used to verify the birefringence of the HC-PBG fiber used in chapter 5 and to calculate group velocity mismatch in the PM fiber used in chapter 9 for environmentally stable nonlinear polarization rotation in an all-PM mode-locked fiber laser.

CHAPTER 5

Solid core photonic bandgap fiber laser

This chapter describes the results of the first mode-locked fiber laser using solid-core photonic bandgap (SC-PBG) fiber for intra cavity dispersion compensation. Limitations in terms of obtainable pulse durations have been explored, and was found to be limited by the high third order dispersion of the SC-PBG fiber. After external amplification and external compression in a hollow-core photonic bandgap (HC-PBG), 158 fs 5.3 nJ pulses were obtained at a central wavelength of 1030 nm from this very compact all-fiber based system, and the result is a significant step toward a femtosecond ytterbium based fiber laser system with no sections of free space optics. The SC-PBG fiber was spliced to a standard fiber, and hence enables fiber oscillators without sections of free-space optics.

5.1 Introduction

Standard fibers have a large normal dispersion at the lasing wavelength of ytterbium and one of the main problems using ytterbium as gain media in fiber lasers is the lack of fiber components with anomalous dispersion at this wavelength. Because of the high dispersion of standard fibers, dispersion compensating elements are necessary in fiber lasers to obtain broad spectra, which can result in short femtosecond pulses. Otherwise the spectrum narrows and only longer pulses are possible.

The laser presented in chapter 6 uses a bulk transmission grating pair for intra cavity dispersion compensation. Although compact and stable, a transmission grating excludes the possibility of making an implementation with no free space sections. All-fiber implementations are preferable, as it increases the stability, compactness and possibly reduces the cost.

A very elegant fiber based solution is the use of a chirped fiber Bragg Grating. Dispersion compensation in fiber lasers based on chirped fiber Bragg grating has been researched since the mid-nineties [83] and recently a very elegant and compact all-fiber 100 fs, 4 nJ system based on a transmitting chirped fiber Bragg grating as output coupler, and an amplifier pumped with the same pump single-mode fiber-pigtailed diode as the oscillator, has been demonstrated by IMRA [84].

An alternative solution to fiber based intracavity dispersion compensation is the use of photonic bandgap fibers (PBGs). As opposed to normal fibers where light is bound due to a higher refractive index of the core compared to the surrounding cladding, bound modes in PBGs are found due to a photonic bandgap in a micro structured cladding with a higher average index than the core. A guidance band is created in the core where light of certain wavelengths is not allowed to penetrate into the cladding [18]. This spectral guidance band of PBGs is usually quite narrow and the dispersion of PBGs is strongly affected by the high loss at the edges of the guidance band. The dispersion changes from highly normal close to the short wavelength edge to highly anomalous near the long wavelength edge, with a zero dispersion wavelength in between. By scaling the transverse dimensions of the fiber the position of the spectral transmission band can be moved and anomalous dispersion at any wavelength is in principle possible. Hollow-core photonic bandgap (HC-PBG) fibers have existed for some years now [18] and quite recently solid-core photonic bandgap (SC-PBG) fibers have also been demonstrated [85, 86]. Using PBG fibers for dispersion compensation has the advantage that the anomalous dispersion of the cavity can be changed simply by changing the length of the PBG fiber. Furthermore, PBG fibers can be manufactured in lengths (i.e. > 100 m), sufficient for many mode-locked lasers and hence the use of PBG fiber potentially simplifies mass-production.

Previously mode-locked fiber lasers have been demonstrated with the use of standard photonic crystal fibers (PCFs) [87] and HC-PBG fibers [88]. HC-PBG

fibers have also previously been used to realize all-fiber chirped-pulse amplification systems [89, 90]. PCFs and HC-PBG fibers have some disadvantages when used for intra cavity dispersion compensation. The main problem with PCFs is the small core size which is necessary to achieve anomalous dispersion. As a result these fibers have a high nonlinear coefficient, which is less attractive as it limits the obtainable pulse energy. HC-PBG fibers have a very low nonlinear coefficient and can be spliced to standard fibers with low loss, but the splice introduces a Fresnel reflection at the interface due to the different refractive indexes of the cores. Single-pulse mode-locking cannot be obtained if the cavity contains such Fresnel reflections and these fibers are therefore not attractive for realizations of lasers with no sections of free space optics.

In this chapter a mode-locked laser using a solid-core photonic bandgap (SC-PBG) fiber for dispersion compensation is presented. Simultaneous to the submission of our paper [VII], results on a similar oscillator using SC-PBG fiber for dispersion compensation were also submitted by Isomaki and Okhotnikov [91]. These two results were the first demonstrations of the use of a SC-PBG fiber for dispersion compensation in mode-locked fiber lasers. In [91] a minimum pulse duration of 460 fs was obtained by operating the oscillator in the net anomalous (soliton) dispersion regime. Here 158 fs pulse duration from a fiber oscillator, fiber amplifier and fiber compressor system is demonstrated. This oscillator was operated in the net normal dispersion regime to explore the limits in spectral width and pulse duration set by the high total third order intra cavity dispersion. Transform limited pulses were obtained through nonlinear pulse propagation in the amplifier, and subsequent pulse compression in a HC-PBG fiber with negligible nonlinearity.

5.2 Fiber characterization

The SC-PBG and HC-PBG fibers used to realize the femtosecond laser system were manufactured at Crystal Fibre. The HC-PBG fiber was manufactured from pure silica, creating a cladding with air-holes surrounding the hollow core. The SC-PBG fiber was composed of an array of Ge-doped rods embedded in a silica matrix surrounding a silica core. Cross sections of the HC-PBG and SC-PBG fiber can be seen in figure 5.1.

The dispersion of the PBGs was measured using the setup described in chapter 4. Figure 5.2 (left) shows the measured dispersion. The dispersion of the SC-PBG fiber was measured to: $\beta_2 = -0.085 \text{ ps}^2/\text{m}$, $\beta_3 = 1.7 \cdot 10^{-3} \text{ ps}^3/\text{m}$ at 1030 nm. The dispersion of the HC-PBG fiber was measured to: $\beta_2 = -0.049 \text{ ps}^2/\text{m}$, $\beta_3 = 3.1 \cdot 10^{-4} \text{ ps}^3/\text{m}$ at 1030 nm and the dispersion of the standard fiber was measured to $\beta_2 = 0.023 \text{ ps}^2/\text{m}$, $\beta_3 = 3.9 \cdot 10^{-5} \text{ ps}^3/\text{m}$ at 1030 nm. The third order dispersion (TOD) of the SC-PBG fiber is almost an order of magnitude larger than the TOD of the HC-PBG and almost two orders of magnitude larger than the TOD of the standard fiber. The large TOD of the SC-PBG is a consequence of the solid core, contributing with normal GVD. To obtain anomalous

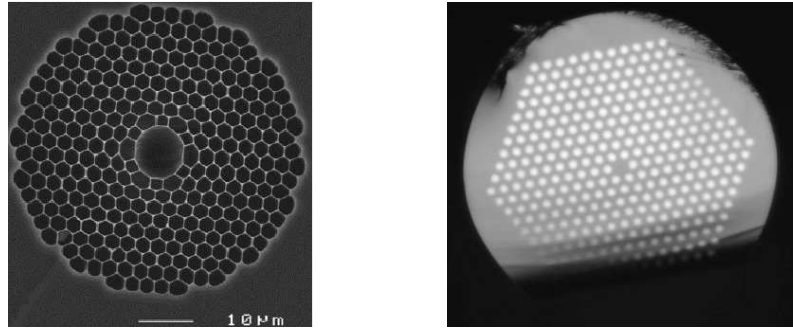


Figure 5.1: Left: SEM image of the cross section of the HC-PBG fiber. Right: Cross section of the SC-PBG fiber.

GVD at a certain wavelength, the long wavelength edge of the transmission band has to be moved closer as the waveguide contributes with a larger anomalous GVD here. The TOD, however, is also larger here and as a consequence the resulting TOD will be higher. The mode field diameter (MFD) of the SC-PBG fiber was $8 \mu\text{m}$ and hence the fiber has a lower nonlinear coefficient compared to the standard fiber (MFD = $6 \mu\text{m}$). The HC-PBG fiber was observed to be birefringent and the group birefringence of the fiber was measured to be $\Delta n_g = 3.1 \cdot 10^{-5}$ with the setup described in chapter 4. The dispersion of both polarization axes was indistinguishable. The SC-PBG fiber on the other hand was not observed to be birefringent.

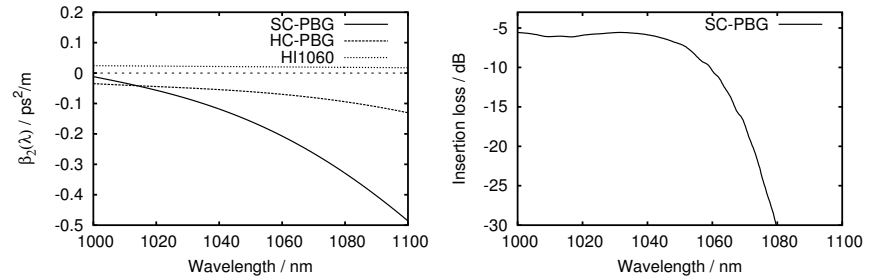


Figure 5.2: Left: Dispersion of the SC-PBG, HC-PBG and standard fiber. Right: The insertion loss of the 0.36 m long SC-PBG fiber.

5.3 Laser design

Figure 5.3 shows a diagram of the laser system. The cavity of the oscillator consists of a WDM, 8.5 cm of highly doped ytterbium fiber (1200 dB/m absorption

at 976 nm), a PM 20:80 coupler with PM fiber pigtails (output coupling: 20 %) and 0.36 m of SC-PBG fiber. The coupler also works as a polarizer, transmitting only the light in the slow axis (extinction ration: 24 dB) and this thereby ensures that the output from the cavity is linearly polarized. The total length of fibers in the cavity was 1.79 m. The non-PM fibers of the cavity were all kept straight in order to avoid polarization rotation. It is, however, unavoidable that a small amount of light is coupled into the fast axis of the fiber pigtails of the coupler, but this is not a problem as light coupled to the fast axis is terminated at the coupler.

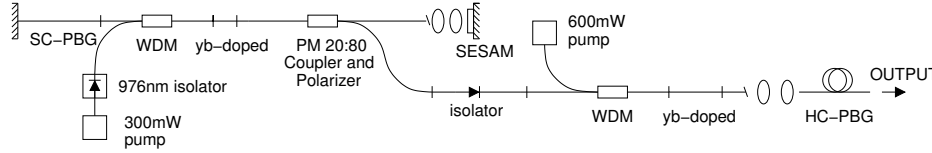


Figure 5.3: Diagram of the laser system.

One end of the SC-PBG fiber was spliced to a standard fiber using a standard Ericsson Fusion splicer. The other end of the fiber was butt-coupled to a high reflecting dielectric mirror. The insertion loss of the SC-PBG fiber can be seen in Fig. 5.2 (right). The long wavelength edge of the transmission band is clearly visible > 1060 nm. The insertion loss includes the double pass through the fiber and the double loss at the interface between the standard fiber and the SC-PBG fiber. The high loss was found to be a combination of not only mismatched MFDs but also a high propagation loss in the SC-PBG fiber. In spite of the high intra cavity losses, lasing is possible due to the high single pass gain of ytterbium. A smaller insertion loss is believed to be possible through further fiber design optimization.

A saturable absorber mirror (SESAM) with a modulation depth of 24 %, a recovery time of < 500 fs, a saturation fluence of $\sim 70 \mu\text{J}/\text{cm}^2$ and non-saturable losses of 16 % was used to mode-lock the laser. Two aspheric lenses were used to focus onto the SESAM and the fiber end was cleaved at an angle of 8° in order to avoid back reflections. A 300 mW fiber pigtailed 976 nm laser diode was used to pump the oscillator. A fiber pigtailed 976 nm isolator was used to protect the pump diode.

To obtain the broadest possible spectra a net GVD close to zero is needed. However, a relative large net GVD, $\sum_k 2\beta_2^k L_k \sim 0.004 \text{ ps}^2$, was chosen in order to reduce the significance of the large total TOD, $\sum_k 2\beta_3^k L_k \sim 0.0013 \text{ ps}^3$. As a result of the large net GVD, the output pulses from the oscillator were prestretched with a positive chirp. Cavities with a smaller net GVD were also investigated but did not result in broader spectra. That the obtainable spectral width is limited by the high intra cavity total TOD is further investigated by numerical simulations below.

The amplifier consisted of an isolator, a WDM, 22.5 cm highly doped ytter-

bium fiber (1200 dB/m absorption at 976 nm) and a FC-APC fiber connector. A 600 mW single mode fiber pigtailed 974 nm diode laser was used to pump the amplifier. The amplifier was spliced directly onto the oscillator and again all non-PM sections were kept straight in order to avoid polarization evolution. The total fiber length after the coupler was 2.5 m and the length of standard fiber after the ytterbium fiber in the amplifier was 14.5 cm. The compressor consisted of 2.63 m HC-PBG fiber. The transmission was measured to be 82.2% and the low coupling loss was obtained with two aspheric lenses. Using a HC-PBG fiber for external pulse compression has the advantage of a high transmission and a fiber coupled output. With an additional isolator inserted after the amplifier, the HC-PBG fiber can also be spliced to the standard fiber with low loss. However, the available fiber pigtailed isolators have a rather high loss of -3.6 dB (56 %) at 1030 nm. Without this isolator an angle cleave of the standard fiber is needed to suppress back reflections into the amplifier.

5.4 Experimental results

The repetition rate of the oscillator was 55.3 MHz and stable CW mode-locking was obtained at a pump power of 145 mW. The pulse stability was measured with an RF-spectrum analyzer and the fundamental peak was 72 dB above the background. This corresponds to a relative amplitude fluctuation of less than 10^{-3} [64]. The general stability of the laser compares to that of other non-PM fiber lasers. The laser was not environmentally stable and the output could be affected by moving the fibers. However, stable operation was obtained if the fibers were left untouched.

Figure 5.4 (left) shows the output spectrum of the oscillator. The spectrum resembles that of a stretched pulse mode-locked laser in the positive net GVD regime, but with an asymmetric spectral modulation. As shown in section 5.5 the spectral asymmetry is the result of the high intra cavity TOD. The central wavelength of the laser was 1030 nm and the spectral 10 dB width was 17.1 nm. The output pulse energy from the oscillator was 40 pJ and the pulses were compressible to 182 fs with a bulk grating compressor. This is 15 % above the transform limit. The residual incompressible chirp is ascribed to be a result of the high TOD of the SC-PBG fiber. This was also the conclusion in reference [88] where 160 fs pulses (40 % above the transform limit) were obtained, with the use of HC-PBG fiber for intra cavity dispersion compensation.

The output from the oscillator was amplified and compressed in the external amplifier and HC-PBG fiber compressor. Figure 5.4 (left) shows the output spectrum after the amplifier and compressor. The 10 dB width increased to 17.4 nm at maximum amplification. Figure 5.5 (left) shows the output power after the compressor vs. pump power of the amplifier. At the highest pump power, the output pulse energy was 5.3 nJ. Before launching the amplified pulses into the HC-PBG fiber, an external grating compressor was initially used to compress the pulses. When increasing the amplifier pump power, a dependence was

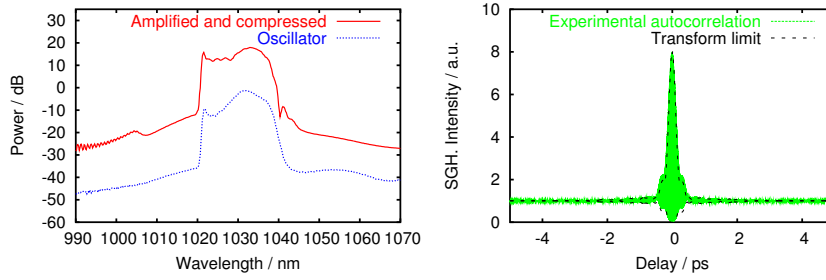


Figure 5.4: Left: Output spectrum from the oscillator and output spectrum after the amplifier and compressor at maximum amplification. Right: Experimental autocorrelation trace at maximum amplification. The autocorrelation trace is compared to the autocorrelation trace of the transform limited pulse, and the deconvoluted pulse duration is 158 fs (FWHM).

observed on the compressed pulse duration. At higher pump powers shorter pulses could be obtained and slightly less dispersion was needed in the grating compressor to find the minimum pulse duration. Due to this pump power dependence, the length of the HC-PBG fiber was optimized to give the shortest possible pulses at maximum amplification. The optimal length was found with a cut-back experiment (see figure 5.5 (right)) and the shortest possible pulses were obtained with 2.63 m of HC-PBG fiber.

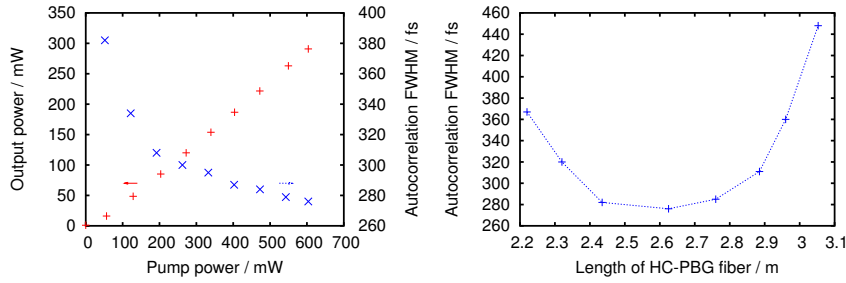


Figure 5.5: Left: Output power and output autocorrelation FWHM (of the top envelope) after the HC-PBG fiber as a function of pump power. Right: Cut-back of HC-PBG fiber at the highest pump power.

Figure 5.4 (right) shows the autocorrelation trace at maximum amplification. The autocorrelation trace is almost identical to the autocorrelation trace calculated from the transform limited pulse, which was obtained by numerically Fourier transforming the measured spectrum with zero phase. To deconvolute the experimental autocorrelation trace, the trace is compared to the calculated

autocorrelation trace. The calculated transform limited pulse has a pulse duration of 158 fs and hence the experimental autocorrelation trace is deconvoluted to this pulse duration.

In the laser system, transform limited pulse durations were only obtained at the highest pump power in the amplifier. To illustrate the pump power dependence of the compressed pulse duration, the autocorrelation FWHM (of the top envelope) vs. pump power after the HC-PBG fiber can be seen in Fig. 5.5 (left). As there is a power dependence on the pulse duration, it must be a result of nonlinear pulse propagation in the amplifier. This therefore suggests that the decreasing pulse duration is due to the combined effect of self-phase modulation and the third order chirp of the pulse as it enters the amplifier. The chirped pulse duration (before the HC-PBG fiber) was calculated to 1.6 ps (FWHM) by numerically adding the dispersion of the HC-PBG fiber to the transform limited pulse. From this value the total nonlinear phase shift in the amplifier can be estimated to $\sim \pi$. The third order chirp of the pulse is a consequence of the large uncompensated TOD of the cavity. Pulses prechirped with a large third order chirp have previously been demonstrated to have an optimal pulse duration at a certain amount of SPM [92]. Hence SPM can also be used to compensate for third order chirp in a pulse.

5.5 Numerical simulations

To further investigate the limiting role of TOD on the spectral width and consequently on the obtainable pulse duration, a numerical simulation of the laser oscillator was performed.

The laser was divided into five fiber sections and the nonlinear Schrödinger equation (NLSE) for a single polarization state was solved for the separate sections in succession. Effects of the SESAM, the coupler and coupling losses between different elements were also included in between the relevant fiber sections. Numerical parameters in each section were chosen to match the physically measured or specified parameters of the fibers.

The five fiber sections were: 36 cm SC-PBG fiber, 39 cm non-PM passive fiber, 8.5 cm yb fiber, 33 cm and 62 cm PM passive fiber, in agreement with the

Fiber type:	SC-PBG	non-PM	yb-doped	PM 1	PM 2
Length / cm:	36	39	8.5	33	62
β_2 / ps ² /m:	-0.085	0.023	0.023	0.023	0.023
β_3 / ps ³ /m:	$1.73 \cdot 10^{-5}$	$3.9 \cdot 10^{-5}$	$3.9 \cdot 10^{-5}$	$3.9 \cdot 10^{-5}$	$3.9 \cdot 10^{-5}$
β_4 / ps ⁴ /m:	$-1.92 \cdot 10^{-5}$	-	-	-	-
β_5 / ps ⁵ /m:	$2.73 \cdot 10^{-7}$	-	-	-	-
γ / (m W) ⁻¹ :	$1.55 \cdot 10^{-3}$	$4.3 \cdot 10^{-3}$	$8.8 \cdot 10^{-3}$	$3.5 \cdot 10^{-3}$	$3.5 \cdot 10^{-3}$

Table 5.1: Coefficients used to model the five different fibers.

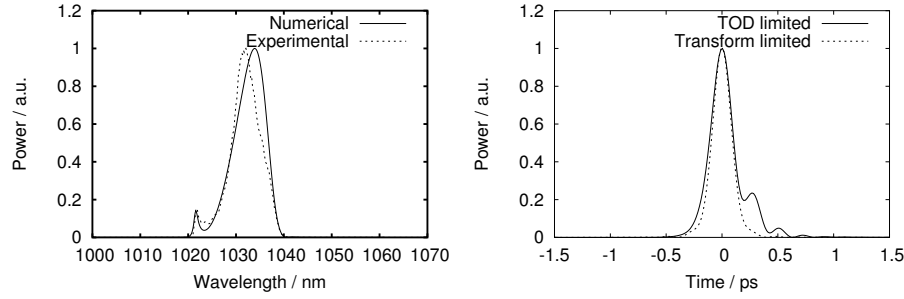


Figure 5.6: Left: Comparison between measured and calculated output spectra. Right: Simulated TOD limited pulse temporal pulse shape where only the quadratic chirp have been compensated and simulated transform limited temporal pulse shape where all the chirp have been removed.

real laser. The ytterbium fiber was modeled with a total unsaturated gain of 30 dB, corresponding to $g_0 = 81.3 \text{ m}^{-1}$, a saturation power of $P_{\text{sat}} = 0.8 \text{ mW}$, and a Gaussian gain bandwidth of 40 nm (FWHM). The saturation of the gain medium included the saturation from average powers coming from both directions. Other relevant coefficients used in the NLSE can be seen in table 5.1. The total insertion loss of the SC-PBG fiber including the loss on the butt-coupled mirror was 70 %. The SESAM was modeled with a modulation depth of 24 %, non-saturable losses of 16 %, a saturation energy of 80.5 pJ and a relaxation time of 500 fs.

From noise a pulse was iterated numerically until steady state was reached. In figure 5.6 (left) the experimental spectrum is compared to the numerically calculated spectrum on a linear scale. The spectral shape is slightly different, but the strong spectral modulation and the spectral width are in good agreement with the measured spectrum. To illustrate the residual third order chirp on the pulse, the output pulse was numerically compressed by adding only quadratic dispersion (β_2 term) to the pulse until a minimum was found. Figure 5.6 (right) shows the temporal shape of the pulse at this TOD limited minimum. The pulse clearly shows signs of a third order chirp, which can be seen from the oscillations on the right side of the pulse (compare e.g. to figure 3.6 in reference [1]). The pulse is compared to the transform limited pulse, calculated by removing all the chirp of the pulse. In addition to having broader shoulders to the right side as is typical if a positive third order chirp is added, the pulse also have a pulse duration (FWHM) which is 14 % longer than the transform limited pulse duration. This is also in agreement with the experimental result.

To further investigate the experimentally observed limit in obtainable spectral width and the role of the intra cavity uncompensated TOD, a series of simulations were performed where only the length of the SC-PBG fiber was changed, while all other parameters were kept the same. By increasing the length of the

SC-PBG fiber, the net normal GVD is decreased and if no TOD was present in the cavity, this would result in broader spectra. Figure 5.7 (left) shows the calculated output spectrum at three different lengths of SC-PBG fiber. The calculated spectrum labeled " $L_{\text{pbg}} = 36 \text{ cm}$ " is the same as in figure 5.6.

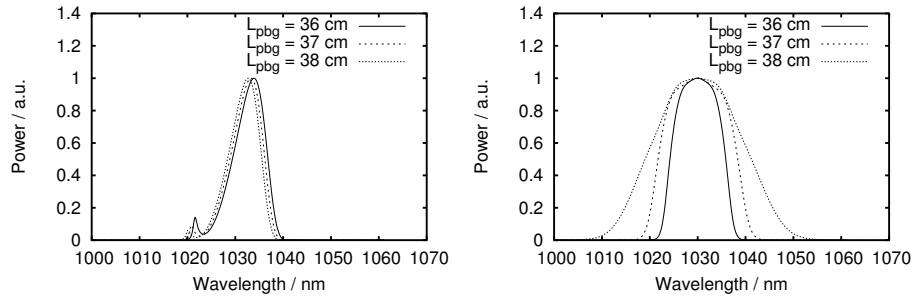


Figure 5.7: Left: Numerically calculated output spectra on a linear scale from lasers with three different lengths of SC-PBG fiber: 36 cm, 37 cm and 38 cm corresponding to a net GVD in the laser of 0.0042 ps^2 , 0.0025 ps^2 and 0.0008 ps^2 respectively. Right: Numerically calculated output spectra from the same three lasers except that β_3 and all higher order dispersion terms have been set to zero.

No significant increase in spectral width was observed even at a net GVD as small as 0.0008 ps^2 . Rather, the spectral shape and width were almost unchanged. To clarify that the spectral width is limited by the large intra cavity uncompensated TOD, calculations were also performed for the same three cavities, only with the TOD and all higher order dispersions artificially set to zero. Figure 5.7 (right) shows the calculated spectra. If no TOD and higher order dispersions are present in the cavity, much broader spectra are obtained. When comparing figure 5.7 (left) to figure 5.7 (right), it is clear that the obtainable pulse duration is limited by the large uncompensated TOD of the cavity, and that the experimentally obtained pulse duration cannot be significantly improved unless the TOD is reduced inside the cavity.

5.6 Outlook

Although femtosecond fiber lasers based on chirped fiber Bragg gratings are a more mature technology, the development of SC-PBG fiber lasers is of interest to NKT as these lasers are not limited by patents owned by other fiber laser manufactures. This demonstration of SC-PBG fiber as intra cavity dispersion compensation is a large step towards an environmentally stable femtosecond fiber laser with no sections of free space. The only problem which needs to be solved in order to obtain a cavity with no sections of free space optics is the removal of the two lenses in front of the SESAM. This is a problem which

has been solved by other fiber laser manufactures and is primarily a question of proper design of the SESAM. However, as only a very limited number of SESAMs were available during this study, this last step will be left to others.

A much more serious concern is the environmental stability of the laser. The environmental stability of the laser was limited by the use of non-PM fiber pigtailed components and primarily the non-PM SC-PBG fiber. The non-PM fiber pigtailed components are easily replaceable with PM pigtailed alternatives, and a birefringent version of the SC-PBG fibers is under development at Crystal Fibre. Hence a environmentally stable all-fiber laser based on SC-PBG fiber for dispersion compensation and with no sections of free space will be developed at NKT-Research in the near future based on this study.

If a pulse duration significantly shorter than the 158 fs as demonstrated here is required, either something has to be done to reduce the TOD of the SC-PBG fibers or elements with opposite sign of the TOD have to be included in the cavity. This is however also beyond the scope of this research. In reference [54] Ilday *et al.* demonstrates pulses with a duration as short as 36 fs from an ytterbium doped fiber laser, utilizing a bulk grating compressor for intra cavity dispersion compensation. However, with fiber based components for dispersion compensation, such as e.g. chirped fiber Bragg gratings, only pulse durations in the order of ~ 100 fs have been obtained from ytterbium based fiber lasers.

5.7 Summary

The use of SC-PBG fiber for intra cavity dispersion compensation in a mode-locked fiber laser has been investigated. SC-PBG fiber possess a large TOD, and this was both experientially and numerically verified to be the limiting factor on the obtainable pulse duration from fiber lasers utilizing SC-PBG fibers. The primary limitation was on the obtainable spectral width from the oscillator. Furthermore, a residual third order chirp resulted in output pulses with minimum pulse durations 15 % above the transform limit. This third order chirp was, however, demonstrated to be removable through nonlinear pulse propagation in an amplifier. As a result pulse durations down to 158 fs were demonstrated, and this is significantly shorter than what can be obtained without intra cavity dispersion compensation.

CHAPTER 6

Self-similar all-polarization maintaining environmentally stable fiber laser

This chapter presents an environmentally stable self-starting fiber laser based on a SESAM and polarization maintaining (PM) fiber pigtailed components. The laser was designed to operate in the self-similar regime and the laser generates parabolic-like pulses. Pulse energies of 1 nJ at a repetition rate of 17 MHz and a central wavelength of 1035 nm were obtained, and the pulses were externally compressible to a duration of 210 fs. Parabolic pulses are interesting for direct amplification, and chapter 7 presents an amplifier based on amplification of these pulses to the micro-Joule level. The experimental work of this chapter and chapter 7 were done in Jena.

6.1 Introduction

Propagation of short optical pulses with high peak powers inside optical fibers can cause high pulse distortions and pulse break-up due to high nonlinearities inside the fiber. Nonlinearities are important inside mode-locked fiber lasers due to the fact that the highest allowable total nonlinear phaseshift is usually of the order of π . If this intensity dependent phase shift is too high during one round trip, the pulse cannot reproduce itself within a constant phase shift, and hence the laser output fluctuates from pulse to pulse. As illustrated in chapter 3, the laser then enters the noise-like mode-locked regime if nothing is done to prevent it. A special kind of pulse does however tolerate a larger nonlinear phase shift: pulses with a parabolic temporal profile:

$$\begin{aligned} a(t) &= a_0 \left(1 - \left(\frac{t}{t_0} \right)^2 \right)^{1/2} & |t| \leq t_0 \\ a(t) &= 0 & |t| > t_0. \end{aligned} \quad (6.1)$$

The nonlinear phase shift, $\phi_{NL}(t) = \gamma L |a(t)|^2$, accumulated by a parabolic pulse, is also parabolic and hence adds to the chirp with a linear contribution:

$$c(t) = -\frac{\partial \phi_{NL}}{\partial t} = \frac{2a_0}{t_0^2} t. \quad (6.2)$$

Linear chirps are compressible by other linear dispersive elements inside an oscillator and if the pulse inside the cavity is parabolic, the laser output is no longer limited by the nonlinear phase shift. Figure 6.1 (left) shows both a chirped parabolic and a chirped Gaussian pulse and the contributions to their chirps from a nonlinear phase shift of 2π (at the peak of the pulses). As can be seen in the figure, the contribution to the chirp from the nonlinear phase shift to the parabolic pulse is linear over the extent of pulse, whereas the chirp of the Gaussian pulse is only approximately linear over the central part of the pulse and deviates in the wings.

The nonlinear phase shift is also important in amplifiers, if the pulses are to be compressible afterwards. It was shown in reference [32] and [23] that parabolic pulses with a linear chirp can be generated in high gain amplifiers. Such pulses can propagate self-similarly - that is in a form preserving manner - inside fibers with normal dispersion and high gain, even if the total nonlinear phaseshift exceeds π . As the pulse propagates, the temporal and spectral width increases exponentially, while maintaining a linear chirp that can be removed afterwards. The theory of parabolic pulse propagation in amplifiers will be further deepened in chapter 7. In an oscillator, the limit on the nonlinear phase shift can also be increased by designing the oscillator to develop parabolic pulses and using the self-similar nature of parabolic pulse propagation. The first self-similar oscillator was demonstrated by Ilday *et al.* [24]. Today the largest pulse energies from fiber oscillators are obtained from self-similar oscillators [57]. A

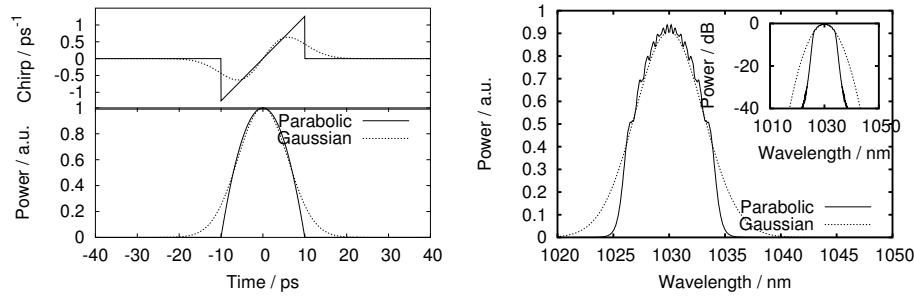


Figure 6.1: Left: Temporal profile of a linear chirped parabolic and a linear chirped Gaussian pulse. The contributions to their chirps from a nonlinear phase shift of 2π (at the peak of the pulses) is also shown. Right: spectra of the two chirped pulses on a linear scale. Insert spectra on a logarithmic scale.

wide range of different pulse shapes were shown to evolve asymptotically toward the parabolic shape in reference [32] and [93], but dependent on the initial pulse shape, longer or shorter lengths of fiber were needed for the pulse to converge. Self-similar oscillators generating linearly chirped parabolic pulses are an interesting source for self-similar amplifiers, as the seed pulse from such an oscillator does not need a long section of fiber with gain to evolve into the parabolic pulse, and hence, self-similar amplifiers based on shorter fibers can be obtained. Furthermore, it can be shown that parabolic pulses with high peak powers can propagate in both a form preserving and wave-breaking-free manner in normal dispersive fibers both without [94] and with gain [95] - even if the pulses have not reached the asymptotic regime.

Parabolic pulses are most easily identified by the spectrum, which is also approximately parabolic. Figure 6.1 (right) compares the spectrum of a chirped parabolic pulse to a chirped Gaussian pulse on a linear scale (Insert: logarithmic scale). The oscillations in the spectrum originates from the non-differential points at $t = \pm t_0$ of the analytical expression of the parabolic pulse. Self-similar oscillators are however not likely to be able to produce exact parabolic pulse, because of these non-differential points, but as shown in chapter 7, these pulses allow amplification beyond the nonlinear limit in an fiber amplifier.

The pulse evolution in a self-similar oscillator differs from the pulse evolution in the well known soliton [96] and stretched pulse lasers [55]. In soliton lasers the generated pulse maintains an almost constant temporal width during one round trip: the soliton. A stretched pulse laser consists of two sections of fiber with normal and anomalous dispersion causing the chirp to change from positive to negative and back to positive during one round trip [11]. In the self-similar laser, the chirp increases monotonically as the pulse propagates inside the fiber, and the pulse is only compressed at points where nonlinearities are negligible. An even more important issue for a self-similar laser is that the

pulse must experience a large gain per round trip in order to take advantage of the spectral bandwidth of the gain medium, to shape the pulse. The net cavity dispersion should also be positive so that the pulse is always positively chirped.

The energy achievable in soliton fiber laser systems is limited to some ten picojoules [97]. On the other hand, stretched pulse lasers with output energies from tens of picojoules to some nanojoules have been reported [56, 98–100]. Self-similar pulse evolution inside mode-locked fiber lasers has recently been shown to extend the obtainable pulse energy beyond the limit found in stretched-pulse lasers [57]. Therefore, the self-similar pulse regime is an interesting regime to investigate. Previous to the publication of our paper [V], self-similar pulses had only been generated from fiber lasers based on the nonlinear polarization evolution in the ring geometry [24]. This method does not allow for the use of PM fibers because of the walk-off between light polarized along the two axis of the fiber. Hence, environmentally stable lasers cannot be obtained with this geometry as nonlinear polarization evolution in non-PM fibers is sensitive to environmentally induced changes in the birefringence of the fiber. Environmentally stable fiber lasers have, however, been reported in a variety of other configurations, based on both nonlinear polarization evolution [58, 101] and saturable absorber mirrors [84]. However, as environmental instabilities in fiber lasers mainly arise from environmentally induced changes in the birefringence of non-PM fibers, the most natural approach is to use PM fibers with the light polarized only along the slow axis. This of course eliminates the possibility of using nonlinear polarization evolution. In this chapter the generation of self-similar pulses from a linear cavity comprising only PM fibers is demonstrated.

6.2 Cavity design

Two different cavity configurations have been investigated and self-starting self-similar pulses could be generated over a wide range of parameters such as output coupling, pump power and net cavity dispersion. The two different cavity configurations can be seen in figure 6.2. In both cases the mode-locking mechanism is based on a semiconductor saturable absorber mirror (SESAM) and highly efficient transmission gratings have been used for intra cavity dispersion compensation. The fiber length inside the cavity was also chosen to be the same in the two cases and the only difference was the choice of output coupling. In one case (figure 6.2(a)), the output coupler was a fixed fiber pig-tailed coupler allowing for a fiber based output. The coupler was a thin-film 30:70 PM coupler (output coupling: 30 %) with transmission in only the slow axis. In the other case (figure 6.2(b)) the output coupler was based on a bulk polarizer and a quarter-wave plate allowing a tunable output coupling. Both cases are presented here, as highest output powers were obtained from laser (b), but laser (a) had the advantage of an fiber coupled output and was used for the setup in chapter 7.

The gain medium was a 31 cm long highly ytterbium doped (~ 300 dB/m

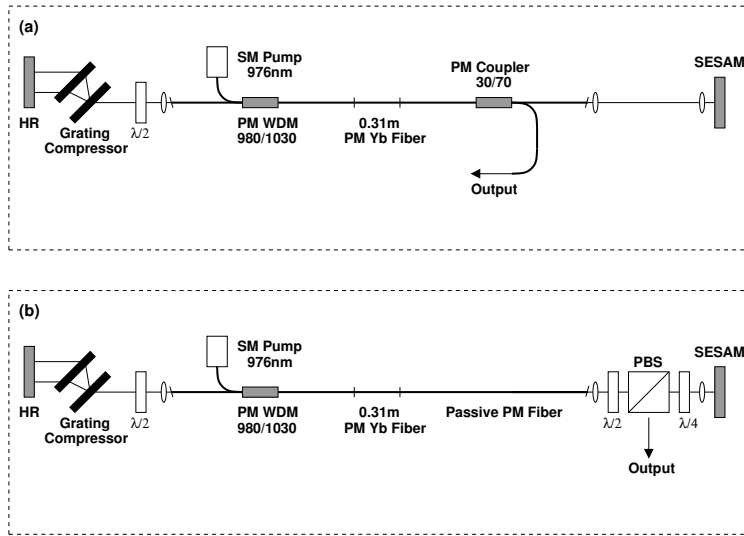


Figure 6.2: The two different cavity designs: (a) with fiber output coupler and (b) with variable bulk output coupler. PM - polarization maintaining, HR - high reflection mirror, SESAM - saturable absorber mirror, PBS - polarization beam splitter.

absorption at 976 nm) PM fiber with a mode-field diameter of $4.8 \mu\text{m}$. The utilization of the minimal length of gain fiber allows to decouple gain bandwidth filtering from the nonlinear evolution in the undoped fiber because the effect of GVD and nonlinearity can be neglected during the amplification [24]. This fiber was pumped through a thin-film PM WDM by a single mode diode providing a maximum output power of 400 mW at a wavelength of 976 nm. The passive fibers used in the setup were Panda 980 PM fibers with mode field diameters of $\sim 7 \mu\text{m}$ at 1035 nm and a dispersion of $0.023 \text{ ps}^2/\text{m}$. The total fiber length inside the cavity was 5.6 m for both cavity designs and in both cases the length of the passive fiber on both sides of the gain medium was equal in order to create symmetric conditions for the pulse evolution after the gain medium in both directions. All the PM fibers were fusion spliced together with an estimated polarization extinction ratio above 37.5 dB and all fiber ends were either angle polished or angle cleaved.

The SESAM is commercially available [60] and is based on a non-resonant design, using a GaAs/AlAs Bragg mirror with 27 layer pairs and 26 low temperature molecular beam epitaxy grown InGaAs quantum wells in front of the mirror. The AR coated device has a low-intensity absorption of 45 %, a modulation depth of $\sim 30 \%$ and a saturation fluence of $\sim 100 \mu\text{J}/\text{cm}^2$. The recovery dynamics of the optical excitation has been measured in a pump-probe experiment using 200 fs pulses. The pump-probe experiment was carried out by D. Fischer

and G. Steinmeyer, MBI Berlin, Germany. The SESAM shows a bi-temporal impulse response with a short relaxation time of < 200 fs and a slower part of 500 fs. The ratio of the fast and slow parts has been determined to 3:2.

To saturate the SESAM sufficiently a telescope was used to image the output of the fiber onto the SESAM. To obtain self-similar pulse evolution in a SESAM based laser, it is important to be far beyond the saturation energy, so that temporal shaping in the SESAM can be neglected. In chapter 8 the opposite case is explored where a SESAM operated close to the saturation energy is the primary source of temporal shaping.

The transmission gratings used for intra cavity dispersion compensation were 1250 lines/mm gratings made of fused silica [102] with a high transmission into first order ($>95\%$ at 1035 nm). The gratings were set up in Lithrow angle (40°) with a grating separation of 16 mm. A half-wave plate was used between the gratings and the PM fiber to ensure excitation of only the slow axis. In laser (b) an additional half-wave plate was also used to ensure excitation of only the slow axis of the fiber after the polarizer. If the axis of the fiber itself is properly aligned to the grating or the polarizer, the half wave plate can be removed resulting in an even simpler setup. With the fiber pig-tailed coupler used in laser (a), a half-wave plate was no longer necessary, as the coupler in itself worked as a polarizer transmitting only light in the slow axis.

6.3 Experimental results

Special care had to be taken to align the half-wave plates to ensure excitation of only the slow axis with a high extinction ratio. It was difficult to align the wave-plates accurately in especially laser (b) as in this configuration there was no polarization dependent loss inside the fiber. With the fiber pig-tailed coupler/polarizer in laser (a) it was much easier, as only one wave-plate had to be aligned. If the wave-plates were not perfectly aligned (i.e. within one degree), smaller or larger ripples on top of the spectrum could be observed.

Self-similar spectra, characterized by a parabolic top and with steep edges [24], with a FWHM between 8 and 12 nm dependent on the pump power, could be obtained with a net cavity dispersion of ~ 0.02 ps² from both lasers. A typical output spectrum from laser (b) is shown in figure 6.3 (left), where the FWHM of the self-similar spectrum is 11.3 nm. As the pump power was increased the spectral width increased monotonically, until the threshold for double-pulsing was reached (i.e. two pulses per round trip). The relatively large value of the net cavity dispersion of (≥ 0.02 ps²) was chosen to obtain a symmetric spectrum.

In contrast, for lower but still positive values of net cavity dispersion, broader but asymmetric and more structured spectra could be observed, which correspond to the stretched-pulse regime [57]. In the following the focus will only be on the self-similar regime.

The highest output pulse energy was obtained from laser (b), where the output coupling could be tuned. For a high output coupling coefficient the highest

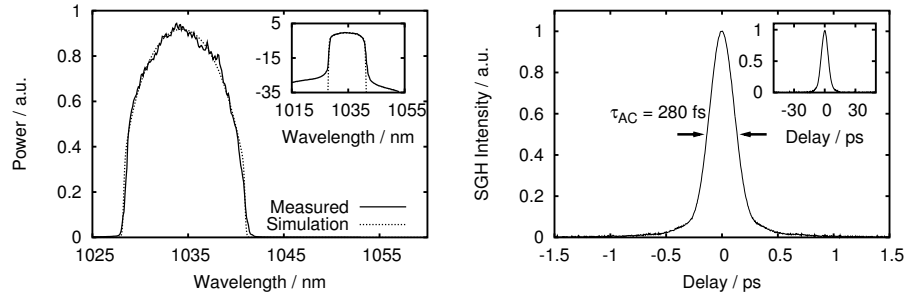


Figure 6.3: Left: Typical output spectrum on a linear scale of the laser (b) operated in the self-similar regime. Dotted curve: numerical simulation. Insert: logarithmic scale. Right: Autocorrelation trace of the externally compressed pulse from laser (b) at a pulse energy of 1 nJ with an autocorrelation FWHM of 280 fs. Inset: Uncompressed output pulse with an autocorrelation FWHM of 8.2 ps.

pulse energies of 1 nJ were obtained with a repetition rate of 17 MHz. The value of 1 nJ is smaller than what has been obtained recently with a self-similar ring laser [57]. However, in ring lasers more degrees of freedom are available to optimize the output pulse energy. The optimal pulse energy was further found in reference [57] to be highly sensitive to the cavity length. It is expected, that higher pulse energy can also be obtained if the cavity length of these lasers are optimized. The focus here is however not on high pulse energy directly out of the oscillator, but rather on a low repetition rate, enabling a higher final pulse energy after external amplification.

The chirped self-similar output pulse of laser (b) at a pulse energy of 1 nJ had a duration of 7.2 ps (8.2 ps FWHM on the background free autocorrelator) (see figure 6.3 (right)), but could externally be compressed to an autocorrelation FWHM of 280 fs on the background free autocorrelator. This corresponds to the transform limit. The pulse duration can be calculated from the width of the autocorrelation by assuming a transform limited self-similar spectrum of the compressed pulse (deconvolution factor 1.33) and is from this evaluated to 210 fs. The scan range of the background free autocorrelator was 150 ps, but to check for multiple pulsing and to ensure that there was only a single pulse in the output, a 25 GHz photo diode in combination with a 50 GHz sampling oscilloscope providing a scan range from 30 ps to 60 ns has been used.

Self-similar spectra similar to the spectrum shown in figure 6.3 were also obtained from laser (a). The output pulse energy was ~ 0.12 nJ, which could be externally re-compressed to an autocorrelation FWHM of 350 fs. Due to the fixed output coupling of 30%, which is lower than in the other setup, no flexibility was given to find the regime of higher pulse energy and shorter pulses. Additionally, an extra loss of 30% is introduced inside the cavity due to the fact that the coupler is passed in both directions.

To make sure that the lasers operates in the self similar regime some inspections have to be made. First of all, the spectrum should of course exhibit a self-similar shape, which is fulfilled in our case. Secondly, an important condition for self-similar evolution is that the pulse is always positively chirped inside the cavity and with a minimum pulse duration after the intra cavity gratings just before entering the fiber [57]. The negative dispersion given by the grating pair used for external compression ($\sim -0.36 \text{ ps}^2$ (double pass)) was higher than that of the pair used inside the cavity. In addition, only half the length of intra cavity fiber is passed before the pulse is coupled out. This indicates that the pulse is still highly positively chirped before entering the fiber after the intra cavity grating pair. As the dispersion from this point on inside the cavity is positive until the pulse again reaches the intra cavity gratings, this point must be a minimum point. As an additional verification, a numerical simulation of the cavity was carried out. Each segment was treated separately by solving the nonlinear Schrödinger equation with the parameters of our experimental setup. In figure 6.3 the simulated spectrum can be seen to be in good agreement with the measured spectrum. In the simulation the pulse exhibits self-similar pulse propagation [57] and is always positively chirped.

In both configurations the laser was self-starting and immediately jumped back into the same mode-locked state without any external perturbations if, for instance the laser was switched off and back on again. Furthermore, the use of PM fibers made the laser stable toward environmentally induced changes to the birefringence of the fiber. The fibers could be twisted and moved around while maintaining a stable mode-locked output. This was verified by observing a uniform train of pulses using a fast photo diode and an analog scope.

6.3.1 Bound states

As mentioned above, it is important to verify, that only a single pulse resides inside the cavity. This is especially true in long fiber lasers or at high intra cavity average powers, where the power can be distribute over two or more pulses. This occurs if two pulses result in a smaller loss, and hence a more attractive solution to the cavity, or if the nonlinear phaseshift is so high, that a single pulse breaks up [103, 104]. The resulting smaller pulse energy per pulse is usually an unwanted effect. In general, these pulses are randomly separated, but under certain conditions these pulses can be regularly spaced in the cavity. Two different scenarios can happen. If n pulses coexist in the cavity simultaneously, they can either be separated by T_R/n where T_R is the round trip time, and hence create a pulse train with a repetition rate n times larger than the fundamental. This is called harmonic mode-locking. Alternatively they can be spaced very closely together with a fixed separation which is much smaller than T_R . This is called bound-state mode-locking. The later case is the most difficult to detect at first sight, as the pulses can be difficult to resolve with ordinary oscilloscopes and photo diodes.

Laser (a) was limited to a lower pulse energy compared to laser (b) by the

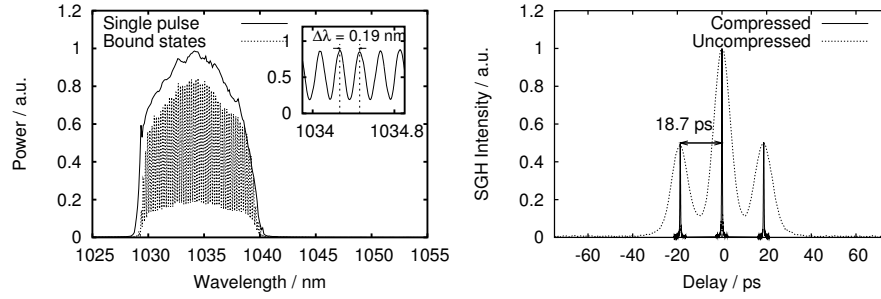


Figure 6.4: Left: Output spectrum from the laser in the single pulse and the bound states regimes. Insert: zoom on the spectral fringes. Right: Autocorrelation of the laser output in the bound state regime (before and after external compression).

onset of bound-state lasing. At a pump power of about 94 mW, stable self-starting single pulse mode-locking was observed. If the pump power was now increased, the laser switched into a new regime of operation, where two closely bound pulses circulated inside the cavity. At a typical pumping power of 125 mW the two bound states were self-starting - i.e. if the laser beam inside the cavity was blocked and afterwards unblocked, the laser jumped right back into the same mode-locking state. The transition was observable both spectrally and temporally. Figure 6.4 (left) shows the output spectrum of laser (a) in the bound state and in the single pulse regime. The spectral width decreased slightly in the bound state regime due to the lower pulse energy per pulse, and is strongly modulated, which is a direct consequence of the a precise phase relationship maintained between the two pulses. Note that the exact modulation depth cannot be found due to the limited resolution of the spectrum analyzer (0.05 nm), but is believed to be larger than the measured 80 %. The insert of figure 6.4 (left) shows a zoom in on the spectral fringes. The fringes correspond to a two-wave interference pattern with 0.19 nm period.

The autocorrelation traces of both the compressed and uncompressed two bound states can be seen in figure 6.4 (right). The temporal separation, d , of the two pulses was measured to 18.7 ps in correspondence with the spectral modulation period ($\Delta\lambda = \frac{\lambda^2}{c \cdot d}$), and the duration of the uncompressed pulses was 8.3 ps. After external compression a pulse duration of 248 fs (410 fs autocorrelation FWHM) was obtained. The slightly longer pulse duration is in correspondence with the slightly narrower spectrum. In the two bound state regime the pulse energy per pulse was 70 pJ. If the pump power was further increased, regimes of three and even four bound states were obtained.

6.4 Outlook

Besides the demonstration of a self-starting environmentally stable fiber laser constructed from PM fibers only, the truly interesting aspect about the presented laser is its output spectral shape and especially the amplification of this output beyond the nonlinear limit in a fiber amplifier. This will be the scope of the next chapter. As the central wavelength of the laser was 1034 nm, the laser is a suitable candidate for amplification in short large-mode-area ytterbium fiber amplifiers and the spectral width of the laser is also almost ideal, as broader spectra can experience significant spectral gain narrowing in the amplifier.

6.5 Summary

In summary, it has been experimentally demonstrated that a self-starting self-similar oscillator can be obtained with a linear cavity where a SESAM is used as the nonlinear mode-locking mechanism. Further, the oscillator was intrinsically environmentally stable, as only PM fibers were used. Pulses with an energy of 1 nJ at a repetition rate of 17 MHz were obtained, and the output pulse duration was 7.2 ps, but could be externally compressed to a pulse duration of 210 fs.

CHAPTER 7

Microjoule-level all polarization-maintaining femtosecond fiber source

Direct amplification of parabolic pulses from an environmental stable passively mode-locked fiber oscillator is presented here. The pulses are amplified in an Yb-doped single-polarization photonic crystal fiber and the special pulse shape allows for the generation of high quality femtosecond pulses beyond the non-linear limit. The system delivers 240 fs pulses with a pulse energy of 1.2 μJ (21 W average power) at a repetition rate of 17 MHz and central wavelength of 1035 nm in a linearly polarized beam with diffraction-limited quality.

7.1 Introduction

Due to the outstanding heat dissipation capabilities of a rare-earth-doped fibers, average power scaling of fiber amplifiers is a straightforward problem, which makes a fiber amplifier system interesting for e.g. fast material processing [13]. Furthermore, nonlinear effects during amplification can be greatly reduced by the application of Yb-doped low-nonlinearity photonic crystal fibers with extended single-mode cores compared to step index fibers [105] and absorption length of only some ten centimeters [106]. Especially, the possibility of making very short fiber amplifiers makes ytterbium a better choice over e.g. erbium. The problem with erbium is that the doping concentration in the fiber is limited by concentration quenching due to cluster formation [107]. Hence longer fibers are needed to obtain the same total gain, but longer fibers also result in a larger nonlinear phase shift accumulated by the pulse. In general, the nonlinearity of a fiber amplifier can be reduced by either decreasing its length or by increasing its core size. The core size in step index fibers is limited by higher order transverse modes. Step index fibers are only single mode (i.e. only supporting a single transverse mode) above a specific wavelength - the cut off wavelength. If the fiber is scaled in order to increase the core size, the cut off wavelength will also move towards higher wavelengths and eventually above the desired lasing wavelength. The result is an output which is no longer diffraction limited. Photonic crystal fibers (PCFs) can be designed to be endlessly single mode (i.e. supporting only a single mode at all wavelengths) by increasing the air fill fraction of the cladding, and hence increasing the index step between the core and the average index of the cladding [108]. Endlessly single mode fibers can in principle be scaled to have any core size. However, a further limit is set by the bend losses of the fiber. Like conventional fibers, PCFs exhibit a bend loss edge at long wavelengths. The reason for this is that the mode extends further into the cladding at longer wavelengths, resulting in a more weakly guided mode that will suffer a greater perturbation in response to bending. In addition to this PCFs also have a short wavelength bend loss edge due to the wavelength dependent effective index in the cladding [108]. As the fiber is scaled, the low bend loss edge also moves towards higher wavelengths. A solution to this problem was introduced in reference [106] where the fiber was simply drawn into a rod with almost zero flexibility. On the practical side, however, another problem arises with increasing core size. As the core size increases, it is increasingly difficult to polish the core to be entirely scratch free.

Compact and environmentally stable high energy and high average power ultra-short pulse laser sources have many applications. Examples are micro machining, marking, eye surgery (ophthalmology), index modification in transparent materials (waveguide writing) and frequency conversion. In terms of compactness, cost, reliability and ease of operation a fiber based laser system is the predestined laser architecture. Fiber based short-pulse oscillators have been demonstrated to be an ideal candidate for compact femtosecond laser sources [56].

However, the pulse energy from fiber lasers is fundamentally limited by the nonlinear phase shifts accumulated during propagation through the fibers inside the cavity [57]. Hence, to reach pulse energies sufficient for most applications, the laser has to be amplified.

The pulse energy is also limited in amplifiers by the nonlinearities. Depending on the pulse shape, a large nonlinear phase shift can result in a pulse which cannot be compressed to the transform limit with linear dispersive elements like gratings and hence the pulse quality degrades. Nonlinear effects also introduce other pulse quality degrading problems, like wave-breaking where the pulse breaks up into several pulses [94]. Wave-breaking is a consequence of different frequency components of chirped pulses, catching up with other frequency components due to different group velocities and happens to pulses with non-monotonically varying chirps [94]. Further problems arise through the generation of stimulated Raman scattering [109], which decreases and limits the obtainable pulse energy and also increases the noise on the pulse. As mentioned in chapter 6 the final amplified pulse quality can be highly increased, if the input pulse has a parabolic shape. The reason for this is the shape of the nonlinear phase, which is also parabolic according to the intensity profile of the pulses [32]. In the high power limit (see equation 7.3 below), the pulse will remain a parabolic shape with linear chirp also after amplification [95].

So far amplified mode-locked fiber laser systems suffer from the lack of stability of non-polarization maintaining (non-PM) components. As demonstrated in chapter 6 environmentally stable fiber lasers can be constructed using polarization maintaining (PM) fibers. However, if a linearly polarized environmentally stable amplified output is desired, all stages including the amplifier should be PM. It was shown in reference [110] that a single polarization property could be added directly to low nonlinearity PCFs, which increases stability and further reduces the complexity of the setup by reducing polarization control [110].

In terms of average powers, impressive results from femtosecond fiber amplifier systems have already been obtained using non-polarization maintaining low-nonlinearity fibers in chirped pulse amplification systems [111] and in amplifiers, where a parabolic pulse is created during amplification and therefore additional pulse stretching is not necessary [112]. The nonlinearity in the amplification stage can of course be greatly reduced by incorporating temporal pre-stretching of the pulse using e.g. bulk gratings before launching it into the amplifier. 1.8 μJ 220 fs pulses at 1040 nm with a repetition rate of 73 MHz were obtained in reference [111] by applying this approach, and 100 μJ at a repetition rate of 200 kHz was obtained in reference [14], but the bulk grating separation of 1 m in these systems, doesn't exactly make them compact. More compact prestretching schemes have also been demonstrated. 6.5 μJ 940 fs pulses were obtained at 1558 nm in reference [113] after prestretching the pulses to 720 ps with the use of a chirped fiber Bragg grating, subsequent amplification in a large-mode area Er/Yb-doped fiber and recompression with an bulk grating compressor. Direct amplification without prestretching is, however, preferable as it simplifies the setup, and large grating separations can be avoided.

Especially, the amplification of parabolic pulses allows for the realization of high peak powers without any significant degradation of the recompressed pulse quality. If the pulse entering the amplifier is already parabolic, it is not necessary to take special care of the parabolic pulse evolution in the following amplifier stages in comparison to references [32, 112]. Consequently, the combination of an oscillator delivering parabolic pulses and a polarization-maintaining low-nonlinearity fiber seems to provide an easy way for high-energy linearly polarized femtosecond pulse generation. In this chapter the theory behind parabolic amplifiers and amplification of parabolic pulses will be introduced, followed by the first demonstration of direct amplification of parabolic pulses from a self-similar oscillator [VI]. The setup was further the first demonstration of amplification of an environmentally stable femtosecond fiber laser in an PM and single polarization amplifier to the microjoule level without significant pulse quality degradation.

7.2 Theory

To understand the difference between direct amplification of parabolic pulses and self-similar amplifiers, the theory of self-similar amplifiers is first introduced. Fermann *et al.* [32] were the first to introduce the concept of self-similar pulse evolution in fiber amplifiers. A solution $u = u(x, t)$ of a nonlinear partial differential equation is called self-similar if the knowledge of u at time t_0 is sufficient to obtain u for all $t > t_0$ by a suitable rescaling.

Fermann showed that parabolic pulses are exact asymptotic solutions to the nonlinear Schrödinger equation (NLSE):

$$\frac{\partial a}{\partial z} = -i\frac{1}{2}\beta_2\frac{\partial^2 a}{\partial t^2} + i\gamma|a|^2a + \frac{g}{2}a, \quad (7.1)$$

with constant gain, g (both spectrally and longitudinal). The analytical theory was extended to include longitudinal gain variations, $g(z)$, in reference [114] and further to include variations in $\beta_2(z)$ and $\gamma(z)$ in reference [115]. However, the inclusion of non-constant g , β_2 and γ increases the complexity of the analysis and the essential physics can be understood from the simpler case. The only conditions that have to be fulfilled for self-similar pulse propagation are $\beta_2\gamma > 0$ and $g > 0$, which restrict the theory to normally dispersive fiber amplifiers, such as e.g. Yb-doped fiber amplifiers.

Independently of the initial pulse shape, any pulse will evolve asymptotically into a similariton - i.e. a pulse with a parabolic intensity profile and a linear positive chirp:

$$\begin{aligned} a(z, t) &= a_0(z) \left(1 - \left(\frac{t}{t_0(z)}\right)^2\right)^{1/2} \exp(i\phi(z, t)) & |t| \leq t_0(z) \\ a(z, t) &= 0 & |t| > t_0(z), \end{aligned} \quad (7.2)$$

where

$$a_0(z) = \frac{1}{2}(gE_{IN})^{\frac{1}{3}}\left(\frac{2}{\gamma\beta_2}\right)^{\frac{1}{6}}\exp\left(\frac{gz}{3}\right),$$

is the amplitude of the parabolic pulse,

$$t_0(z) = 3g^{-\frac{2}{3}}\left(\frac{\gamma\beta_2 E_{IN}}{2}\right)^{\frac{1}{3}}\exp\left(\frac{gz}{3}\right),$$

is the $t_{FWHM}/\sqrt{2}$ width of the pulse, and

$$\phi(z, t) = \phi_0 + \frac{3\gamma}{2g}a_0(z) - \frac{g}{6\beta_2}t^2,$$

the phase of the pulse. E_{IN} is the input pulse energy, and the asymptotic solution only depends on this and on the amplifier parameters. The energy of the parabolic pulse is $E(z) = \frac{4}{3}a_0(z)^2t_0(z)$. The linear chirp of the pulse is given by:

$$\delta\omega(t) = -\frac{\partial\phi(z, t)}{\partial t} = \frac{g}{3\beta_2}t \equiv C \cdot t.$$

An approximate analytical solution of the pulse spectrum can also be calculated [114]:

$$\begin{aligned} |a(z, \omega)|^2 &\simeq \frac{3\gamma a_0^2}{g} \exp\left(\frac{2}{3}gz\right) \left(1 - \left(\frac{\omega}{\omega_0(z)}\right)^2\right) & |\omega| \leq \omega_0(z) \\ |a(z, \omega)|^2 &= 0 & |\omega| > \omega_0(z), \end{aligned}$$

with the $\omega_{FWHM}/\sqrt{2}$ width given by $\omega_0(z) = C \cdot t_0(z) = \frac{g}{3\beta_2} \cdot t_0(z)$. The spectrum is also approximately parabolic [114] with a linear spectral chirp, and the approximation is good for large chirps, C , whereas the spectrum resembles that of a sinc function with many side-lobes if $C = 0$. Both the pulse energy, and the temporal and the spectral width of the pulse increase exponentially in the amplifier. The temporal and spectral intensity profile of a parabolic pulse can be seen in figure 7.1.

The generation of similaritons in optical fiber amplifiers have potential wide-ranging applications in many areas of current optical technology, as the output pulses have a well defined linear chirp even in the presence of input pulse distortions. Furthermore, all the energy of the input pulse is transferred into the parabolic pulse, as opposed to the generation of solitons, where the remaining energy above the soliton energy is shed off into a continuum. The intrinsic resistance to wave-breaking of parabolic pulses allows the scaling of the fiber amplifiers to higher-power regimes and the linear chirp facilitates efficient compression. The only issue of self-similar amplification is the propagation length over which a specific input pulse converges to the asymptotic solution.

To illustrate the asymptotic convergence towards a parabolic pulse, a calculation of an Yb-amplifier has been made by solving the NLSE numerically

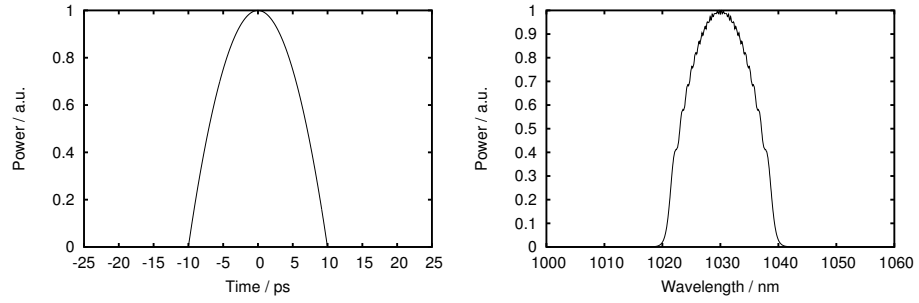


Figure 7.1: Left: Calculated temporal intensity profile of a parabolic pulse with $t_0 = 10$ ps and $C = 0.888$ ps⁻². Right: spectral profile of the same pulse with an approximate parabolic shape.

with realistic parameters. The length of the amplifier was chosen to 8 m with a constant gain, $g = 0.69$ m⁻¹, corresponding to a total gain of 30 dB. The non-linear coefficient was set to $\gamma = 3.5 \cdot 10^{-3}$ (m W)⁻¹, and the dispersion was set to $\beta_2 = 0.023$ ps²/m (corresponding to coefficients of a fiber with mode-field diameter (MFD) = 7 μ m). The input pulse energy was 100 pJ, corresponding to an output pulse energy of 100 nJ. Three different unchirped Gaussian pulses with durations: 100 fs, 500 fs and 5 ps were used as input. In figure 7.2 the RMS temporal duration of the pulses vs. propagation distance in the amplifier is compared to the asymptotic limit.

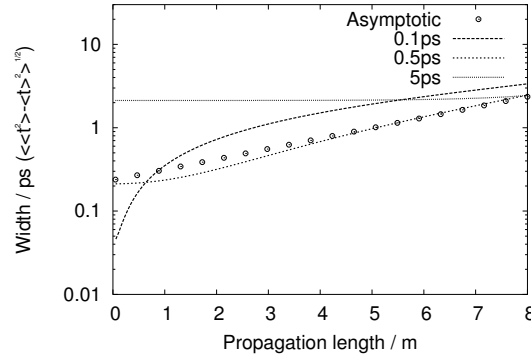


Figure 7.2: Calculated RMS temporal duration vs. propagation vs. distance in the amplifier for three different unchirped Gaussian input pulses: 100 fs, 500 fs and 5 ps.

The temporal duration of the pulses always converges towards the asymptotic solution. However the distance over which the pulses reach the asymptotic solution.

otic solution is very dependent on the input pulse duration. This is even more clearly seen if the output temporal and spectral intensity profiles are compared to the asymptotic solution (see figure 7.3).

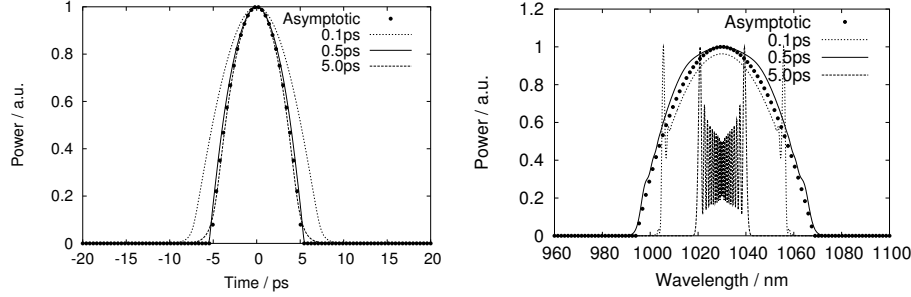


Figure 7.3: Left: temporal output intensity profile for three different input pulses, compared to the asymptotic solution. Right: spectral output intensity profile compared to the asymptotic solution.

From the output spectrum (figure 7.3 (right)) it is clear that both the 100 fs and 5 ps pulses have not yet entered the parabolic regime. For a given amplifier and input pulse energy, an optimal input pulse duration for fast convergence can be found by evaluating the similariton parameters at $z = 0$. With the amplifier parameters used in the calculation and the input pulse energy, the optimal input duration is:

$$t_0(0) = 3g^{-\frac{2}{3}} \left(\frac{\gamma\beta_2 E_{IN}}{2} \right)^{\frac{1}{3}} = 526 \text{ fs},$$

In agreement with the optimal input duration the pulse with the duration of 500 fs was the only one to come close the asymptotic solution. Another important property was also observed from the calculations: the higher total gain in the amplifier, the easier it is to reach the parabolic regime. However in practice high gains are limited in an amplifier by amplified spontaneous emission (ASE).

As the theory of self-similar pulse amplifiers is based on a simplified NLSE where e.g. spectral dependence on the gain and other nonlinear effects such as stimulated Raman scattering (SRS) have been neglected, the theory breaks down when these effects become important. The limit set by these effects on the obtainable pulse energy from self-similar amplifiers was calculated in reference [109]. If the gain per meter is high then shorter fiber lengths are necessary. However, for shorter fiber lengths the dispersion becomes less dominant and the spectral width of the asymptotic solution broadens. Hence, the limit in high gain amplifiers was found to be set by the finite bandwidth of the gain medium. On the other hand, in longer amplifiers with lower gain per meter the limit set by the generation of SRS is reached earlier. An optimal gain value can be found

in between these two limits, depending on the input pulse energy. For an Yb-doped amplifier with a gain bandwidth of 10.8 THz (38.2 nm) and a dispersion of $\beta_2 = 0.020 \text{ ps}^2$ and with an input pulse energy of 1 nJ, the optimal gain resulting in maximum output pulse energy was calculated to 3.9 dB/m [109]. The maximum output pulse energy does, however, still scale linearly with the mode field area (MFA) of the fiber. For a fiber with MFA of $700 \text{ } \mu\text{m}^2$ (equal to the MFA of the fiber used in the experiments below), the maximum output pulse energy was calculated to $< 0.5 \text{ } \mu\text{J}$. Hence, if larger pulse energies from an amplifier fiber with given dimensions are to be obtained alternative methods have to be considered, and one alternative is the direct amplification of parabolic pulses.

The theory of parabolic pulses was first introduced in 1993 by Anderson *et al.* [94], where they showed that parabolic pulses are a form invariant solution to the NLSE with zero gain, $g = 0$, and in the high power limit:

$$\frac{\beta_2}{2|a|} \left| \frac{\partial^2 |a|}{\partial t^2} \right| < \gamma |a|^2. \quad (7.3)$$

Other well known examples of form invariant pulse are the soliton in the anomalous dispersion regime, $\beta_2 < 0$, and Gaussian pulses in the dispersive only regime, $\gamma = 0$. The theory of parabolic pulses was extended in reference [95] to include a NLSE with nonzero gain. Under the assumption of equation 7.3, three differential equations for the parameters of the parabolic pulse (equation 7.2) can be derived:

$$\frac{\partial^2 t_0}{\partial z^2} = \frac{3}{2} \frac{E_{IN} \gamma \beta_2}{t_0^2(z)} \exp(gz) \quad (7.4)$$

$$C(z) = \frac{1}{\beta_2} \frac{1}{t_0(z)} \frac{\partial t_0}{\partial z} \quad (7.5)$$

$$|a_0(z)|^2 = \frac{3}{4} \frac{E_{IN}}{t_0(z)} \exp(gz) \quad (7.6)$$

From the first differential equation $t_0(z)$ can be numerically calculated from the initial conditions $t_0(0)$ and $(\partial t_0 / \partial z)_{z=0} = \beta_2 C(0) t_0(0)$, and from $t_0(z)$ the parameters, $C(z)$ and $|a_0(z)|^2$ can be calculated.

While the output pulses are still parabolic pulses, the output pulse differs from the self-similar solution, as it now also depends on the input pulse parameters, $t_0(0)$ and $C(0)$. The property that any pulse (i.e. also a parabolic pulse) will eventually evolve into the asymptotic solution if the amplifier is long enough is still fulfilled, even though it is less apparent. To illustrate this, equations 7.4-7.6 were solved with the same amplifier parameters as in the previous example (figure 7.2). This time three different parabolic input pulses were chosen. The input pulse energy was set to 1 nJ for all pulses and the spectral width was fixed to $\lambda_0(0) = \frac{2\pi c}{\lambda^2} \omega_0 = 5 \text{ nm}$, as in figure 7.1 (right). Only the pulse duration, $t_0(0)$, was varied: 1 ps, 5 ps and 10 ps. The evolution of the parameters, $t_0(z)$ and $\lambda_0(z)$ vs. amplification distance for the three pulse are compared to

the asymptotic solution in figure 7.4. To illustrate the convergence towards the asymptotic solution for the chosen pulses, the amplifier length was extended to 16 m, corresponding to a total (unrealistic) gain of 60 dB. After a sufficiently long amplification distance, all input pulses converge towards the asymptotic solution.

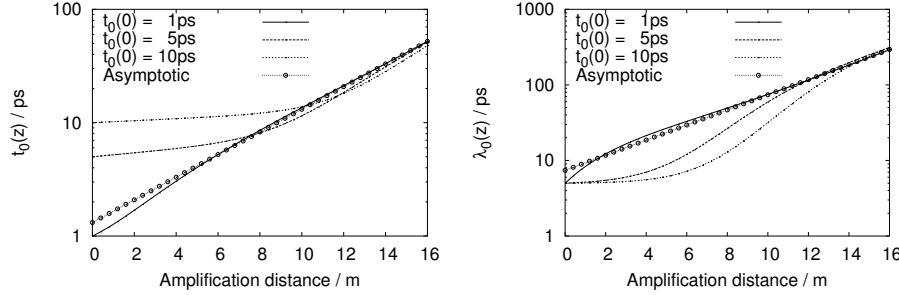


Figure 7.4: Evolution of the the parabolic pulse parameters vs. amplification distance. The parameters of the three parabolic input pulses are compared to the asymptotic solution. Left: $t_0(z)$ Right: $\lambda_0(z)$

Although the asymptotic limit is eventually reached, and although it can be reached faster with other choices of input pulses, the interesting regime is the regime before this happens. A very interesting property of the amplification of parabolic pulses is that, as the input pulse does not need to evolve into the asymptotic solution, shorter amplifiers with higher gain per meter can be used, and the limit set by SRS can be avoided. The limit set by the finite bandwidth of the gain medium does however still apply, but now the spectral width of the output pulse can be controlled by the input parameters (as illustrated in figure 7.4 (right)), and hence higher pulse energies could be obtainable from the amplification of parabolic pulses than from self-similar amplifiers. To investigate this further, a more conservative estimate of the limit set by the finite bandwidth can be found by neglecting the dispersion totally in equation 7.1 ($\beta_2 = 0$). Then the equation can be integrated directly under the assumption of an initial parabolic input pulse to yield a parabolic pulse with parameters:

$$\begin{aligned}
 t_0(z) &= t_0(0) \\
 P_p(z) &= P_p(0) \exp(gz) \\
 C(z) &= C(0) + 2\gamma \frac{P_p(0) \exp(gz) - 1}{t_0^2(0) g} \\
 &= \frac{\omega_0(0)}{t_0(0)} + \frac{3}{2} \gamma \frac{E_{IN} \exp(gz) - 1}{t_0^3(0) g}
 \end{aligned}$$

As the spectral width is still given by $\omega_0(z) = C(z) \cdot t_0(z)$, the output spectral width can be decreased for a fixed input pulse energy, E_{IN} , and fixed input

spectral width $\omega_0(0)$ by increasing $t_0(0)$. The output spectral width can hence be controlled to less than the spectral width of the gain medium. If $t_0(0)$ is sufficiently large, the regime of chirped pulse amplification is of course reached, where the nonlinearities can be neglected. However, the focus is here on much smaller input pulse durations where the pulse still experiences a significant nonlinear phase shift in the amplifier.

To further illustrate the strengths of parabolic pulse amplification, the experimental results from the amplification of the oscillator presented in chapter 6 are now presented.

7.3 Experimental setup

The μ J-level all-polarization-maintaining (PM) femtosecond fiber laser source consists of the environmentally stable and self-starting ytterbium-doped fiber oscillator, a polarization-maintaining pre-amplifier, a single-polarization fiber power-amplifier and a transmission grating compressor. The experimental setup is shown in figure 7.5. For the amplifier system the oscillator with the fiber-pigtailed 30/70 coupler was used (figure 6.2). The pre-amplifier consisted of a WDM and a 0.55 m PM Yb-doped single-mode fiber with identical fiber characteristics as the fiber used in the oscillator. The pre-amplifier was spliced to the oscillator with an fiber-pigtailed isolator in between. Between the pre-amplifier and the power-amplifier a bulk isolator was used for isolation. After the power amplifier the output was directed towards the Grating compressor with a dichroic mirror reflecting at 1034 nm and transmitting at 976 nm. A bulk isolator was also used after the power amplifier. The power-amplifier was pumped with a multi-mode 976 nm pump. The pump was fiber pigtailed to a 400 μ m multi-mode fiber. The pre-amplifier was pumped with a 300 mW single mode fiber-pigtailed pump diode. Aspheric lenses were used to couple light into the power amplifier. The grating compressor consisted of a pair of transmission gratings with high transmission [102].

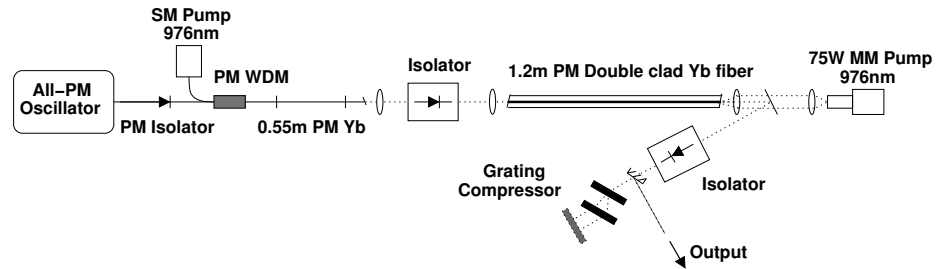


Figure 7.5: Schematic setup of the Microjoule-level all-polarization maintaining femtosecond fiber laser system (PM: polarization maintaining, SM: single mode, MM: multi mode, WDM: wavelength division multiplexer).

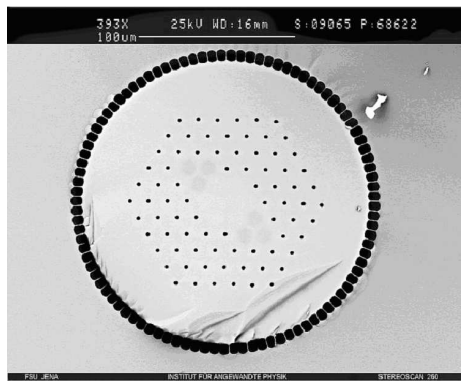


Figure 7.6: SEM image of the polarizing low-nonlinearity Yb-doped PCF.

The power amplifier consists of an 1.2 m long ytterbium-doped single polarization single-mode double-clad PCF [110] shown in figure 7.6. This fiber comprises index-matched stress-applying elements (SAP) as part of the photonic cladding. The proximity of the SAP to the core ensures high differential stress, and thus high birefringence. Additionally due to the index matching of the SAP array to the air-hole cladding, the light is confined by both parts of the photonic cladding: the air holes and the index matched regular array of SAPs. Furthermore, the amount of birefringence is enough to split two polarization states of the weakly guided fundamental mode so that the effective index of one polarization is below the cladding index. This results in a single-polarization large-mode-area fiber in a certain wavelength range, which is determined by the design and lies within the amplification bandwidth of Ytterbium in the present case. The MFA of $700 \mu\text{m}^2$ is larger than that of any step-index single-mode fiber. The pump cladding is formed by an air-cladding outside the inner photonic cladding and has a diameter of $170 \mu\text{m}$ and a NA of 0.6. This structure has a pump light absorption of 14 dB/m.

The power amplifier fiber was angle polished at an angle of 4° in order to suppress lasing on the ends. The fiber was further mounted with a glass to glass indexed matched interface in order to avoid melting the fiber with non-guided pump light.

7.4 Experimental results

The parabolic output spectrum from the oscillator had a FWHM of 12.1 nm at a fixed maximum output energy of 0.12 nJ. The spectrum from the oscillator can be seen in figure 7.7 (left). The chirped parabolic output pulses had a pulse duration of 7.2 ps (FWHM), but could externally be compressed to a pulse duration of 260 fs. The output of the oscillator (about 2 mW average power) was amplified to 50 mW and due to the additional fiber length the pulses were stretched to

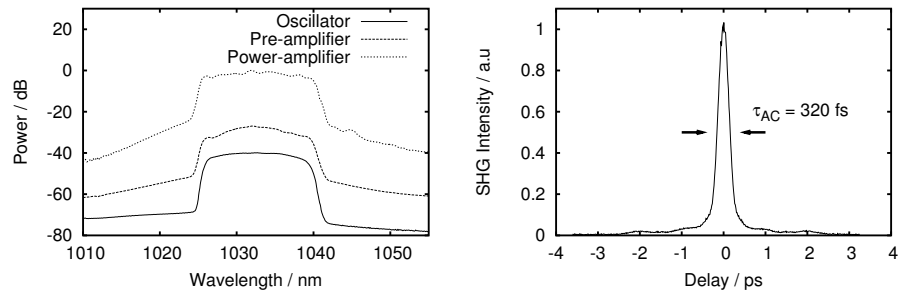


Figure 7.7: Left: Output spectrum from the oscillator, the pre-amplifier and the power-amplifier. Right: Autocorrelation after external compression at maximum amplification.

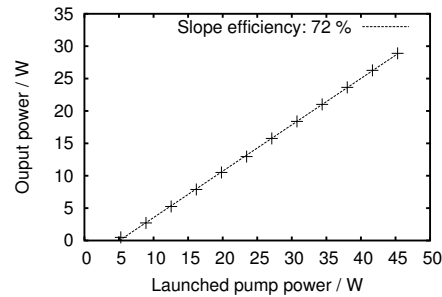


Figure 7.8: Output power of the power-amplifier vs. launched pump power.

10 ps (FWHM). After direct pre-amplification, these parabolic pulses were amplified in the single-polarization ytterbium-doped PCF to the μ J level without any further temporal stretching.

The output power characteristic is shown in figure 7.8. Up to 29 W average power with a slope efficiency of 72 % was obtained at a launched average seed power of ~ 30 mW. The polarization extinction ratio was as high as 24 dB (1:250) even at the highest power level. The output spectra of the pre- and main amplifier are also shown in figure 7.7 (left). The influence of self-phase modulation by the slight spectral broadening and modulation can be seen. However, the recompressed pulse quality was almost unaffected by the imposed nonlinear phase. The grating separation in the grating compressor was just ~ 2 cm and the throughput efficiency was 73 % resulting in 21 W of recompressed average power. The measured autocorrelation is shown in figure 7.7 (right). The autocorrelation width was 320 fs corresponding to 240 fs pulse duration (deconvolution factor of 1.33). Consequently, the pulse peak power was as high as 5 MW after compression. The slight reduction in pulse duration compared

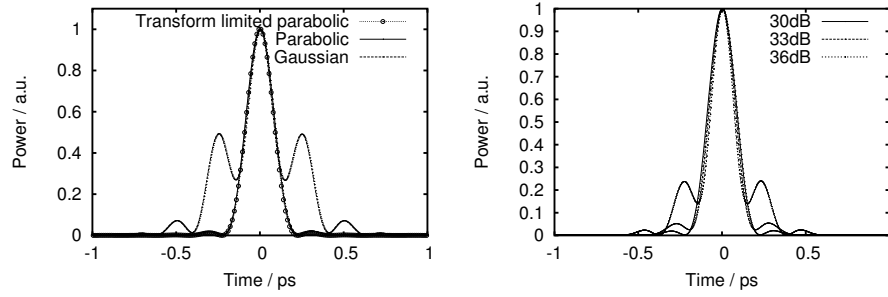


Figure 7.9: Calculated output pulses after amplification and subsequent compression. Left: an initial parabolic and an initial Gaussian pulse with the same characteristics as the pulse in the experiment. For comparison a transform limited parabolic pulse is also shown (filled circles). Right: amplification of the parabolic pulse at three different total gains in the amplifier.

to the oscillator was made possible by the bandwidth enhancement in the amplification stages. At the highest power levels wings in the autocorrelation are developing, however, they contain just a minor part of energy (compare e.g. to the calculations below (figure 7.9)). To validate that improved pulse quality was indeed obtained as a result of parabolic shaped pulses and in spite of the development of these wings, the accumulated nonlinear phase shift in the amplifier can be calculated:

$$\phi_{NL} = \gamma \int_0^L |a(z, t = 0)|^2 dz \quad (7.7)$$

If ϕ_{NL} is below 1 a linear propagation is assumed [116]. Above this value, the pulse quality usually degrades due to the non-compressible higher order nonlinear phase [116]. According to the simplified theory for amplification of parabolic pulses, mentioned above, this value should not be a limit. In fact ϕ_{NL} was calculated to be in the range of 8 for the present amplifier. To further prove the importance of the pulse shape, a simulation of the amplifier was performed, by solving the NLSE. The simulation includes dispersion, $\beta_2 = 0.020 \text{ ps}^2/\text{m}$ and $\beta_3 = 0.00039 \text{ ps}^3/\text{m}$, nonlinearity, $\gamma = 2.6 \cdot 10^{-4} (\text{m W})^{-1}$, constant longitudinal gain, $g = 5.76 \text{ m}^{-1}$ corresponding to a total gain of 30 dB in the 1.2 m long amplifier fiber. Furthermore, the gain was assumed to have a parabolic spectral shape with a FWHM spectral width of 40 nm. A parabolic input pulse of 10 ps (FWHM) with a 12.1 nm FWHM spectral width and a pulse energy of 1.76 nJ was used. For comparison a simulation was also performed on the same amplifier with a Gaussian input pulse with the same temporal and spectral widths and input pulse energy. After amplification, the minimum pulse duration was found by applying negative dispersion. Figure 7.9 (left) shows the difference between the resulting output pulses. As seen the parabolic input pulse also cor-

responds to a transform limited parabolic output pulse. The Gaussian pulse, however, has developed considerable wings, containing a substantial part of the pulse energy. With the numerical mode at hand, it is now also possible to investigate the limit of parabolic pulse amplification. According to the simplified analytical theory above, no limit should exist in principle. However, using the numerical model, it was found that the gain bandwidth which is not included in the simple analytical theory influences the output pulse. The explanation for this is that the spectral shape of the pulse is affected by the gain bandwidth and, hence, also the temporal shape of the pulse. As the temporal shape deviates from the ideal parabolic shape, the nonlinear phase shift accumulated by the pulse is no longer quadratic, which can be seen by the development of wings on the minimal pulse duration. Figure 7.9 (right) shows the resulting output pulses from the amplification and compression of the same parabolic pulse as used above, but with a varying gain, g , in the amplifier. Three different values of g were chosen, corresponding to a total gain of 30 dB, 33 dB and 36 dB. As can be seen, wings also start to develop as the gain is increased. At an amplification of 33 dB the wings still contain an acceptable low amount of energy and at this amplification level the nonlinear phase shift was calculated to 15.9. This is considerable more than the value of 1 for other pulse shapes, such as Gaussian and sech^2 shapes. The development of wings in the experiments already at a nonlinear phase shift of 8 may be a consequence of slight deviation from an ideal parabolic pulse already on the input side. However considerable improvement compared to amplification of non-parabolic pulses have been obtained.

7.5 Outlook

From both the theoretical analysis and from the experimental results it is evident, that increased pulse quality can be obtained at higher pulse energies by direct amplification of parabolic pulses. Pulse energies above the theoretical limit predicted for self-similar amplifiers and above the nonlinear limit in the amplifier have been experimentally demonstrated. It was however theoretically shown that amplification of parabolic pulses is also limited by the finite bandwidth of the gain medium. Many of the limiting problems can be avoided by controlling the input pulse parameters. The output spectral width can be reduced by increasing the pulse duration on the input side. Even though the principle is the same as in chirped pulse amplification, much smaller chirps are required, as larger nonlinear phase shifts can be tolerated. If parabolic pulse amplification is combined with a chirped pulse amplification setup, and the pulses are chirped to 1 ns before amplification, it is predicted that multi-mJ femtosecond pulse are feasible [14].

As illustrated by the experimental results, the initial pulse shape plays an important role in the final pulse quality. A scaling of the pulse energy from parabolic amplifiers depends on available initial pulse shapes. As opposed to the use of oscillators operating in the self-similar regime, where the output pulses

are not guaranteed to be perfectly parabolic, perfect parabolic input pulses for parabolic pulse amplifiers can be obtained from self-similar amplifiers operating sufficiently close to the asymptotic limit, and sufficiently far from the limits set by finite bandwidth and SRS. Hence the use of parabolic pulse amplification could be used to extend the limited pulse energy from self-similar amplifiers. Alternatively, and perhaps much more interesting, parabolic pulses can also be generated through linear pulse shaping in e.g. fiber Bragg gratings [117]. An initial parabolic pulse is not necessarily the best candidate for further pulse energy scaling. The possibility of arbitrary initial pulse shapes through linear pulse shaping may be used to overcome even the limit set by the finite bandwidth of the amplifier. The accumulated nonlinear phase shift is primarily accumulated during the last part of the amplifier, where the pulse peak power is highest. Hence, an initial non-parabolic pulse shape which, as a consequence of the finite bandwidth of the amplifier, evolves into a parabolic pulse on the output side of the amplifier, will primarily have accumulated a linear chirp, and hence extends the limit set by the finite bandwidth.

Further power and energy scaling as a result of improved fiber design will also be possible in the future, because single-transverse-mode PCFs with core diameters of $60\text{ }\mu\text{m}$ and mode-field-areas of $2000\text{ }\mu\text{m}^2$ have already been realized.

An alternative and very interesting approach to the generation of high energy pulses from fiber amplifiers is through the generation of cubicon pulses. As much as $100\text{ }\mu\text{J}$ 650 fs pulses at 50 kHz have recently been demonstrated after prestretching in a simple single mode fiber (2 km), and after taking advantage of a clever scheme where the nonlinear phase shift in the amplifier is used to compensate for the residual third order dispersion of the pulses [118]. Although the pulses were not transform limited, and much power still resided in the wings of the pulses, the peak power was still impressively high.

7.6 Summary

In summary, a compact all-PM fiber femtosecond fiber laser source delivering pulse energies up to $1.25\text{ }\mu\text{J}$ at a high repetition rate of 17 MHz and a pulse durations of 240 fs has been demonstrated here. The use of polarization maintaining and polarizing fibers make the polarization control redundant. Furthermore, any complex pulse stretching is avoided in the setup. Nevertheless, the high energies are made possible by amplification of linearly chirped parabolic pulses in low-nonlinearity single-polarization PCFs. The obtained pulse energy is higher than the theoretically predicted limit for self-similar amplifiers. To the best of my knowledge this was the first experimental confirmation that parabolic pulses can lead to significant improved pulse quality in fiber amplifier systems.

CHAPTER 8

Dispersion compensation free mode-locked fiber laser and supercontinuum generation

This chapter presents an environmentally stable dispersion compensation free mode-locked fiber laser. The laser comprises only normal dispersive polarization maintaining fibers and no means of introducing anomalous dispersion are used. A short cavity length and a SESAM with a high modulation depth supplies the necessary pulse shaping to sustain stable mode-locking. The laser was developed as seed laser for NKT's high-average-power supercontinuum white-light source, and a supercontinuum with an average power of > 5 W (> 1 W in the visible, i. e. 470 nm-850 nm) is demonstrated. After this demonstration, NKT decided to focus on the development of their own fiber laser rather than purchasing commercially available lasers.

8.1 Introduction

As argued in chapter 5, one of the main problems in obtaining an all-fiber environmentally stable laser based on Yb doped fibers is the lack of environmentally stable fiber components with anomalous dispersion in this wavelength range. If pulses considerably shorter than 1 ps are required, anomalous dispersion for dispersion compensation is necessary. However, for some purposes a mode-locked laser with a narrow spectral range is preferred. For other purposes it is the realization of a mode-locked laser with a simple, but stable setup, which is the key issue.

Standard fibers have a high normal dispersion around 1030 nm and if a laser was realized with no means of temporal compression the pulse duration of a pulse launched into the laser would simply continue to increase every round trip until the pulse would eventually catch up with itself and turn into cw-lasing. This is not the case for lasers working solely in the anomalous dispersion regime. Here the nonlinear coefficient of the fiber has opposite sign of the dispersion, and by creating a soliton, the contribution to the chirp from the nonlinear phase shift can cancel the contribution from the dispersion. In the normal dispersion regime elements like e.g. the SC-PBG fiber used in chapter 5 have to be used to obtaining temporal compression every round trip.

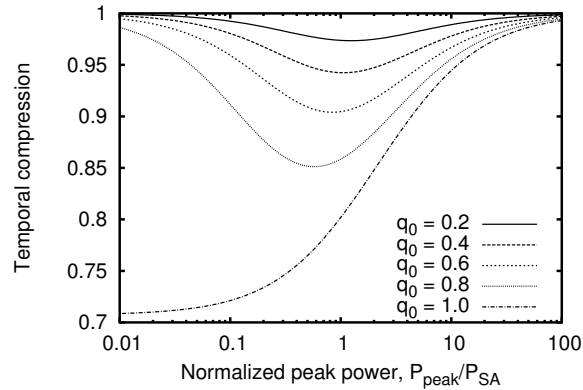


Figure 8.1: Calculated temporal compression of a Gaussian pulse in a SESAM. The temporal compression is plotted vs. normalized input peak power and for different modulation depths, q_0 .

The increase per round trip in pulse duration due to the dispersion in the laser depends on the spectral width of the pulse. A balance between temporal stretching and compression can hence be found if the spectrum is sufficiently narrow - even though the temporal compression is small. An alternative mean to the use of linear dispersive elements for temporal compression is by a strong nonlinear response from e.g. a SESAM. In the limit of a 100 % modulation

depth and an unsaturated SESAM, a Gaussian pulse experiences a temporal compression by a factor of $\sqrt{2}$. Figure 8.1 shows the temporal compression calculated by applying the effect of a SESAM (equation. 3.3) to a Gaussian pulse. For a smaller modulation depths than 100 % a smaller reduction is obtained, but as shown in the following, a sufficiently strong modulation depth supplies enough temporal compression, to obtain stable mode-locking. Dispersion compensation free mode-locked fiber laser have previously been reported in reference [119]. Here an environmentally stable dispersion compensation free mode-locked laser based solely on temporal compression in a SESAM is demonstrated. The laser is further used for high power supercontinuum generation after external amplification in a dispersion compensation free setup.

8.2 Experimental setup and results

Figure 8.2 shows a diagram of the laser, comprising a polarization maintaining (PM) WDM, 32 cm of highly doped ytterbium PM fiber (300 dB/m absorption at 976 nm) and a PM 20:80 coupler with PM fiber-pigtails (output coupling: 20 %). The coupler also works as a polarizer, transmitting only the light in the slow axis, and hence ensures that the output from the cavity is linearly polarized. The total length of fibers in the cavity was 1.38 m, resulting in a repetition rate of 71 MHz.

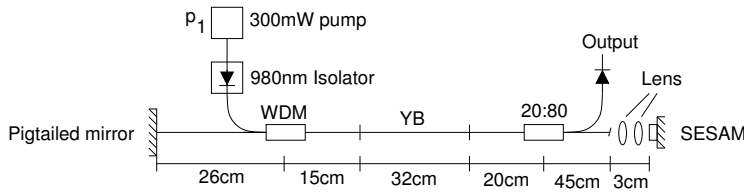


Figure 8.2: Diagram of the dispersion compensation free laser

A saturable absorber mirror (SESAM) with a modulation depth of 24 %, a recovery time of < 500 fs, a saturation fluence of $\sim 70 \mu\text{J}/\text{cm}^2$ and non-saturable losses of 16 % was used to mode-lock the laser. The other cavity mirror was a PM fiber-pigtailed mirror. A 300 mW fiber-pigtailed 976 nm laser diode was used to pump the oscillator and a fiber-pigtailed 976 nm isolator was used to protect the pump diode.

Figure 8.3 (left) shows the output spectrum from the laser vs. pump power, and figure 8.3 (right) shows the output power characteristics. As seen, stable mode-locking is obtained over a wide pump power range.

The output pulses of the laser are highly chirped, as there is no intra cavity dispersion compensation in the cavity. Figure 8.4 (left) shows the uncompressed output pulse at maximum pump power. The pulse has an autocorrelation FWHM of 16 ps, corresponding to a pulse duration of 11 ps. Fig-

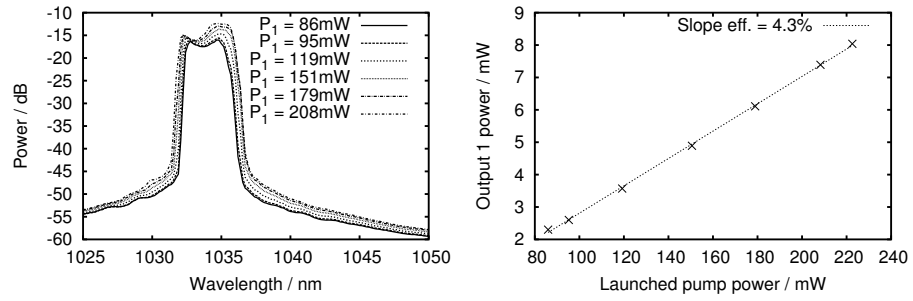


Figure 8.3: Left: Output spectrum vs. pump power. Right: output power characteristics.

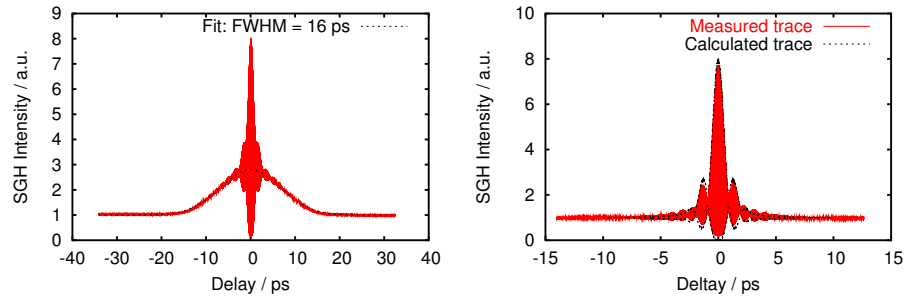


Figure 8.4: Left: Uncompressed pulse autocorrelation trace. 16 ps autocorrelation FWHM corresponds to a pulse duration of 11 ps. Right: Compressed pulse autocorrelation trace (measured and calculated).

Figure 8.4 (right) shows the measured autocorrelation trace of the compressed output pulses (compressed with an external grating compressor). The compressed pulses were obtained with a grating separation of 15 cm, corresponding to a total GVD of -1.97 ps^2 . The measured autocorrelation trace is compared to a calculated autocorrelation trace, obtained using a pulse retrieval algorithm. The pulse retrieval algorithm Fourier transforms the measured spectrum with a small amount of higher order chirp in order to match the measured autocorrelation trace. The measured autocorrelation trace can be seen to be in good agreement with the calculated autocorrelation trace, and hence the autocorrelation trace is deconvoluted to a pulse duration of 800 fs. Figure 8.5 shows the calculated pulse shape corresponding to the autocorrelation which gives the best fit to the measured autocorrelation trace. This is compared to the calculated transform limited pulse, and as one can see, the output pulse is slightly longer than the transform limit.

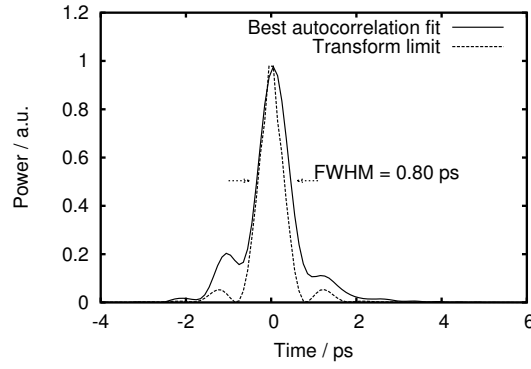


Figure 8.5: Temporal pulse shape of a transform limited pulse (calculated by Fourier transforming the measured spectra with zero phase), and of the pulse giving the best autocorrelation fit. The compressed pulse has a FWHM of 0.80 ps and is close to transform limit.

8.3 Supercontinuum generation with a dispersion compensation free setup.

The above mentioned oscillator was developed as seed-laser for NKT's high average power supercontinuum (SC) white-light source. Supercontinuum generation in nonlinear PCFs has for several years been studied as a source of spatially coherent broadband light [120]. The dispersion and nonlinearity of a PCFs can be controlled in the fiber design. The ability to move the zero dispersion wavelength closer to the visible wavelength range, has enabled generation of broad SC extending all the way down into the blue. Furthermore, a white-light fiber delivery is highly attractive for commercial applications such as spectroscopy, fluorescent microscopy [121], and optical coherence tomography [6]. The fiber delivery conveniently removes any restrictions of the possible application to the optical table and provides a diffraction limited output. The generation of wide SC in PCFs fibers has been demonstrated with femtosecond pulses, however, the SC spectra are typically jagged and the average optical power in the visible spectrum low. Picosecond pulses from bulk optical seed oscillators, on the other hand, have proven efficient for the generation of high average power, wide, and smooth SC spectra [122]. The difference between femtosecond and picosecond pulses, when pumping in the anomalous dispersion regime is in the number of fundamental solitons generated. If the input pulse is a transform limited femtosecond pulse, the soliton number is lower, and fewer fundamental solitons are generated. Bright visible SC have been generated through both nanosecond [123, 124] and femtosecond [125] dual-wavelength pumping of nonlinear PCFs with the fundamental wavelength at

~ 1060 nm and second harmonic wavelength at 530 nm. Although the mechanisms behind dual-wavelength pumping are well understood [125], pumping with high average power picosecond pulses at a single wavelength is a simpler route toward bright visible SC. For a thorough review of supercontinuum generation in PCFs see [30].

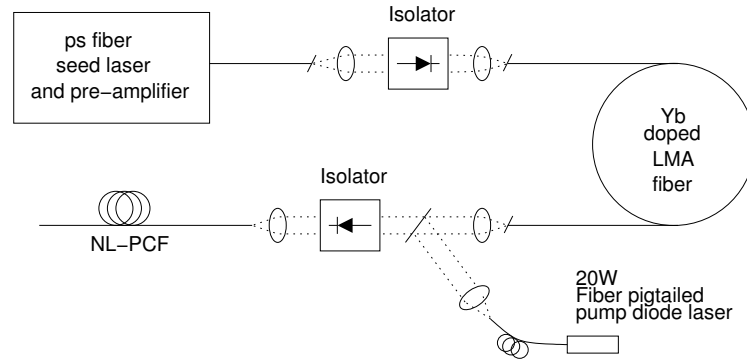


Figure 8.6: Diagram of the dispersion compensation free supercontinuum setup

Figure 8.6 shows the setup for generation of high average power supercontinuum. The seed oscillator was a 70 MHz oscillator based on the above mentioned mode-locking principle, but with a slightly different output coupling. Instead of the fixed 20:80 output coupler, which introduces a loss two times per round trip and hence splits the output power in two, a PM fiber-pigtailed polarizing beam splitter was combined with a quarter-wave plate. The quarter-wave plate was inserted in between the two aspheric lenses on the SESAM side, to yield a tunable output coupling, resembling the bulk version used in figure 6.2. The output power from the oscillator was pre-amplified in a pre-amplifier based on the same fibers as the oscillator, and the output launched into a non-PM large mode area (LMA) double clad PCF, which was pumped from the other side with a 20 W fiber-pigtailed laser diode. Figure 8.7 (left) shows a SEM image of the LMA fiber. A dichroic mirror was used to separate the amplified output, before it was launched into a 12 m long nonlinear (i.e. small core ($MFD = 3.3 \mu\text{m}$)) PCF. Figure 8.7 (right) shows a SEM image of the nonlinear fiber. Bulk isolators were used on both sides of the LMA fiber. Due to the large core of the LMA fiber ($MFD = 20 \mu\text{m}$), it was possible to amplify the output from the pre-amplifier directly and without significant pulse distortions, and hence stretching of the pulse prior to the amplification and subsequent compression could be avoided.

The output from the seed laser was amplified to 8.5 W in the LMA fiber, and the output was launched into the nonlinear PCF with an aspheric lens, resulting in a maximum of 5.2 W average power supercontinuum. The generated supercontinuum is shown in figure 8.8 on a linear scale and covers the range from 470 nm to above 1800 nm. The visible part of the spectrum contained more than 1.2 W average power (measured directly after spectral filtration with two

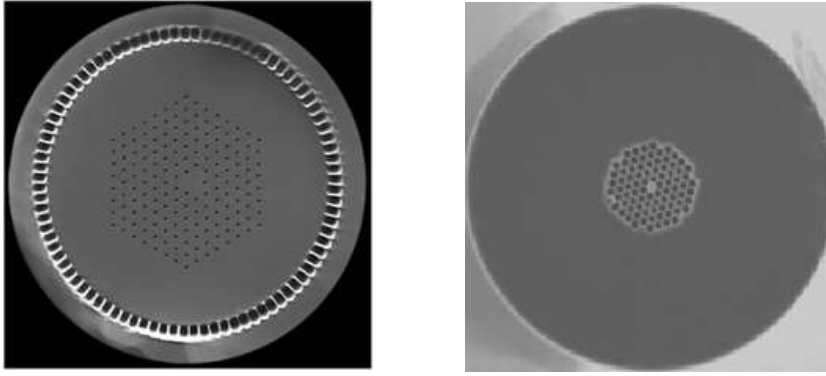


Figure 8.7: Left: SEM image of the LMA Yb-doped fiber. The fiber has a double cladding structure with an outer air cladding and supports single mode laser light guidance in the core and multi mode pump light guidance in the inner cladding. Right: SEM image of the nonlinear PCF.

broadband dielectric mirrors (465 nm to 850 nm) and hence contributions from the seed itself and the infrared part of the spectrum are not included).

8.4 Outlook

Although the short term stability of the aforementioned laser was good, and it could be operated for days without degradation, the long term stability (i.e. > 100 h) was tested to be inadequate. The problem stems from the SESAM, where the deposited heat gradually changed the parameters and as the only pulse shaping mechanism in the laser is the nonlinear effect in the SESAM, small changes here strongly affects the pulse. Furthermore, the presented method is only applicable to mode-lock short lasers. If lower repetition rates (i. e. 10-60 MHz) are desired, stronger temporal compression is required per round trip. One possibility is the use of strong spectral filtration (e.g. by introducing a fiber Bragg grating) to shape the pulse. Succeeding the results presented here, mode-locked fiber lasers with repetition rates down to 20 MHz have also been realized at NKT with the use of uniform unchirped fiber Bragg gratings for strong intra cavity spectral filtration. A high average power supercontinuum source based on these lasers will be commercially available in the near future. A 33 MHz dispersion compensation free fiber laser was also build as a replacement for the Ti:sapphire laser in our lab, and is now used for CARS microscopy. The laser also comprised the high modulation depth SESAM and further a 2 nm broad apodized unchirped fiber Bragg grating. After external amplification and SPM induced spectral broadening, the output is compressed to 110 fs, and used to create a soliton which can be red-shifted from 1030 nm and all the way out to 1450 nm in a PCF with anomalous dispersion in this range. Combined with

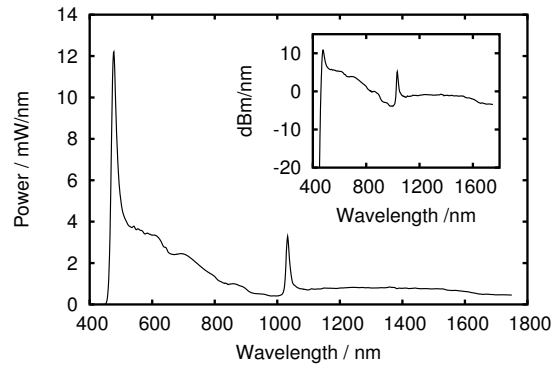


Figure 8.8: Supercontinuum from the dispersion compensation free setup on a linear scale. Insert: log scale.

another close-to transform-limited amplified picosecond output from the laser, this constitutes an excellent source for CARS microscopy [34]. In the next chapter the limit in repetition rate from a different type of short pulsed mode-locked laser is explored, using strong spectral filtration as the primary pulse compression technique.

8.5 Summary

In summary, it has been experimentally demonstrated, that mode-locking of an ytterbium based fiber laser can be obtained without the presence of intra-cavity dispersion compensation. The result is an environmentally stable fiber laser based on normal dispersive PM fiber pigtailed components only. The laser delivering picosecond pulses was amplified and used to generated a high average power supercontinuum covering the range from 470 nm to above 1800 nm with more than 1.2 W of visible power.

CHAPTER 9

Environmentally stable low repetition rate nonlinear polarization rotation based fiber laser

This chapter presents the design and realization of an environmentally stable mode-locked fiber laser based on nonlinear polarization rotation. The laser is based on a novel laser configuration which has negligible low power steady state reflectivity from one side, and hence requires an alternative mechanism to initiate mode-locking. The laser operates in the noise-like mode-locked regime, but in spite of this, 8.3 ps pulses are obtained at a repetition rate of 2.91 MHz and after external amplification to a pulse energy of 141 nJ, 213 mW of supercontinuum extended to the orange part of the visible spectrum is obtained from a totally integrated system with no sections of free space optics.

9.1 Introduction

The lasers described in this thesis so far have all been based on SESAM mode-locking. An alternative and widely researched possibility is to use nonlinear polarization rotation (NPR), as also described in section 2.3.3. The most frequently researched laser configuration utilizing NPR is the fiber ring laser [12, 24, 42, 46, 54–57, 97]. In this laser configuration an isolator ensures unidirectional pulse propagation around a fiber ring containing the gain medium. A polarizer is included in the ring to create a nonlinear loss after NPR in the ring. Wave plates are placed on both sides of the polarizer to control the polarization state of the light before and after NPR. Impressive results in terms of pulse energy, duration and peak power have recently been reported from ytterbium based fiber ring lasers [24, 54, 56, 57]. The advantage of fiber ring lasers are the many degrees of freedom available when aligning the lasers, and hence the laser can be pushed to limits of higher pulse energy and short pulse durations. The disadvantage is however, as also described in chapter 6, that fiber ring lasers cannot be implemented as intrinsically environmentally stable lasers. As NPR is an intensity dependent distributed change of the polarization state of the light as it propagates inside the fiber due to a non-linear coupling between the two orthogonal polarization states, NPR is strongly coupled to the pulse polarization evolution inside the laser. Hence the NPR in the fiber ring is affected by the polarization evolution due to bend induced birefringence in the non-PM fibers, and this bend induced birefringence is susceptible to changing temperatures. There are however good reasons for looking into environmentally stable laser configurations utilizing NPR. First of all, as NPR originates from the interaction with the electrons in the fiber, it is an intrinsically fast response (infinitely fast compared to pulse durations). Furthermore, as SESAMs are one of the optically most fragile components of fiber lasers, and as a strong perturbation of a laser oscillator may cause the gain medium to Q-switch, and thereby emit a short intense pulse of high peak power, the SESAM can easily be permanently damaged. A solution to this problem has been found [69], and patented by IMRA [126]. The solution involves growing a two-photon absorbing layer on top of the SESAM, in order to prevent Q-switching. However, it is still interesting to look into other possibilities for lasers operating in harsh environments.

As NPR only occurs if the light is elliptically polarized, PM fibers with light in only one linear polarization axis cannot be used. Environmentally stable lasers based on NPR have previously been reported [58, 101], and patented [127–129]. All previously proposed laser configurations use a Faraday Mirror (FM) (a Faraday rotating element with a 45° single pass polarization rotation combined with a mirror). The FM cancels the effect of environmentally induced changes of the birefringence. In all cases a second Faraday rotating element was also needed, and the polarization evolution is only environmentally stable in between the two Faraday elements. In references [58, 127–129] the rest of the cavity comprises free space optics only. Figure 9.1 shows a diagram of a typical

configuration [129]. In reference [101] the rest of the cavity in addition to free space optics, also comprises a PM HC-PBG fiber in a ring configuration. Furthermore, the use of NPR also requires a polarization dependent loss (e.g. in the form of a polarizer). If an environmentally stable fiber laser based on the principle in references [58, 101, 127–129] were to be implemented with no sections of free space optics, a fiber-pigtailed component comprising both wave-plates and the second Faraday rotating element in a single component would have to be manufactured, as a fiber section between the wave-plates and the second Faraday rotating element would not be environmentally stable - even if PM fibers were used.

In this chapter a novel laser configuration based on the environmental stabilization of a FM, but without the second Faraday rotating element is investigated. The advantages of this approach is that the laser can be implemented with no sections of free space optics with currently available fiber pigtailed components. Different experimental implementations of the proposed laser configuration are demonstrated accompanied by numerical calculations. Low repetition rate single pulse lasing can be obtained directly from the oscillators, with the advantage of high pulse energy. The laser operates in the noise-like mode-locked regime, but in spite of this, average pulse durations of 7.3 ps are obtained at a repetition rate of 2.91 MHz directly from one experimental version of the laser. After external amplification in a simple standard single-mode fiber amplifier, a pulse energy of 141 nJ is obtained and after supercontinuum generation in a photonic crystal fiber, 213 mW of supercontinuum extended to the orange part of the visible spectrum is obtained from a totally integrated system with no sections of free space optics. This is a more than a two fold increase compared to what is obtainable from NKT's commercial nanosecond based supercontinuum source, SuperK-Red [75], (where the average power is limited by optical damage of the components by the high energy nanosecond pulses). An experimentally found limit in repetition rate of 360 kHz with single pulse mode-locking is demonstrated, and was found to depend the nonlinear losses associated with stimulated Raman scattering (SRS). Finally an all-polarization maintaining (all-PM) fiber laser is demonstrated utilizing nonlinear polarization rotation (NPR) in a PM fiber with the advantage of an mode-locking mechanism which is in-

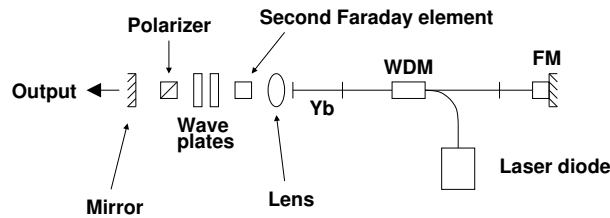


Figure 9.1: Typical diagram of previously proposed environmentally stable fiber lasers based on NPR [129]. (FM: Faraday Mirror).

trinsically independent of even strong bend induced birefringence, and hence extremely environmentally stable.

9.2 Faraday mirror

Before introducing the laser configuration, it is advantageous to look at the theory behind the FM. The analysis involves propagation of the two orthogonal polarization components of the slowly varying electrical field amplitudes through both reciprocal and nonreciprocal elements in both directions. It is advantageous to represent the field in both a linear (LP) and circular polarized (CP) basis. Transformations between the two basis is carried out with an unitary transformation:

$$\vec{A}^{CP} = U \vec{A}^{LP}; \quad \vec{A}^{LP} = U^\dagger \vec{A}^{CP},$$

where:

$$\vec{A}^{CP} = \begin{pmatrix} A_+ \\ A_- \end{pmatrix}; \quad \vec{A}^{LP} = \begin{pmatrix} A_x \\ A_y \end{pmatrix};$$

$$U = \frac{1}{\sqrt{2}} \begin{pmatrix} 1 & i \\ 1 & -i \end{pmatrix}; \quad U^\dagger = \frac{1}{\sqrt{2}} \begin{pmatrix} 1 & 1 \\ -i & i \end{pmatrix}.$$

To handle waves moving in both directions inside a medium, care must be taken when choosing the coordinate system. If the coordinate system is chosen always to be right handed orientated with its z-axis in the direction of propagation, the transformations between a forward system and a backward system can be made with a rotation around e.g. the x-axis, such that $y \rightarrow -y$ and $z \rightarrow -z$. If a propagation through a lossless linear medium with zero dispersion in the forward coordinate system is described by the operator, \vec{O} , then a propagation through the medium in the reverse direction and in the backward coordinate system is described by the operator $\overleftarrow{O} = P \vec{O}^t P$ [42, 130], where superscript t means transposed and

$$P = \begin{pmatrix} 1 & 0 \\ 0 & -1 \end{pmatrix}$$

takes care of changing the sign on the y-component.

A Faraday mirror consists of a Faraday rotating element and a mirror. The mirror is described in the LP basis by:

$$M^{LP} = \begin{pmatrix} 1 & 0 \\ 0 & -1 \end{pmatrix},$$

where the -1 comes from the change of the forward to the backward coordinate system. The Faraday rotating element rotating the light by 45° is represented in

the CP bases by:

$$F(\theta_F)^{CP} = \begin{pmatrix} e^{i\theta_F} & 0 \\ 0 & e^{-\theta_F} \end{pmatrix},$$

where $\theta_F = VHL = \pi/4$ is the Faraday rotation angle (V is the Verdet constant, H the magnetic field, L the medium length). In the Faraday mirror the light is first sent through the Faraday element, reflected on the mirror, and finally sent back through the Faraday element:

$$FM^{LP} = P(U^\dagger F(-\theta_F)^{CP} U)^t P \cdot M^{LP} \cdot U^\dagger F(\theta_F)^{CP} U = \begin{pmatrix} 0 & -1 \\ -1 & 0 \end{pmatrix}.$$

Notice that the Faraday rotation angle changes sign in the backward coordinate system because the H-field is now in the -z direction.

It was shown in references [130–132] that a FM is a universal compensator for polarization changes induced by the birefringence of an arbitrary birefringent lossless linear medium with no dispersion. Such a general medium may be described by a unitary transformation containing 3 free parameters (where the 4th parameter - describing a global phase - is omitted):

$$O^{LP} = \begin{pmatrix} te^{-i\phi} & i\sqrt{1-t^2}e^{-j\theta} \\ i\sqrt{1-t^2}e^{j\theta} & te^{i\phi} \end{pmatrix}.$$

Propagation through the birefringent medium, reflection from the Faraday mirror and propagation back through the birefringent medium is described by the operator:

$$P(O^{LP})^t P \cdot FM^{LP} \cdot O^{LP} = \begin{pmatrix} 0 & -1 \\ -1 & 0 \end{pmatrix}.$$

That is: the polarization of the reflected wave is independent of the birefringent medium and is always perpendicular to the polarization state of the forward moving wave. This is truly an interesting property of a FM. The operator, O^{LP} , could in principle represent any combination of wave plates, or a fiber with arbitrary bend induced and hence unknown birefringence. The property that the reflected light is orthogonally polarized to the incoming light is also true at any point inside the fiber. The origin of this property is that the FM rotates the major axis of an incoming arbitrary elliptically polarized light beam with 90° and changes the handedness (right or left handed) without changing the ellipticity. On propagation back through the arbitrary birefringent medium, it appears that the orthogonal birefringent axes have been switched, and the light now experiences the phase delays between the axes in reverse. Even if the arbitrary birefringence of a non-PM fiber changes due to environmentally induced effects, the FM will compensate. A second advantage of a FM is that the group velocity walk-off between the two different polarization axes in e.g. a PM fiber is

also automatically compensated, as the light returns using opposite polarization axis.

If a second Faraday rotating element is added before the arbitrary birefringent medium, the effect is:

$$P(U^\dagger F(-\theta_F)^{CP} U \cdot O^{LP})^t P \cdot FM \cdot O^{LP} \cdot U^\dagger F(\theta_F)^{CP} U = \begin{pmatrix} -1 & 0 \\ 0 & 1 \end{pmatrix}.$$

Hence the second Faraday rotating element changes the polarization state back to the incoming polarization state. Again the -1 comes from the change of coordinate system. Inclusion of polarization independent losses and polarization independent birefringence is straight forward, as it does not change the linear polarization evolution. On the other hand, if O^{LP} was a nonlinear function of the optical field, the statement that a FM compensates for the polarization changes of an arbitrary birefringent medium is in general no longer valid. In the special case where the medium is isotropic, lossless, dispersion free but nonlinear, the operator for NPR is given by [42]:

$$O_{NPR}^{CP} = \begin{pmatrix} e^{i\Phi_+} & 0 \\ 0 & e^{i\Phi_-} \end{pmatrix},$$

where $\Phi_\pm = \frac{2}{3}\gamma L(|A_\pm|^2 + 2|A_\mp|^2)$ is the nonlinear phaseshift. The effect of propagating through the nonlinear medium, reflecting off the FM and propagating back through the nonlinear medium, can be calculated by applying the operators in sequence to the field, \vec{A}^{LP} :

$$U^\dagger O_{NPR}^{CP} U \cdot FM^{LP} \cdot U^\dagger O_{NPR}^{CP} U \cdot \vec{A}^{LP},$$

where is was used that $\vec{O}_{NPR}^{CP} = \overleftarrow{O}_{NPR}^{CP}$ because the medium is isotropic. Notice that the application of each operator is not just a matrix multiplication, as the matrix elements depend on the vector it operates on. As a result the outcome depends on the input polarization state. To quantify this, a polarizer O_P^{LP} :

$$O_P^{LP} = \begin{pmatrix} 1 & 0 \\ 0 & 0 \end{pmatrix},$$

and a single wave plate, O_{WP}^{LP} :

$$O_{WP}^{LP} = \begin{bmatrix} e^{i\Delta} \cos^2(\theta) + e^{-i\Delta} \sin^2(\theta) & i \sin(2\theta) \sin(\Delta) \\ i \sin(2\theta) \sin(\Delta) & e^{-i\Delta} \cos^2(\theta) + e^{i\Delta} \sin^2(\theta) \end{bmatrix},$$

are further included before propagation through the nonlinear medium. The effect of the wave plate is to change the polarization state to elliptical. $\Delta = \pi$ corresponds to a half-wave plate, $\Delta = \pi/2$ to a quarter-wave plate, etc., and θ represent the rotation angle between the axis of the wave plate and the axis of the polarizer. The reflection back through the polarizer can be calculated as:

$$\vec{A}_{out}^{LP} = P(O_{WP}^{LP} O_P^{LP})^t P \cdot U^\dagger O_{NPR}^{CP} U \cdot FM^{LP} \cdot U^\dagger O_{NPR}^{CP} U \cdot O_{WP}^{LP} O_P^{LP} \cdot \vec{A}_{in}^{LP}.$$

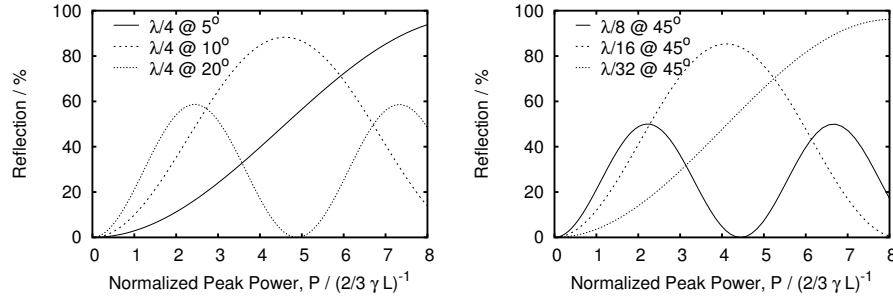


Figure 9.2: Calculated reflection back through a polarizer, a wave plate, and a nonlinear medium with NPR after reflection off a FM as function of normalized input peak power. Left: With a quarter wave plate at different rotation angles. Right: With an 8th wave, a 16th wave and a 32th wave plate at a rotation angle of 45° ($\theta = \pi/4$).

Figure 9.2 shows the reflection, $|\vec{A}_{out}^{LP}|^2/|\vec{A}_{in}^{LP}|^2$, for different wave plate retardations, Δ , and rotation angles, θ . At smaller rotation angles or with smaller wave plates (smaller Δ), a higher input peak power is needed to get the maximum reflection, but a higher maximum reflection is also obtained. Even more importantly: at low input peak powers, the reflection tends towards zero. The second Faraday rotating element was included after the polarizer and the section of wave plates in references [58, 127–129], as a relative high low power reflectivity is usually most practical inside a mode-locked laser, in order to start the laser. However, as the FM thereby no longer environmentally stabilizes the section of wave plates, free space wave plates were used in references [58, 127–129]. The laser configuration presented in this chapter explores the possibility of omitting the second Faraday rotating element. As a consequence an alternative method to initiate mode-locking has to be used. Further, high reflectivities are only obtainable at nonlinear phase shifts above the noise-free limit. The laser should be operated on the first increasing slope if the reflectivity curve (see figure 9.2).

9.3 Proposed laser configuration

Figure 9.3 shows a diagram of the proposed laser configuration. Besides the polarizer, the wave plates, the FM, and a long fiber between the FM and the wave plates in which NPR can take place (referred to as NPR fiber), the laser should also include an output coupler, a gain fiber, and a WDM to couple pump power into the gain fiber. As only the fiber between the FM and the polarizer is being environmentally stabilized by the FM, the rest of the cavity (i.e. the gain

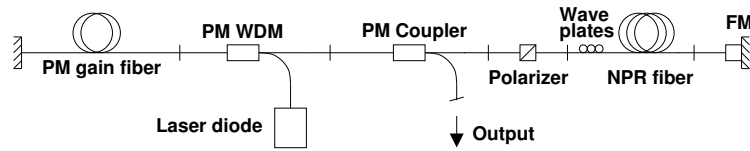


Figure 9.3: Diagram of the laser configuration.

fiber, the WDM, the coupler, and the polarizer) should be PM fibers and PM fiber-pigtailed components and the polarizer aligned to the slow axis of these PM fibers, so that the whole laser is environmentally stable.

9.4 Startup of mode-locked lasing

In a mode-locked laser where a specific short pulse is the most favourable solution to the cavity, this pulse is not automatically guaranteed to occur as soon as the pump power is turned on. On the contrary, most mode-locked lasers go through a short phase of cw lasing before mode-locked lasing is initiated. A pulse which is not the stable solution may under certain circumstances evolve into the stable solution, and such an initial pulse may occur out of noise from the initial cw lasing [133, 134]. This is why cw lasing usually also has to be a good solution to the cavity with relative low losses per round trip.

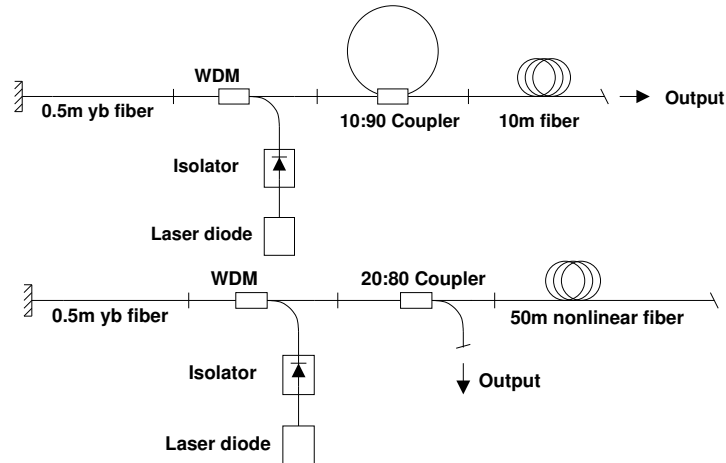


Figure 9.4: Top: Diagram of a self-Q-switched laser configuration with a ring interferometer. The ring interferometer simply consists of a e.g. a 10:90 coupler coupling 10 % into the loop. Bottom: Diagram of a self-Q-switched laser configuration without a ring interferometer.

As cw lasing is not possible for the proposed laser (figure 9.3), another me-

thod is needed to start the laser. It was shown in references [135, 136], that if reflection from one side of a gain medium is suppressed, the laser may self-Q-switch or passively Q-switch, generating a rather regular train of nanosecond pulses with a spacing of the order of the lifetime of the gain medium and inversely proportional to the pump power (i.e. with a repetition rate in the order of 1-10 kHz for ytterbium doped fibers). It is well known that Stimulated Brillouin Scattering (SBS) in a long fiber can create a nonlinear feedback mechanism acting like an artificial saturable absorber and hence cause the generation of nanosecond pulses. SBS is like stimulated Raman scattering (SRS), an interaction with the phonons of the material, but unlike SRS, SBS is an interaction with the acoustical phonons. Because of energy and momentum conservation in the interaction process, the SBS gain is zero in the forward direction, and hence the only direction with a nonzero SBS gain is in the backward direction. The frequency shift associated with SBS (~ 17 GHz) is much smaller than the SRS frequency shift (~ 13 THz). When the pulse spectrum is much broader than the SBS gain bandwidth (i.e. for transform limited pulses shorter than ~ 10 ps), the effect of SBS can be neglected [1]. However, before the onset of mode-locked lasing, SBS may play a considerable role. The passive Q-switching mechanism was enhanced with the use of a ring interferometer in references [136, 137], and the mechanism was found to depend on Rayleigh Back Scattering (RB) and SBS at the resonance frequencies of the ring interferometer. This enabled self-Q-switching even at low pump powers. Figure 9.4 (top) shows a diagram of a typical passively Q-switched laser configuration with a ring interferometer.

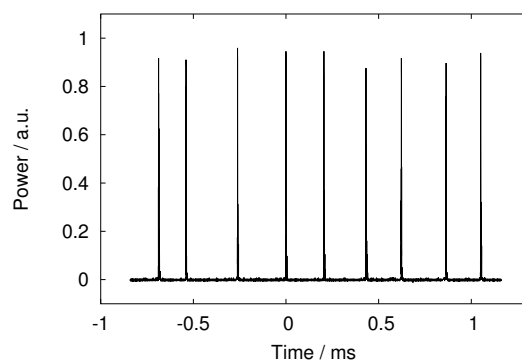


Figure 9.5: Pulse train of nanosecond pulses from a passively Q-switched fiber laser.

Ring interferometers are however not very practical inside a mode-locked fiber laser, because of the coupled cavity effects resulting in multi-pulsing. However, passive Q-switching can be obtained with a ytterbium doped fiber as the gain medium in a cavity without using a ring interferometer. This is because ytterbium doped fibers have a pronounced tendency to self-Q-switch with pulse

durations usually an order of magnitude shorter (i.e. $\sim 1\text{-}2\text{ ns}$) and correspondingly intense compared to pulses from e.g. erbium doped fiber lasers (i.e. $\sim 10\text{-}15\text{ ns}$) [135]. Figure 9.4 (bottom) shows the diagram of a passively Q-switched laser configuration, and figure 9.5 shows a typical output pulse train of nanosecond pulses. The tendency to self-Q-switch is enhanced if the long fiber has high RB and SBS coefficients. The RB coefficient is proportional to the linear loss of the fiber and the SBS coefficient is inversely proportional to the MFD of the fiber. Using a short highly ytterbium doped fiber as gain medium further increases the tendency to self-Q-switch. However, as the gain bandwidth of ytterbium overlaps with the gain band of 976 nm pump laser diodes, it is advantageous to use an isolator in front of the pump diode. Otherwise the interaction between the two gain media can Q-switch the laser diode. As a result the laser facet of the laser diode may be damaged, and the laser diode destroyed.

To incorporate the self-Q-switching mechanism as a starting mechanism of a mode-locked fiber laser, several things have to be fulfilled. First of all the reflection into the gain medium should be suppressed from one side. This is possible if the gain medium is not placed in the section between the polarizer and the FM. Furthermore, the fibers on the side of the gain medium with suppressed reflection must be long enough to facilitate passive Q-switching. Finally, the feedback in the presence of a mode-locked pulse train should be sufficient to saturate the gain medium enough for passive Q-switching to be efficiently suppressed after the onset of mode-locked lasing.

9.5 Experimentally implemented laser configuration

Figure 9.6 shows a diagram of the first experimentally implemented laser configuration to be presented. All components in the laser were PM fiber pigtailed

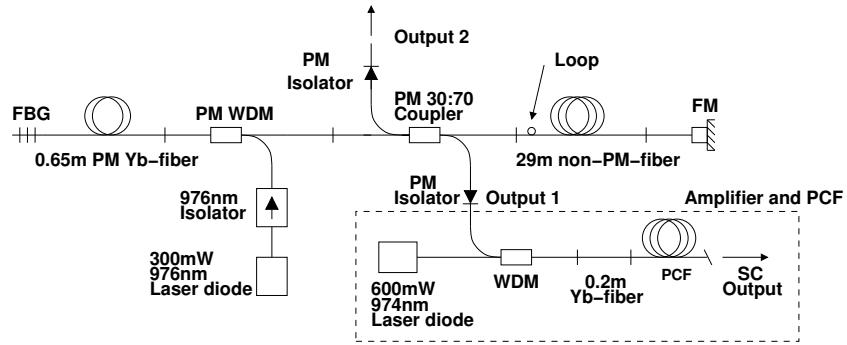


Figure 9.6: Diagram of an experimental implementation of the proposed laser configuration. (HR: High Reflector, FBG: Fiber Bragg grating, FM: Faraday Mirror). The primary output (Output 1) is connected to an amplifier and a photonic crystal fiber (PCF) for supercontinuum generation.

components. The fiber pigtails on all the components were Panda 980 fibers with MFD $\sim 7 \mu\text{m}$, and were all $\sim 1 \text{ m}$ long. The gain medium of the laser was a 0.65 m long yb-doped ($\sim 300 \text{ dB/m}$ absorption at 976 nm) PM fiber, pumped through a thin-film filter WDM with a 300 mW 976 nm laser diode. The PM yb-doped fiber had a MFD of $4.8 \mu\text{m}$. The coupler was a 30:70 PM coupler (30 % output coupling). The primary output is labeled "Output 1" in figure 9.6, and there is also a second output, "Output 2". PM-fiber pigtailed isolators were used to eliminate back reflections into the cavity. The coupler serves several purposes. The coupler is primarily used to couple light out of the cavity, but in addition to this, it has the property that only light polarized along the slow axis of the fiber is transmitted, and hence it effectively works as a polarizer. The NPR fiber used between the coupler and the FM was chosen to have a relative high loss and small MFD in order to seed initial Q-switching. The NPR fiber was a 29 m long non-PM fiber with a MFD of $3.33 \mu\text{m}$ and 9 dB/km attenuation at 1060 nm. The dispersion of the NPR fiber was measured to $\beta_2 = 0.046 \text{ ps}^2/\text{m}$, $\beta_3 = -9.6 \cdot 10^{-6} \text{ ps}^3/\text{m}$ at 1030 nm.

To change the polarization state to an elliptical state at the entrance to the NPR fiber, a small loop (with a diameter of 33 mm) was made at the beginning of the fiber. Because of bend induced birefringence, this creates a wave plate effect corresponding to a retardation of $\Delta = 3\pi/8$ at 1030 nm. The plane of the loop was fixed with a small angle ($\theta \sim 5^\circ$) compared to the slow axis of the fiber, and hence also to the axis of the polarizer. Notice that all linear birefringence introduced by bending the fibers is canceled by the FM, and the effect of the wave plate is only to ensure a change of the polarization state away from linear in order to enable NPR.

An apodized unchirped fiber Bragg grating (FBG) with a bandwidth of 2 nm at a central wavelength of 1034 nm was used as cavity mirror at the other end of the cavity. A FBG is made by doping the fiber (with e.g. Germanium and Hydrogen) and subsequently exposing the fiber to UV light. The energetic UV photons create defects at the dopant sites which cause an increase of the index of refraction of up to $\sim 10^{-3}$. Phase masks are used to ensure spatial periodicity of the UV-exposure since it is the periodic variation in the refractive index which cause the reflection. If the periodicity of the index change increases or decreases along the FBG, the FBG is said to be chirped, and if the periodicity does not change, it is said to be unchirped. If the magnitude of the index modulation is constant over the entire length of the grating, this results in spectral sidebands. Sidebands can be avoided by varying the index modulation (e.g. with a Gaussian profile) along the grating. The FBG is then said to be apodized. For further information about FBGs see e.g. [138].

9.6 Experimental results

Mode-locking of the laser starts out from an initial phase of self-Q-switching. Initially nanosecond pulses are generated with a rather irregular temporal spac-

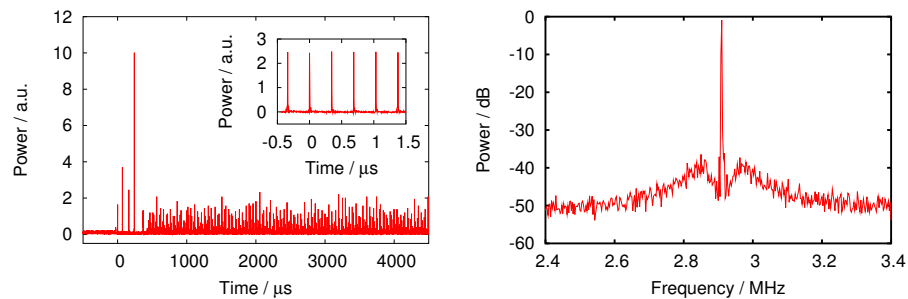


Figure 9.7: Left: Mode-locked startup from an initial Q-switched phase. Right: RF-spectrum of the mode-locked output around the fundamental frequency. The resolution BW was 1 kHz.

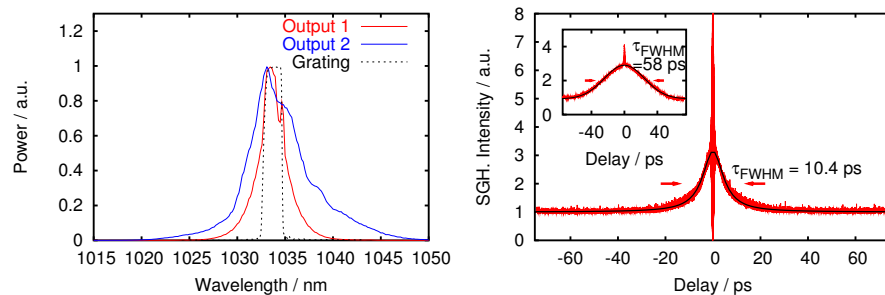


Figure 9.8: Left: Output spectra from the laser. Dotted line: measured reflectivity of the FBG. Right: Autocorrelation trace from the primary output, "Output 1". (Insert: autocorrelation trace from "Output 2")

ing and amplitude, but as soon as mode-locking is initiated, Q-switching ceases. This method of mode-locking differs from the well known Q-switched mode-locking [65], where a mode-locked pulse train is generated underneath the envelope of a Q-switched pulse. Figure 9.7 (left) shows the transition from Q-switched to mode-locked lasing. The mode-locked pulse train is not fully resolved due to sampling. The insert of figure 9.7 (left) shows the mode-locked pulse train on a shorter time scale. The repetition rate of the laser was 2.91 MHz.

Figure 9.8 (left) shows the output spectrum from the laser on a linear scale. The two outputs originate from the two arms of the 2x2 coupler, and the primary output, "Output 1" is the output which has the highest output power and shortest pulses. "Output 2" comes from the NPR fiber side of the cavity, and significant spectral broadening can be observed there from propagation in the NPR fiber. The laser mode-locks at a launched pump power in the interval 180-300 mW. At a pump power of 300 mW, the primary output power was 8.9 mW,

and the "Output 2" power was 0.8 mW. Both outputs were linearly polarized along the slow axis of the PM fiber pigtails. All data presented in this section were measured at a pump power of 300 mW. Figure 9.8 (left) also shows the measured reflectance from the FBG as a dotted line.

Figure 9.8 (right) shows the autocorrelation trace of the primary output. The autocorrelation FWHM of the non-oscillating part was 10.4 ps corresponding to an average pulse duration of 8.3 ps (using a deconvolution factor of 1.25 as found from the numerical calculations below (section 9.7)). The pulse stretches considerably during one round trip. The insert of figure 9.8 (right) shows the autocorrelation trace of the secondary output from the laser. The autocorrelation FWHM was 58 ps corresponding to an average pulse duration of 43 ps (deconvolution factor of 1.36). The laser contains ~ 34 m of fibers, and due to this long interaction length between fiber and pulse, the total non-linear phase shift accumulated during one round trip is so large that the pulse cannot reproduce itself every round trip. As a consequence the laser output is noise-like mode-locked, with a few percent fluctuations from pulse to pulse. In figure 9.7 (right) the RF spectrum around the fundamental laser frequency can be seen. The RF spectrum reveals a pedestal, which is typical for noise-like mode-locked lasers [139]. The pedestal is 38 dB below the peak. The relative energy fluctuations of the pulses was calculated from the measured RF-spectrum to 25 % [139]. In spite of noise-like mode-locking, the long term stability of the laser was excellent. The long term stability was tested over a period of 200 hours, by monitoring the average output power and no variation was observed. This was despite the fact, that the laser were simply freely lying in a cardboard box on a wooden table in a room with no temperature control, and hence the stability is significantly better than that of the solid state lasers in our lab, which require optical tables and stable temperatures.

9.6.1 Amplification and supercontinuum generation

To demonstrate the applicability of the laser, the primary output, "Output 1" was amplified in a simple single-mode non-PM fiber amplifier, and subsequently used for supercontinuum generation in a nonlinear photonic crystal fiber (PCF). Figure 9.6 also shows the diagram of the amplifier and the PCF. The gain fiber of the amplifier was a 20 cm long non-PM highly yb-doped fiber (i.e. ~ 1200 dB/m absorption at 976 nm). The yb-doped fiber was pumped through a non-PM fiber pigtailed WDM with a 600 mW single-mode fiber pigtailed 974 nm laser diode. The fiber pigtails on the WDM were kept as short as possible (i.e. < 20 cm). The nonlinear PCF (MFD ~ 3.3 μm) was 11.4 m long and was simply spliced to the amplifier (splice loss: ~ 48 %). The other end of the PCF was angle cleaved in order to suppress back reflection into the amplifier. Figure 9.9 (left) shows the output power from the amplifier vs. amplifier pump power before the PCF was spliced on. The maximum output power was 410 mW corresponding to a pulse energy of 141 nJ. Figure 9.9 (right) shows the amplified spectrum at three different amplifier pump powers on a logarithmic scale, and only slight spectral

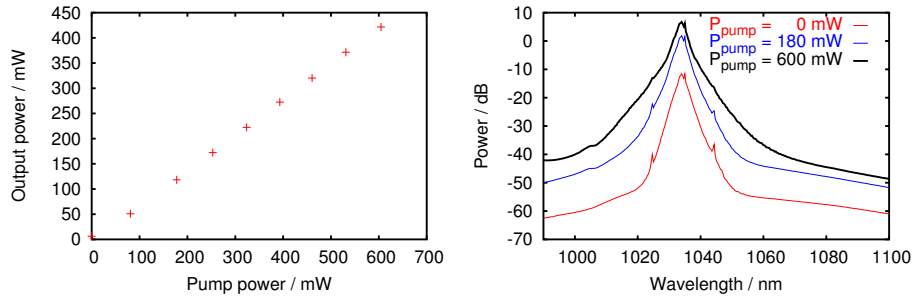


Figure 9.9: Left: Output power from the amplifier vs. amplifier pump power. Right: Amplified spectrum at three different amplifier pump powers.

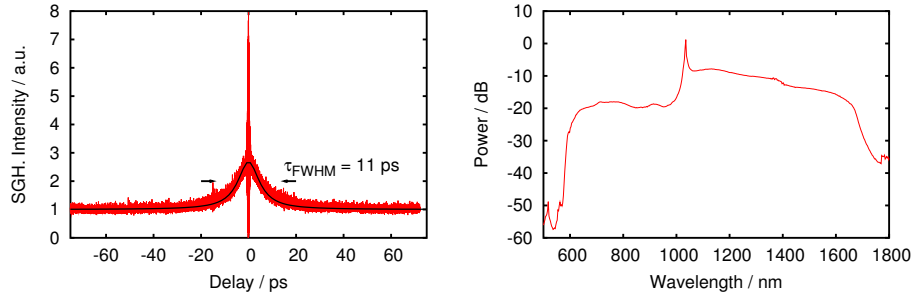


Figure 9.10: Left: Autocorrelation after maximum amplification of the primary output. The autocorrelation FWHM of the non-oscillating part is 11 ps corresponding to a pulse duration of 7.8 ps. Right: Supercontinuum generated after pulse propagation through a photonic crystal fiber.

broadening was observed.

Figure 9.10 (left) shows the measured autocorrelation trace after amplification. The pulse duration only increased slightly during amplification, and the autocorrelation FWHM of the non-oscillating part was 11.0 ps at maximum amplification corresponding to an average pulse duration of 8.8 ps. At maximum amplification the output power through the PCF was 213 mW. Figure 9.10 (right) shows the supercontinuum (SC) generated after pulse propagation through the PCF. The SC spans from 600 nm to 1750 nm. The noise from the laser also leads to noise in the SC, but averaging times of < 1 s were found to be sufficient for stable noise-free averaged spectra. For most linear applications of the SC (e.g. transmission measurements etc.) such averaging times are sufficiently short. The SC is generated through multi soliton generation and this form of SC generation is also associated with pulse to pulse fluctuations even if the input is more stable. In spite of the low average power of the SC compared to

the SC demonstrated in chapter 8, the SC source presented here is expected to be highly applicable in many fields, as it is based on a fully-spliced environmentally stable fiber laser system, based on readily available single-mode fiber components. Compared to other fiber laser sources, it is the low repetition rate from this laser that enables SC generation at the power levels obtainable after amplification with the use of standard single-mode fiber pigtailed laser diodes. SC generation can also be obtained at higher repetition rates if shorter femto-second pulses are used. However this requires more complicated amplification schemes with subsequent pulse compression before launching the pulse into the PCF. Alternatively pulse-picking can also be used.

9.7 Numerical model and simulations

An important component of the presented laser is the FBG. Besides working as a mirror, the FBG is also the primary source of pulse shaping, which is needed to obtain short pulses from the laser. Without this form of pulse shaping (i.e. if the FBG is replaced by a broadband mirror), much longer pulses (i.e. > 100 - 1000 ps) would be obtained from the laser. When working in the noise-like mode-locked regime, it is possible to use strong spectral filtration to attain temporal compression inside the cavity. As all the fibers in the cavity have high normal dispersion, and as no means of introducing anomalous dispersion are used, the pulses circulating inside the cavity are highly chirped. As a consequence, temporal compression can be obtained by spectral filtration. A numerical model of the laser was developed to further investigate the difference between temporal compression by spectral filtration and temporal compression by dispersion compensation, and to investigate dependence of different parameters.

The model is based on the operator algebra introduced in section 9.2 and on solving the NLSE in each fiber segment in succession. The laser is divided into three fiber segments: 0.65 m PM gain fiber and 4 m passive PM fiber between the FBG and the coupler, and 30 m nonlinear non-PM fiber between the coupler and the FM. NPR in between the coupler and the FM is handled in a similar way as in the calculations in section 9.2, except that the effect of the NPR operator, O_{NPR}^{CP} , is replaced by an integration of the NLSE for two coupled slowly varying fields in the CP representation (equations 2.28 and 2.29). The last two fiber segments are modeled by the standard NLSE for a single linear polarization state (equation 2.18). As no SRS was present in the output from the experimental laser, it is reasonable to neglect the Raman terms in the NLSE. Measured losses at intersections between different components are also included. The gain medium was modeled with an unsaturated peak gain coefficient of 25 dB/m and a Gaussian spectral gain profile with a bandwidth of 40 nm (FWHM). A coupling between light propagating in both directions through the gain medium was included through the gain average power saturation. The FBG was modeled by a super

Fiber type:	Gain	Passive	NPR
Length / m:	0.65	4	30
β_2 / ps ² /m:	0.023	0.023	0.046
β_3 / ps ³ /m:	$3.9 \cdot 10^{-5}$	$3.9 \cdot 10^{-5}$	$-9.6 \cdot 10^{-6}$
γ / (m W) ⁻¹ :	$6.7 \cdot 10^{-3}$	$3.6 \cdot 10^{-3}$	$14 \cdot 10^{-3}$
α / m ⁻¹ :	0	0	$2.07 \cdot 10^{-3}$

Table 9.1: Coefficients for the three different fibers used in the model of the laser.

Gaussian function to match the measured reflectivity of the FBG:

$$A(\omega) \rightarrow A(\omega) \cdot \exp \left(-2^{2.5} \ln(2) \left(\frac{\omega}{\omega_{\text{FWMN}}} \right)^{2.5} \right),$$

where the FWHM bandwidth, ω_{FWMN} , corresponds to a bandwidth of 2.0 nm. The other relevant coefficients used in the NLSE to model the three fibers can be seen in table 9.1.

Because of the strong pulse shaping from the strong spectral filtration, the simulations quickly converge from a long noise pulse to a regime where the monitored parameters fluctuate around stable values. No dependency was found on the choice of input pulse (non-noise pulses were also tested). Furthermore, dependency on the numerical resolution was also tested, and the number of data points was chosen sufficiently large to eliminate any dependence on the numerical resolution. At a saturation average power of $P_{\text{sat}} = 40$ mW, the calculated average output powers from the simulation matched the output powers from the experimental laser. Although the model is simplified compared to the real laser, and for instance does not include the unknown bend induced birefringence of the long NPR fiber, it does reproduce the experimental data qualitatively, and in agreement with the theory, the reflection, $|\vec{A}_{\text{out}}^{LP}|^2/|\vec{A}_{\text{in}}^{LP}|^2$, from NPR section tends to zero, as the input peak power is decreased. The pulse experiences both spectral and temporal broadening throughout the entire cavity and is only compressed (both spectrally and temporally) at the FBG. Figure 9.11 (left) shows the calculated averaged output spectra corresponding the the "Output 1" and "Output 2" spectra from the experimental laser. The spectra were averaged over 1000 round trips after the noise-like mode-locked regime was reached.

Figure 9.11 (right) shows the averaged output pulse temporal shapes, and figure 9.12 shows the averaged autocorrelation traces. The "Output 1" averaged pulse duration was 10.4 ps and the "Output 2" averaged pulse duration was 58 ps. The autocorrelation FWHM of the non-oscillating parts were 13.0 ps and 79 ps respectively, and hence the deconvolution factors between the autocorrelation FWHM and the averaged pulse duration FWHM for the two outputs are 1.25 and 1.36 respectively. Before calculating the averaged output pulse temporal shape, the midpoint of the temporal window was moved to the mean peak of the pulse. If this is not done, a spreading of the averaged pulse temporal shape would be observed due to drifting pulse position in the temporal

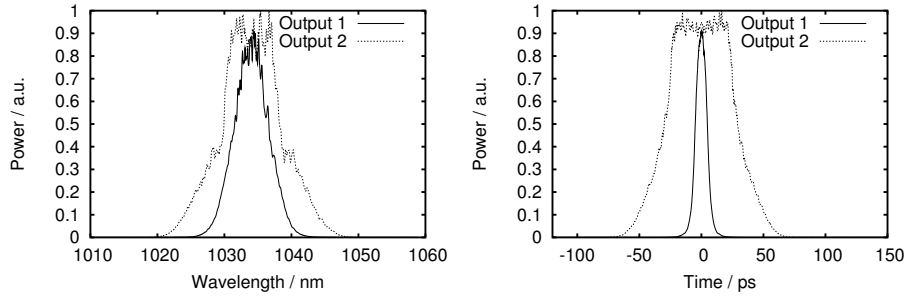


Figure 9.11: Left: Calculated averaged output spectra at output powers corresponding to the experimentally measured values. Right: Calculated averaged output temporal shapes.

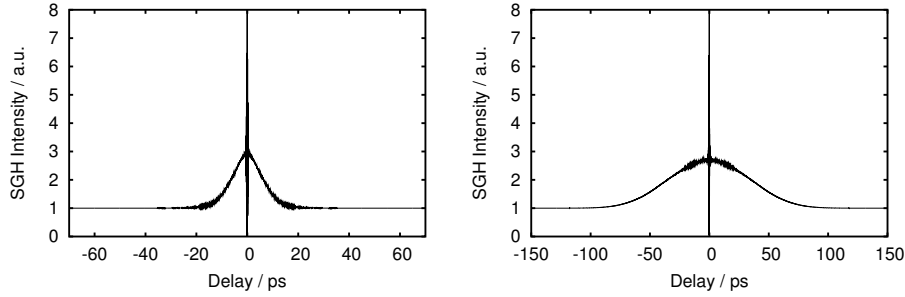


Figure 9.12: Calculated averaged autocorrelation trace of "Output 1" at output powers corresponding to the experimentally measured values. The autocorrelation FWHM of the non-oscillating part is 13.0 ps. Right: Calculated autocorrelation trace of "Output 2". The autocorrelation FWHM is 79.0 ps.

window. The averaged temporal pulse shape may, however, still be deceiving, as the pulse changes shape due to noise fluctuations. In the calculation of the averaged autocorrelation trace, the individual autocorrelation traces are however intrinsically centered due to the definition of the autocorrelation function, and hence the calculated averaged autocorrelation function gives a better picture of the true average pulse duration than the directly averaged temporal shape.

A significant temporal compression is observed in agreement with the experimentally measured pulse durations. To further investigate the importance of the FBG on the output pulse duration, a series of simulations were performed where the bandwidth of the FBG was varied while keeping all other parameters fixed. Figure 9.13 (left) shows the calculated "Output 1" autocorrelation FWHM vs. the FWHM bandwidth of the FBG. Short pulses directly out of the oscillator are a key issue for nonlinear applications, as the laser is noise-like mode-locked,

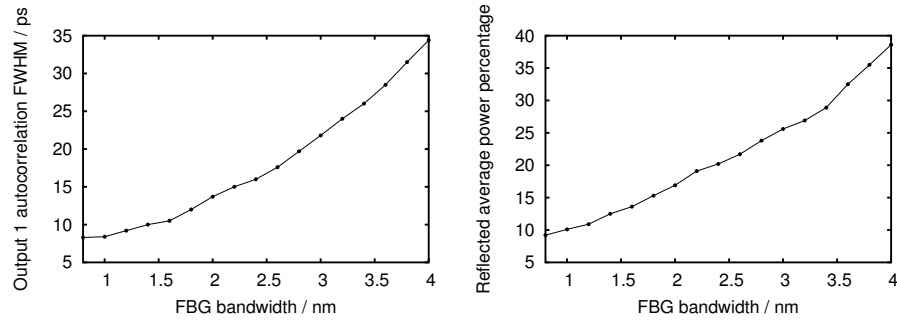


Figure 9.13: Left: "Output 1" autocorrelation FWHM vs. the FWHM bandwidth of the FBG. Right: Percentage of average power reflected of the FBG vs. the FWHM bandwidth of the FBG.

and as pulses from noise-like mode-locked lasers are in general not compressible due to the fluctuating phases from pulse to pulse. At increasing FBG bandwidths the pulse duration quickly increases, and to obtain as short pulses as possible, it is tempting to use as narrow FBG as possible. However, there is also a limit to how narrow a FBG one can use. When the bandwidth of the FBG is decreased, it slices out a smaller part of the spectrum, and this results in a shorter pulse, but a shorter pulse also results in a stronger spectral broadening during one round trip, and hence a smaller percentage of the power is reflected at the FBG. Figure 9.13 (right) shows the calculated percentage of the average power reflected of the FBG vs. the FWHM bandwidth of the FBG. In the simulations the competition between mode-locked lasing and self-Q-switched lasing is not included, but if the mode-locked mode experiences a too high loss in the real laser, self-Q-switched lasing will dominate.

In figure 9.14 (left), the "Output 1" autocorrelation FWHM can be seen as function of pump power, and in figure 9.14 (right) the corresponding "Output 1" averaged average power can be seen. The curve labeled "Spectral filtration" corresponds to the case of the FBG with a width of 2.0 nm. A very interesting property, which was also observed experimentally, when utilizing a FBG for temporal compression, is that the output pulse duration is constant over a wide range of pump powers. The reason for this is that a larger pump power causes a larger spectral and hence also temporal broadening during one round trip, but as the grating now slices out a smaller percentage of the spectrum, this results in an unchanged pulse duration. As with the limit in FBG bandwidth, the pump power can not just be increased unlimitedly, as the higher loss at the FBG makes mode-locked lasing less favourable compared to self-Q-switched lasing. Figure 9.15 (left) shows the calculated accumulated nonlinear phase shift during one round trip, and this can be seen to be substantially larger than π which is usually the limit of noise-free lasing.

Simulations were also performed where the FBG was replaced by an ele-

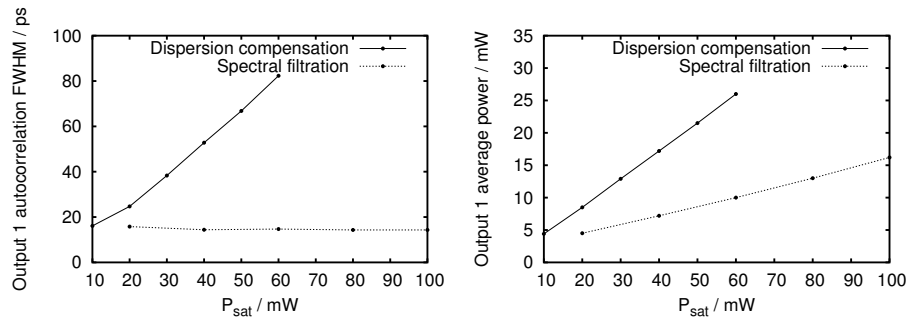


Figure 9.14: Left: "Output 1" autocorrelation FWHM vs. pump power represented by the gain saturation average power. "Spectral filtration" corresponds to simulations of a laser with an unchirped FBG with a bandwidth of 2.0 nm, and "Dispersion compensation" corresponds to a laser where the total dispersion of the cavity has been compensated by an element of infinite bandwidth. Right: "Output 1" averaged average power vs. pump power.

ment with infinite bandwidth, but with a total dispersion equal in magnitude but with opposite sign as that of the rest of the cavity. This was done in order to compare temporal compression inside the laser by use of strong spectral filtration with temporal compression by dispersion compensation. The calculations for the latter case are labeled "Dispersion compensation" in figures 9.14 and 9.15. Shorter pulses are in general obtainable by use of spectral filtration compared to dispersion compensation - even if lasers of comparable output powers are compared. The output pulse duration from dispersion compensated lasers increases linearly as the pump power is increased.

Figure 9.15 (right) shows the result of simulations where the length of the NPR fiber has been varied. Simulations of the laser with spectral filtration are conducted at a saturation average power of the gain medium of, $P_{\text{sat}} = 40 \text{ mW}$, and simulations of the laser with dispersion compensation with $P_{\text{sat}} = 20 \text{ mW}$. As can be seen in the figure, the output pulse duration decreases at decreasing cavity lengths. However, the property to optimize for nonlinear applications is the product between the repetition rate and the pulse duration - especially after external amplification to a specific average power level - as it is this product which determines the peak power of the amplified pulse. This product was however found to be virtually independent of the NPR fiber length, and hence substantial improvements to the experimentally obtained results are not expected to be possible with the available fiber components.

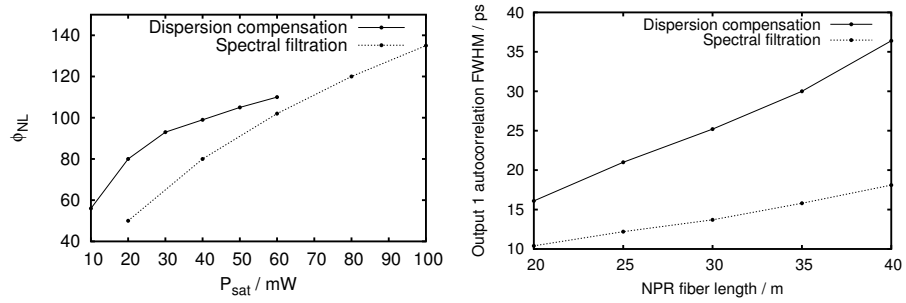


Figure 9.15: Left: Calculated nonlinear phase vs. pump power represented by the gain saturation average power. "Spectral filtration" corresponds to simulations of a laser with an unchirped FBG with a bandwidth of 2.0 nm, and "Dispersion compensation" corresponds to a laser where the total dispersion of the cavity have been compensated by an element of infinite bandwidth. Right: "Output 1" autocorrelation FWHM vs. NPR fiber length.

9.8 Intra cavity Raman continuum generation

To illustrate the limitations on the obtainable repetition rate set by Raman scattering, results of a second experimental implementation of the laser are presented here. Figure 9.16 shows a diagram of the laser.

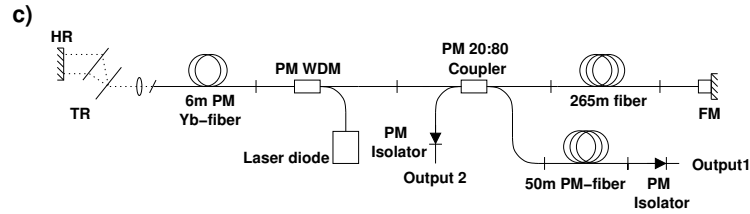


Figure 9.16: Diagrams of an experimental implemented laser with a repetition rate of 360 kHz. In this laser the NPR fiber was a 265 m non-PM fiber, and the length of the ytterbium doped fiber was 6 m. The FBG was replaced by a grating compressor. (HR: High Reflector, TR: Transmission Gratings, FM: Faraday Mirror).

In this laser the NPR fiber was a 265 m non-PM fiber with the same fiber characteristics as in the previous laser (figure 9.3). The length of the ytterbium doped fiber was increased to 6 m (but otherwise also with the same characteristics as before) in order to effectively move the gain band of the ytterbium fiber to higher wavelengths. This is possible as the last (unpumped) section of the ytterbium fiber exhibits a wavelength dependent absorption with higher absorption at lower wavelengths. When a long piece of ytterbium fiber is used, the 976 nm

isolator can be omitted. As a result of the longer yb-doped fiber, an extra length of 50 m PM fiber was needed on the "Output 1" side in order to have sufficient SBS and RB backscattering to start the laser. The FBG was in this laser replaced by a grating compressor. The double pass dispersion of the grating compressor was -2.7 ps^2 , and hence only a partial dispersion compensation ($\Delta\beta_2 = 22.1 \text{ ps}^2$) was obtained with this approach.

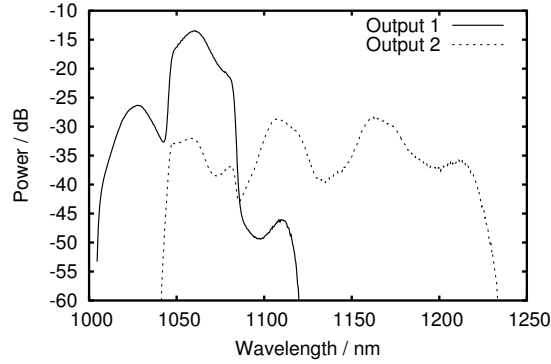


Figure 9.17: Output 1 and Output 2 spectra from the 360 kHz laser.

The repetition rate of this laser was 360 kHz, but the pulse duration was also long (i.e. $> 100 \text{ ps}$). The output spectra from the laser at a pump power of 300 mW can be seen in figure 9.17. The repetition rate and the obtainable output pulse duration was found to be limited by the onset of SRS, and in the "Output 2" spectrum coming from the NPR side of the cavity, the first three stokes pulses are clearly visible. The stokes pulses are generated inside the cavity, and hence correspond to a substantial loss to the mode-locked pulse. SRS is a nonlinear loss mechanism affecting only a pulse and not a low power cw mode, but because of the high modulation depth of the NPR fiber section, single pulse (noise-like) mode-locking was possible with this laser configuration. Due to the low repetition rate, this peak power was sufficient to generate a Raman spectrum with a width of 190 nm. Only the spectral part overlapping with the bandwidth of the gain medium and the grating compressor was amplified, and the rest simply filtered out every round trip, as can be seen from the "Output 1" spectrum. Hence the output only contained the fundamental pulse. Even though longer fiber lengths were also experimentally investigated, the 360 kHz repetition rate constitutes the experimentally found limit in single pulse (noise-like) mode-locking. At longer fiber lengths or at smaller net cavity dispersion the laser jumped into a multi pulse mode where two or more noise-like pulses were simultaneously present inside the cavity.

Although many different cavity configurations were experimentally investigated (i.e. different cavity lengths, different fiber types, different compression mechanisms and settings, etc.), short (i.e. sub 10 ps) pulses were only obtained

at higher repetition rates, as in the laser presented in section 9.5. The primary limitation to the output pulse duration is believed not to be set by SRS, but rather by the nature of noise-like pulse evolution inside long sections of fiber. Pulse durations in the 100 ps range are not really interesting, as shorter pulses are obtainable from fast laser diodes. The approach of using a long piece of yb-doped fiber to avoid the use of the 980 nm isolator was also found to be inadequate to obtain shortest possible pulses.

9.9 All-polarization maintaining fiber laser

Although the FM intrinsically compensates the linear polarization evolution inside the non-PM NPR fiber, and hence stabilizes NPR, NPR in non-PM fibers is still a function of the linear polarization state, and hence also of the linear polarization evolution inside the fiber. As a consequence, the laser outputs from the above mentioned lasers are susceptible to strong perturbations to the non-PM fiber. Although the laser is still much more stable compared to fiber lasers utilizing NPR in a fiber where the linear polarization evolution has not been compensated by a FM, it would be better if the total NPR could be made independent of the linear birefringence altogether. It was both experimentally and theoretically demonstrated in reference [140] that NPR, to a good approximation, is independent of the linear birefringence in highly birefringent fibers with a linear beat length much shorter than the nonlinear beat length.

A FM still has to be used to avoid problems with environmentally induced changes of the linear polarization evolution, but if the non-PM fiber in between the FM and the coupler is replaced by a PM fiber in which NPR can occur, the laser can be made environmentally stable even against strong perturbations of the fibers. When neglecting losses, dispersion and walk-off due to the group birefringence, NPR in a PM fiber is described by [1]:

$$\begin{aligned}\frac{\partial}{\partial z}A_x(t) &= +i\gamma(|A_x(t)|^2 + \frac{2}{3}|A_y(t)|^2)A_x(t) + \frac{i}{3}A_x(t)^*A_y(t)^2\exp(-2i\Delta\beta_0z) \\ \frac{\partial}{\partial z}A_y(t) &= +i\gamma\{(|A_y(t)|^2 + \frac{2}{3}|A_x(t)|^2)A_y(t) + \frac{i}{3}A_y(t)^*A_x(t)^2\exp(2i\Delta\beta_0z)\}.\end{aligned}\tag{9.1}$$

For NPR to occur, the polarization state must not be linearly polarized along one of the two birefringent axes, x and y . However, as the polarization state quickly evolves into elliptically polarized light at other input polarization directions, it is sufficient to launch linearly polarized light into the fiber with an angle between the polarization axis and the birefringent axes. This can easily be implemented experimentally in an all-fiber solution, by splicing two PM fibers together with an angle between the axes of the two fibers. Figure 9.18 shows the calculated reflection through a polarizer after NPR in a 30 m long PM fiber and reflection off a FM. The NPR fiber was modeled with nonlinear coefficient, $\gamma = 9.2 \cdot 10^{-3} \text{ (m W)}^{-1}$ and phase birefringence, $\Delta n = 10^{-4}$, corresponding

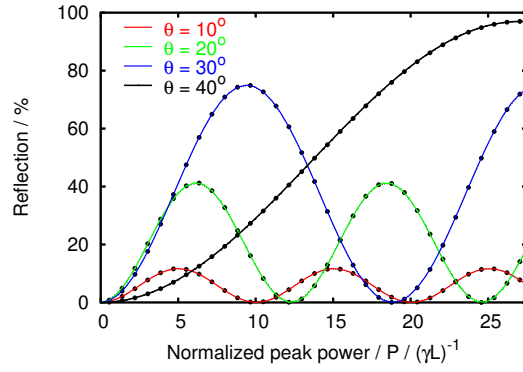


Figure 9.18: Calculated reflection through a polarizer after NPR in a PM fiber (parameters in the text). Reflection is calculated for different angles between the polarizer and the birefringent axis of the fiber on the input side, and at the other end the light is reflected at a FM. Solid and dashed lines represent calculations using equations 9.1, and filled circles represent calculations where the $\exp(\pm 2i\Delta\beta_0 z)$ terms in equations 9.1 have been neglected.

to $\Delta\beta_0 = 610 \text{ m}^{-1}$ (values are chosen to match the PM fiber used in the experiments below (section 9.9.1)). The reflection is calculated using equations 9.1 (solid and dashed lines) for different angles, θ , between the polarizer and the axis of the PM fiber.

Again the reflection initially increases from zero with increasing peak power. The highest reflection is obtained at angles closest to $\theta = 45^\circ$, but also requires a higher peak power. Compared to figure 9.2, higher peak powers corresponding to higher nonlinear phase shifts are also required to obtain maximum reflectivity.

As the $\exp(\pm 2i\Delta\beta_0 z)$ terms in equations 9.1 are very fast oscillating functions of z and hence on average effectively do not contribute to the NPR, they can to a very good approximation be neglected. The filled circles in figure 9.18 represent calculations where the $\exp(\pm 2i\Delta\beta_0 z)$ in equations 9.1 have been neglected, and as can be seen, the results are indistinguishable from the calculations where the $\exp(\pm 2i\Delta\beta_0 z)$ terms were not neglected. This approximation is the high-birefringence approximation of the NLSE leading to equations 2.30 and 2.31. As the environmentally induced changes to the birefringence of the fiber is contained in $\Delta\beta_0(z)$, the NPR is hence independent of environmentally induced changes to the birefringence when the $\exp(\pm 2i\Delta\beta_0 z)$ terms in equations 9.1 are negligible.

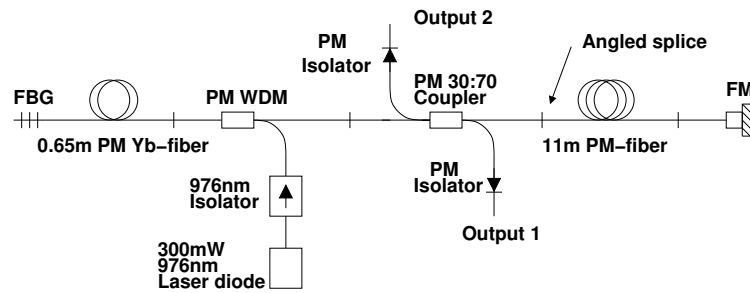


Figure 9.19: Diagram of the all-PM laser configuration.

9.9.1 Experimental setup and results

All-PM versions of the proposed laser configuration with NPR in a PM fiber have also been investigated experimentally. For the experiments a PM fiber with a MFD of $4.11 \mu\text{m}$, and an attenuation of 8 dB/km at 1060 nm was used. The group birefringence of the fiber was measured to: $n_g \sim 0.35 \cdot 10^{-4}$ at 1030 nm . This corresponds to a group velocity mismatch of 117 fs/m . The dispersion of the PM fiber was measured to $\beta_2 = 0.024 \text{ ps}^2/\text{m}$, $\beta_3 = 10.2 \cdot 10^{-6} \text{ ps}^3/\text{m}$ at 1030 nm . Short pulses (i.e. sub 10 ps) were only obtained at higher repetition rates compared to the version with NPR in a non-PM fiber. Here results from an 5.96 MHz version of an all-PM laser is presented. Figure 9.19 shows a diagram of the laser configuration. The laser was identical to the laser shown in figure 9.6, except that the 29 m long non-PM NPR fiber was replaced with an 11 m long PM fiber.

At an angle of $\theta \sim 30^\circ$ between the slow axis of the coupler (polarizer) and the slow axis of the PM fiber, and at a pump power of 300 mW , self-starting noise-like mode-locking was obtained. The pump power could be turned back down to $\sim 150 \text{ mW}$ before mode-locking ceased. The repetition rate of the laser was 5.96 MHz , and the "Output 1" and "Output 2" powers were 8.0 mW and 0.50 mW respectively. Figure 9.20 (left) shows the output spectra from the laser at a pump power of 300 mW on a linear scale (Insert: logarithmic scale). The FWHM spectral width was 1.17 nm and 1.87 nm of "Output 1" and "Output 2" respectively.

Figure 9.20 (right) shows the measured autocorrelation trace. The FWHM of the non-oscillating part of the autocorrelation trace was 7.0 ps , corresponding to an average pulse duration of 5.6 ps (deconvolution factor 1.25). The RF spectrum around the fundamental laser frequency can be seen in figure 9.21 (left). The pedestal was 38 dB below the peak. The calculated relative energy fluctuations were 6.1% , and hence less than the relative energy fluctuations from the 2.91 MHz laser with NPR in a non-PM fiber. The stability of the laser was also excellent, and the fibers (even the NPR fiber) could be moved around and bend strongly without any detectable change to the output power, pulse spectra or autocorrelation trace. The long term stability of the laser was also tested over

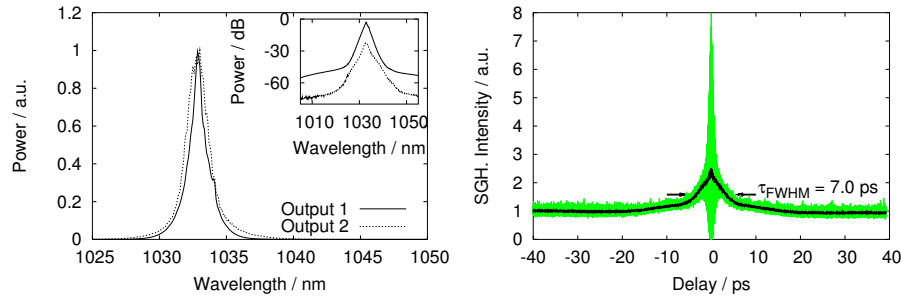


Figure 9.20: Left: Output spectrum from the all-PM laser at a pump power of 300 mW. Insert: logarithmic scale. Right: Autocorrelation trace of the "Output 1" pulse. The autocorrelation FWHM of the non-oscillating part was 7.0 ps.

a period of 200 hours. Figure 9.21 (right) shows the measured output power from the laser. The output power was measured with a setup with a very fast integration time, so that variations in the average output power due to pulse to pulse fluctuations can be seen. The standard deviation was 0.25 mW, and no long time variations in the average output power was observed. In spite of the quite large variations in the output power, the average value does hence not change on a long time scale. The insert of figure 9.21 (right) shows the measured output power over a time period of 2 s and with a sampling rate of 1 kHz. As can be seen, the fluctuations are very rapid, and can be easily averaged out over averaging times of ~ 1 s.

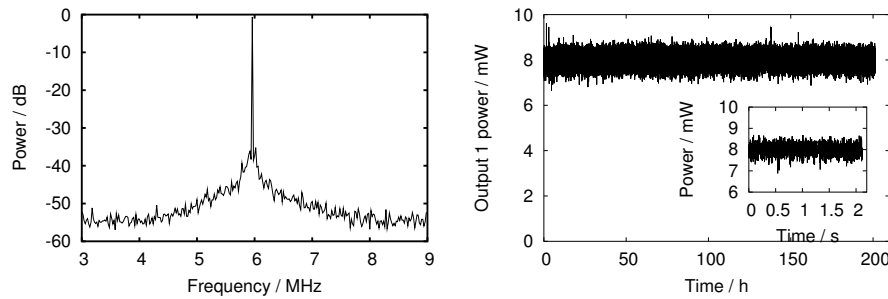


Figure 9.21: Left: RF-spectrum of the mode-locked output around the fundamental frequency at a pump power of 300 mW. The resolution BW was 1 kHz. Right: Long term output power stability measurement of the all-PM laser. The measurement shows quite large pulse to pulse fluctuations but a stable average power level. Insert: Output power on a short time scale measured with sampling rate of 1 kHz.

9.10 Summary

In summary, a new mode-locked laser configuration has been investigated theoretically and experimentally. The mode-locking mechanism is based on NPR, and environmentally stable low-repetition rate laser outputs are possible from lasers with no sections of free space optics. The mode-locked state is noise-like with pulse to pulse fluctuations. However, as there are no long term fluctuations, the outputs can easily be averaged. An alternative approach of using strong spectral filtration instead of dispersion compensation for intra cavity pulse shaping was investigated theoretically and experimentally. This approach resulted in the shortest pulses obtained from the proposed laser configuration. Highest environmental stability was obtained from an all-PM laser with NPR in a PM fiber. The laser is further demonstrated to be stable towards self-Q-switching of the gain medium (and in fact uses this mechanism to start-up), and optically fragile components like SESAMs and pump lasers can be omitted or isolated. As an application of the proposed laser configuration 213 mW of supercontinuum (600 nm to 1750 nm) was demonstrated from a fiber laser system with no sections of free-space optics.

9.11 Outlook

The proposed laser configuration with NPR between a FM and a polarizer is interesting as it is implementable as an all-fiber environmentally stable fiber laser. The combination of a FM and a polarizer, however, does not allow for noise-free mode-locking, as high feedbacks are only possible at nonlinear phase shifts beyond the noise-free limit. For applications where short term averaging is not a problem, but where the long term stability is important, this type of laser configuration may be a good solution. Furthermore, short (i.e. sub 10 ps) single pulsed lasing is possible from this type of configuration at repetition rates in the 1-6 MHz range, and this range is interesting for fast material processing. Low repetition rates are however also obtainable through pulse picking of noise-free lasers, but this requires more complicated and expensive setups, the proposed laser configuration may hence be a cheaper alternative for some applications. It is however believed, that the laser is best suited as a stable source for simple SC generation.

CHAPTER 10

Summary and perspectives

The focus of this thesis has been the development of new mode-locked fiber lasers and fiber laser systems. The recent development of photonic crystal fibers (PCF) has provided new fiber based products which are highly interesting for the development of such systems. The flexibility and design freedoms of PCFs enable interesting new possibilities compared to standard fibers. A main part of this work has been devoted to the investigation of different applications of such PCFs, and how they can contribute to the development of mode-locked fiber laser systems.

A primary requirement for the generation of femtosecond pulses from fiber laser systems operating near $1\ \mu\text{m}$ and with no sections of free space optics, is the availability of fiber based components with anomalous dispersion. In chapter 5 a fiber laser based on a solid-core photonic bandgap (SC-PBG) fiber for intra cavity dispersion compensation was demonstrated. SC-PBG fibers are highly integrable with standard fibers and can be spliced to these without introducing Fresnel reflections. The pulse duration was found to be limited by the high third order dispersion of the SC-PBG fiber. However, a pulse duration comparable to pulse durations obtainable from other fiber lasers with fiber based dispersion compensation was demonstrated. 158 fs pulses were obtained after external compression in a hollow core photonic bandgap (HC-PBG) fiber. HC-PBG fibers enables fiber based outputs and external compression without high nonlinear induced pulse distortions.

An alternative to the use of linear dispersive elements for intra cavity dispersion compensation was investigated in chapter 8. After external compression, 800 fs pulse durations were obtained from a fiber laser based on temporal com-

pression in a high modulation depth SESAM. More importantly, the laser was used for high average power blue-extended supercontinuum generation in a small core PCF after amplification in a setup with no dispersion compensation elements.

Within recent years, fiber laser systems have become a serious alternative to the classical solid-state laser systems. A major reason for this development is the development of high efficiency ytterbium based fiber amplifiers, which combined with high power laser diodes enables average power amplification even to the kW level. Ytterbium doped amplifiers with output power levels of 10-100 W combined with a mode-locked fiber laser seed source, provides competitive alternatives to other amplified mode-locked fiber laser systems. An important property of such systems is the stability towards changing conditions in the surrounding environment. Such changes can affect the output from mode-locked fiber lasers and the polarization evolution in amplifiers with the result of decreased throughput and pulse quality after final compression in grating compressors. In chapter 6, an environmentally stable mode-locked fiber laser was presented, and in chapter 7 amplification of this oscillator to the micro-Joule level was demonstrated in an environmentally stable setup. The setup was based on a single mode polarization maintaining (PM) standard fiber oscillator and a large core single mode double clad PM PCF amplifier.

A primary limitation to the generation of high pulse peak powers from fiber based systems is the high nonlinear phase shift accumulated by a pulse due to tight confinement and long interaction lengths in fibers. To reach the highest pulse energies without high pulse distortions in chapter 7, advantage of the special pulse output shape from the oscillator was taken, and this enabled nonlinear phase shifts above the nonlinear limit. The oscillator operated in the self-similar regime, and hence generated parabolic like pulses. Direct amplification of parabolic pulses was further investigated theoretically in chapter 7, and compared to self-similar amplifiers, this approach was found to have a higher theoretical limit of the obtainable pulse energy.

To utilize the full potential of fibers in fiber lasers, experimental implementations should be realized with no sections of free space optics. Prior to this work, intrinsically environmentally stable mode-locked fiber lasers with no sections of free space optics have only been demonstrated with the use of PM fibers and with a SESAM as the mode-locking mechanism. In chapter 9, an intrinsically environmentally stable mode-locked fiber laser with no sections of free space optics and based on nonlinear polarization rotation was demonstrated. As an application, super continuum generation from a stable source with no sections of free space optics was proposed and demonstrated.

The further development of fiber laser systems is also in the future expected to depend highly on the continued development of PCFs. Especially the development of double clad PCFs with larger cores will push the obtainable pulse energies and peak powers even further. On the integrability side, there is also a lot of work to be done in obtaining amplification to the highest power levels without sections of free space optics. As fiber laser systems with higher stability

are developed, the number of applications will also continue to increase, and in the future, mode-locked fiber lasers will perhaps find applications on much broader commercial markets. In the near future, it is likely that the realization of commercial high average power supercontinuum sources will have a high impact on areas such as e.g. microscopy and spectroscopy in fields of medicine, biology and chemistry, and hence bring applications of mode-locked fiber laser out of the optical laboratories.

Bibliography

- [1] G. P. Agrawal. *Nonlinear Fiber Optics*. Academic Press, San Diego, CA. (1995).
- [2] C. L. Thomsen, D. Madsen, S. R. Keiding, J. Thøgersen, and O. Christiansen. "Two-photon dissociation and ionization of liquid water studied by femtosecond transient absorption spectroscopy". *J. Chem. Phys.*, **110**, no. 7, pp. 3453–3462 (1999).
- [3] T. Udem, R. Holzwarth, and T. W. Hänsch. "Optical frequency metrology". *Nature*, **416**, pp. 233–237 (2002).
- [4] P. U. Jepsen, R. H. Jacobsen, and S. R. Keiding. "Generation and detection of terahertz pulses from biased semiconductor antennas". *J. Opt. Soc. Am. B*, **13**, no. 11, pp. 2424–2436 (1996).
- [5] H. N. Paulsen, K. M. Hilligsøe, J. Thøgersen, S. R. Keiding, and J. J. Larsen. "Coherent anti-Stokes Raman scattering microscopy with a photonic crystal fiber based light source". *Opt. Lett.*, **28**, no. 13, pp. 1123–1125 (2003).
- [6] I. Hartl, X. D. Li, C. Chudoba, R. K. Ghanta, T. H. Ko, J. G. Fujimoto, J. K. Ranka, and R. S. Windeler. "Ultrahigh resolution optical coherence tomography using continuum generation in a air-silica microstructure optical fiber". *Opt. Lett.*, **26**, no. 9, pp. 608–610 (2001).
- [7] P. Weigl, A. Kasenbacher, and K. Werelius. "Dental applications". *Top. App. Phys.*, **96**, pp. 167–185 (2004).
- [8] A. Tünnermann, J. Limpert, and S. Nolte. "Ultrashort pulse fiber lasers and amplifiers". *Top. App. Phys.*, **96**, pp. 35–53 (2004).
- [9] D. Breitling, C. Föhl, F. Dausinger, T. Kononenko, and V. Konov. "Drilling of metals". *Top. App. Phys.*, **96**, pp. 131–154 (2004).
- [10] H. A. Haus. "Mode-Locking of Lasers". *IEEE J. Selected Top. in Quantum Electron.*, **6**, no. 6, pp. 1173–1185 (2000).

- [11] M. E. Fermann, A. Galvanauskas, G. Sucha, and D. Harter. "Fiber-lasers for ultrafast optics". *Appl. Phys. B*, **65**, no. 2, pp. 259–275 (1997).
- [12] L. E. Nelson, D. J. Jones, K. Tamura, H. A. Haus, and E. P. Ippen. "Ultrashort-pulse fiber ring lasers". *Appl. Phys. B*, **65**, no. 2, pp. 277–294 (1997).
- [13] A. Tünnermann, T. Schreiber, F. Röser, A. Liem, S. Höfer, H. Zellmer, S. Nolte, and J. Limpert. "The renaissance and bright future of fibre lasers". *J. Phys. B*, **38**, no. 9, pp. 681–693 (2005).
- [14] J. Limpert, F. Röser, T. Schreiber, and A. Tünnermann. "High-Power Ultrafast Fiber Laser Systems". *IEEE J. Selected Top. in Quantum Electron.*, **12**, no. 2, pp. 233–244 (2006).
- [15] (<http://www.imra.com>).
- [16] (<http://www.fianium.com>).
- [17] J. C. Knight, T. A. Birks, P. S. J. Russell, and D. M. Atkin. "All-silica single-mode optical fiber with photonic crystal cladding". *Opt. Lett.*, **21**, no. 19, pp. 1547–1549 (1996).
- [18] J. C. Knight, J. Broeng, T. A. Birks, and P. S. J. Russell. "Photonic Band Gap Guidance in Optical Fibers". *Science*, **282**, no. 5393, pp. 1476–1478 (1998).
- [19] L. F. Mollenauer, R. H. Stolen, and M. N. Islam. "Experimental Observation of Picosecond Pulse Narrowing and Solitons in Optical Fibers". *Phys. Rev. Lett.*, **45**, no. 13, pp. 1095–1097 (1980).
- [20] T. R. Taha and M. I. Albowitz. "Analytical and numerical aspects of certain nonlinear evolution equations. II. Numerical, nonlinear Schrödinger equation". *Journal of Comp. Phys.*, **55**, no. 2, pp. 203–230 (1984).
- [21] N. Yajima, M. Oikawa, J. Satsuma, and C. Namba. "Modulated Langmiur waves and nonlinear landau damping". *Rep. Res. Inst. Appl. Mech.*, , no. 70 (1975).
- [22] K. E. Strecker, G. B. Patridge, A. G. Truscott, and R. G. Hulet. "Formation and propagation of matter-wave soliton trains". *Nature*, **417**, no. 6885, pp. 150–153 (2002).
- [23] J. Limpert, T. Schreiber, T. Clausnitzer, K. Zöllner, H.-J. Fuchs, E.-B. Kley, H. Zellmer, and A. Tünnermann. "High-power femtosecond Yb-doped fiber amplifier". *Opt. Express*, **10**, no. 14, pp. 628–638 (2002).
- [24] F. O. Ilday, J. R. Buckley, and F. W. Wise. "Self-Similar Evolution of Parabolic Pulses in a Laser". *Phys. Rev. Lett.*, **92**, no. 213902 (2004).

- [25] T. G. and K. A. Shore, M. P. Soerensen, P. L. Christiansen, J. Mørk, and J. Mark. "Nonlinear fiber external cavity mode locking of erbium-doped fiber lasers". *J. Opt. Soc. Am. B*, **10**, no. 7, pp. 1166–1174 (1993).
- [26] S. Coen, A. H. L. Chan, R. Leonhardt, J. D. Harvey, J. C. Knight, W. J. Wadsworth, and P. S. J. Russell. "White-light supercontinuum generation with 60-ps pump pulses in a photonic crystal fiber". *Opt. Lett.*, **26**, no. 17, pp. 1356–1358 (2001).
- [27] S. Coen, A. H. L. Chan, R. Leonhardt, J. D. Harvey, J. C. Knight, W. J. Wadsworth, and P. S. J. Russell. "Supercontinuum generation by stimulated Raman scattering and parametric four-wave mixing in photonic crystal fibers". *J. Opt. Soc. Am. B*, **19**, no. 4, pp. 753–764 (2002).
- [28] K. M. Hilligsøe, H. N. Paulsen, J. Thøgersen, S. R. Keiding, and J. J. Larsen. "Initial steps of supercontinuum generation in photonic crystal fibers". *J. Opt. Soc. Am. B*, **20**, no. 9, pp. 1887–1893 (2003).
- [29] A. V. Husakou and J. Herrmann. "Supercontinuum generation of higher-order solitons by fission in photonic crystal fibers". *Phys. Rev. Lett.*, **87**, no. 203901 (2001).
- [30] J. M. Dudley, G. Genty, and S. Coen. "Supercontinuum generation in photonic crystal fiber". *Rev. Mod. Phys.*, **78**, no. 4, pp. 1135–1184 (2006).
- [31] P. V. Mamyshev and S. V. Chernikov. "Ultrashort-pulse propagation in optical fibers". *Opt. Lett.*, **15**, no. 19, pp. 1076–1078 (1990).
- [32] M. E. Fermann, V. I. Kruglov, B. C. Thomsen, J. M. Dudley, and J. D. Harvey. "Self-Similar Propagation and Amplification of Parabolic Pulses in Optical Fibers". *Phys. Rev. Lett.*, **84**, no. 26, pp. 6010–6013 (2000).
- [33] R. Boyd. *Nonlinear Optics*. Academic Press (1992).
- [34] E. R. Andresen, V. Birkedal, J. Thøgersen, and S. R. Keiding. "Tunable light source for coherent anti-Stokes Raman scattering microspectroscopy based on the soliton self-frequency shift". *Opt. Lett.*, **31**, no. 9, pp. 1328–1330 (2006).
- [35] S. Wabnitz, E. M. Wright, and G. I. Stegeman. "Polarization instabilities of dark and bright coupled solitary waves in birefringent optical fibers." *Phys. Rev. A*, **41**, no. 11, pp. 6415–6423 (1990).
- [36] B. A. Malomed and R. S. Tasgal. "The Raman effect and solitons in an elliptical optical fiber." *J. Nonlinear Opt. Phys. and Materials*, **5**, no. 3, pp. 559–574 (1996).
- [37] S. Wabnitz, S. Trillo, E. M. Wright, and G. I. Stegeman. "Wavelength-dependent soliton self-routing in birefringent fiber filters." *J. Opt. Soc. Am. B*, **8**, no. 3, pp. 602–613 (1991).

- [38] C. C. Yang and A. J. S. Wang. "Cross-polarization cross-phase modulation of femtosecond pulses in erbium-doped fiber amplifiers." *J. Opt. Soc. Am. B*, **9**, no. 5, pp. 682–686 (1992).
- [39] Q. Lin and G. P. Agrawal. "Vector theory of stimulated Raman scattering and its application to fiber-based Raman amplifiers." *J. Opt. Soc. Am. B*, **20**, no. 8, pp. 1616–1630 (2003).
- [40] C. R. Menyuk, M. N. Islam, and J. P. Gordon. "Raman effect in birefringent optical fibers." *Opt. Lett.*, **16**, no. 8, pp. 566–568 (1991).
- [41] R. Hellwarth, J. Cherlow, and T.-T. Yang. "Origin and frequency dependence of nonlinear optical susceptibilities of glasses." *Phys. Rev. B*, **11**, no. 2, pp. 964–967 (1975).
- [42] H. A. Haus, E. P. Ippen, and K. Tamura. "Additive-Pulse Modelocking in Fiber Lasers". *IEEE J. Quantum Electron.*, **30**, no. 1, pp. 200–208 (1994).
- [43] H. A. Haus. "Theory of mode locking with a fast saturable absorber". *J. App Phys.*, **46**, no. 7, pp. 3049–3058 (1975).
- [44] H. A. Haus, J. G. Fujimoto, and E. P. Ippen. "Structures for additive pulse mode locking". *J. Opt. Soc. Am. B*, **8**, no. 10, pp. 2068–2076 (1991).
- [45] H. A. Haus, J. G. Fujimoto, and E. P. Ippen. "Analytic Theory of Additive Pulse and Kerr Lens Mode Locking". *IEEE J. Quantum Electron.*, **28**, no. 10, pp. 2086–2096 (1992).
- [46] H. A. Haus, K. Tamura, L. E. Nelson, and E. P. Ippen. "Stretched-Pulse Additive Pulse Mode-Locking in Fiber Ring Lasers: Theory and Experiment". *IEEE J. Quantum Electron.*, **31**, no. 3, pp. 591–598 (1995).
- [47] N. A. Brilliant, R. J. Beach, A. D. Drobshoff, and S. A. Payne. "Narrow-line ytterbium fiber master-oscillator power amplifier". *J. Opt. Soc. Am. B*, **19**, no. 5, pp. 981–991 (2002).
- [48] A. A. Hardy and R. Oron. "Amplified Spontaneous Emission and Rayleigh Backscattering in Strongly Pumped Fiber Amplifiers". *J. Light. Tech.*, **16**, no. 10, pp. 1865–1873 (1998).
- [49] P. W. Milonni and J. H. Eberly. *Lasers*. Academic Press (1988).
- [50] A. Ghatak and K. Thyagarajan. *Introduction to Fiber Optics*. Academic Press (2000).
- [51] H. M. Pask, R. J. Arman, D. C. Hanna, A. C. Tropper, C. J. Mackechnie, P. R. Barber, and J. M. Dawes. "Ytterbium-Doped Silica Fiber Lasers: Versatile Sources for the 1-1.2 μm Region". *IEEE J. Selected Top. in Quantum Electron.*, **1**, no. 1, pp. 2–13 (1995).

- [52] E. Desurvire and J. R. Simpson. "Amplification of Spontaneous Emission in Erbium-Doped Single-Mode Fibers". *J. Light. Tech.*, **7**, no. 5, pp. 835–845 (1998).
- [53] F. O. Ilday, H. Lim, J. R. Buckley, and F. W. Wise. "Practical all-fiber source of high-power, 120-fs pulses at 1 μm ". *Opt. Lett.*, **28**, no. 15, pp. 1362–1364 (2003).
- [54] F. O. Ilday, J. R. Buckley, L. Kuznetsova, and F. W. Wise. "Generation of 36-femtosecond pulses from a ytterbium fiber laser." *Opt. Express*, **11**, no. 26, pp. 3550–3554 (2003).
- [55] K. Tamura, E. P. Ippen, H. A. Haus, and L. E. Nelson. "77-fs pulse generation from a stretched-pulse mode-locked all-fiber ring laser". *Opt. Lett.*, **18**, no. 13, pp. 1080–1082 (1993).
- [56] F. O. Ilday, J. R. Buckley, H. Lim, F. W. Wise, and W. G. Clark. "Generation of 50-fs, 5-nJ pulses at 1.03 μm from a wave-breaking-free fiber laser". *Opt. Lett.*, **28**, no. 15, pp. 1365–1367 (2003).
- [57] J. Buckley, F. O. Ilday, F. W. Wise, and T. Sosnowski. "Femtosecond fiber lasers with pulse energies above 10 nJ". *Opt. Lett.*, **30**, no. 14, pp. 1888–1890 (2005).
- [58] M. E. Fermann, L.-M. Yang, M. L. Stock, and M. J. Andrejco. "Environmentally stable Kerr-type mode-locked erbium fiber laser producing 360-fs pulses". *Opt. Lett.*, **19**, no. 1, pp. 43–45 (1994).
- [59] M. Hofer, M. E. Fermann, F. Haberl, M. H. Ober, and A. J. Schmidt. "Mode-locking with cross-phase and self-phase modulation". *Opt. Lett.*, **16**, no. 7, pp. 502–504 (1991).
- [60] (<http://www.batop.de>).
- [61] D. terverner. "Polarization maintaining figure-8 laser". *Optical Society of America Topical Meeting on non-linear guided wave phenomena, Cambridge*, , no. WC No.3 (1993).
- [62] F. O. Ilday, F. W. Wise, and T. Sosnowski. "High-energy femtosecond stretched-pulse fiber laser with a nonlinear loop mirror". *Opt. Lett.*, **27**, no. 17 (2002).
- [63] J. L. Proctor and J. N. Kutz. "Passive mode-locking by use of waveguide arrays". *Opt. Lett.*, **30**, no. 15, pp. 2013–2015 (2005).
- [64] M. Guina, N. Xiang, A. Vainionpää, O. G. Okhotnikov, T. Sajavaara, and J. Keinonen. "Self-starting stretched-pulse fiber laser mode locked and stabilized with slow and fast semiconductor saturable absorbers". *Opt. Lett.*, **26**, no. 22, pp. 1809–1811 (2001).

- [65] U. Keller, K. J. Weingarten, F. X. Kärtner, D. Kopf, B. Braun, I. D. Jung, R. Fluck, C. Hönninger, N. Matuschek, and J. A. der Au. "Semiconductor Saturable Absorber Mirrors (SESAM's) for Femtosecond and Nanosecond Pulse Generation in Solid-State Lasers". *IEEE J. Selected Top. in Quantum Electron.*, **2**, no. 3, pp. 435–445 (1996).
- [66] L. R. Brovelli and U. Keller. "Design and operation of antiresonant Fabry-Perot saturable semiconductor absorbers for mode-locked solid-state lasers". *J. Opt. Soc. Am. B*, **12**, no. 2, pp. 311–322 (1995).
- [67] F. X. Kärtner, J. A. der Au, and U. Keller. "Mode-Locking with Slow and Fast Saturable Absorbers - What's the Difference?" *IEEE J. Selected Top. in Quantum Electron.*, **4**, no. 2, pp. 159–168 (1998).
- [68] C. Hönninger, R. Paschotta, F. Morier-Genoud, M. Moser, and U. Keller. "Q-switching stability limits of continuous-wave passive mode locking". *J. Opt. Soc. Am. B*, **16**, no. 1, pp. 46–56 (1999).
- [69] M. Jiang, G. Sucha, M. E. Fermann, J. Jimenez, D. Harter, M. Dagenais, S. Fox, and Y. Hu. "Nonlinearly limited saturable-absorber mode locking of an erbium fiber laser". *Opt. Lett.*, **24**, no. 15, pp. 1074–1076 (1999).
- [70] M. L. Dennis and I. N. D. III. "Experimental Study of Sideband Generation in Femtosecond Fiber Lasers". *IEEE J. Quantum Electron.*, **30**, no. 6, pp. 1469–1477 (1994).
- [71] (<http://www.exfo.com>).
- [72] D. Ouzounov, D. Homoelle, W. Zipfel, W. W. Webb, A. L. Gaeta, J. A. West, J. C. Fajardo, and K. W. Koch. "Dispersion measurements of microstructured fibers using femtosecond laser pulses". *Opt. Commun.*, **192**, no. 3-6, pp. 219–223 (2001).
- [73] S. Diddams and J.-C. Diels. "Dispersion measurements with white-light interferometry". *J. Opt. Soc. Am. B*, **13**, no. 6, pp. 1120–1129 (1996).
- [74] D. Müller, J. West, and K. Koch. "Interferometric Chromatic Dispersion Measurement of a Photonic Band-gap Fiber". *Proceedings of Spie, Active and Passive Optical Components for WDM Communications II*, , no. 4870, p. 395 (2002).
- [75] (<http://www.koheras.com/Menu/Products/Ultra+Wide+Band>).
- [76] (<http://www.corning.com/photonicmaterials/pdf/pi1446.pdf>).
- [77] (<http://www.corning.com/photonicmaterials/pdf/pi1441.pdf>).
- [78] J. K. Ranka, A. L. Gaeta, A. Baltuska, M. S. Pshenichnikov, and D. A. Wiersma. "Autocorrelation measurement of 6-fs pulses based on the two-photon-induced photocurrent in a GaAsP photodiode". *Opt. Lett.*, **22**, no. 17, pp. 1344–1346 (1997).

- [79] M. J. Steel. "Symmetry and degeneracy in microstructured optical fibers". *Opt. Lett.*, **26**, no. 8, pp. 488–490 (2001).
- [80] J. Noda, K. Okamoto, and Y. Sasaki. "Polarization-Maintaining Fibers and Their Applications". *IEEE Photon. Technol. Lett.*, **4**, no. 8, pp. 1071–1089 (1986).
- [81] A. Ortigosa-Blanch, J. C. Knight, W. J. Wadsworth, J. Arriaga, B. J. Mangin, T. A. Birks, and P. S. J. Russell. "Highly birefringent photonic crystal fibers". *IEEE Photon. Technol. Lett.*, **25**, no. 18, pp. 1325–1327 (2000).
- [82] J. R. Folkenberg, M. D. Nielsen, N. A. Mortensen, C. Jakobsen, and H. R. Simonsen. "Polarization maintaining large mode area photonic crystal fiber". *Opt. Express*, **12**, no. 5, pp. 956–960 (2004).
- [83] M. Hofer, M. H. Ober, R. Hofer, G. S. M. E. Fermann, D. Harter, K. Sugden, I. Bennion, C. A. C. Mendonca, and T. H. Chiu. "High-power neodymium soliton fiber laser that uses a chirped fiber grating". *Opt. Lett.*, **20**, no. 16, pp. 1701–1703 (1995).
- [84] I. Hartl, G. Imeshev, L. Dong, G. C. Cho, and M. E. Fermann. "Ultra-compact dispersion compensated femtosecond fiber oscillators and amplifiers". *CLEO, Baltimore*, , no. CThG1 (2005).
- [85] A. Argyros, T. A. Birks, S. G. Leon-Saval, C. M. B. Cordeiro, F. Luan, and P. S. J. Russell. "Photonic bandgap with an index step of one percent". *Opt. Express*, **13**, no. 7, pp. 309–313 (2005).
- [86] G. Bouwmans, L. Bigot, Y. Quiquempois, F. Lopez, L. Provino, and M. Douay. "Fabrication and characterization of an all-solid 2D photonic bandgap fiber with a low-loss region (≤ 20 dB/km) around 1550 nm". *Opt. Express*, **13**, no. 21, pp. 8452–8459 (2005).
- [87] H. Lim, F. O. Ilday, and F. W. Wise. "Femtosecond ytterbium fiber laser with photonic crystal fiber for dispersion control". *Opt. Express*, **10**, no. 25, pp. 1497–1502 (2002).
- [88] H. Lim and F. W. Wise. "Control of dispersion in a femtosecond ytterbium laser by use of hollow-core photonic bandgap fiber". *Opt. Express*, **12**, no. 10, pp. 2231–2235 (2004).
- [89] J. Limpert, T. Schreiber, S. Nolte, H. Zellmer, and A. Tünnermann. "All fiber chirped-pulse amplification system based on compression in air-guiding photonic bandgap fiber". *Opt. Express*, **11**, no. 24, pp. 3332–3337 (2003).
- [90] C. J. S. de Matos, J. R. Taylor, K. P. H. T. P. Hansen, and J. Broeng. "All-fiber chirped pulse amplification using highly-dispersive air-core photonic bandgap fiber". *Opt. Express*, **11**, no. 22, pp. 2832–2837 (2003).

- [91] A. Isomäki and O. G. Okhotnikov. "All-fiber ytterbium soliton mode-locked laser with dispersion control by solid-core photonic bandgap fiber". *Opt. Express*, **14**, no. 10, pp. 4368–4373 (2006).
- [92] S. Zhou, L. Kuznetsova, A. Chong, and F. W. Wise. "Compensation of nonlinear phase shifts with third-order dispersion in short-pulse fiber amplifiers". *Opt. Express*, **13**, no. 13, pp. 4869–4874 (2005).
- [93] V. I. Kruglov, A. C. Peacock, and J. D. Harvey. "Self-similar propagation of parabolic pulses in normal-dispersion fiber amplifiers". *J. Opt. Soc. Am. B*, **19**, no. 3, pp. 461–469 (2002).
- [94] D. Anderson, M. Desaix, M. Karlsson, M. Lisak, and M. L. Quiroga-Teixeiro. "Wave-breaking-free pulses in nonlinear-optical fibers". *J. Opt. Soc. Am. B*, **10**, no. 7, pp. 1185–1190 (1993).
- [95] C. Finot, F. Parmigiani, P. Petropoulos, and D. J. Richardson. "Parabolic pulse evolution in normally dispersive fiber amplifiers preceding the similariton formation regime". *Opt. Express*, **14**, no. 8, pp. 3161–3170 (2006).
- [96] I. N. Duling. "Subpicosecond all-fiber Erbium laser". *Electr. Lett.*, **27**, no. 6, pp. 544–545 (1991).
- [97] K. Tamura, C. R. Doerr, L. E. Nelson, H. A. Haus, and E. P. Ippen. "Technique for obtaining high-energy ultrashort pulses from an additive-pulse mode-locked erbium-doped fiber ring laser". *Opt. Lett.*, **19**, no. 1, pp. 46–48 (1994).
- [98] M. Hofer, M. E. Fermann, and L. Goldberg. "High power side-pumped passively mode-locked Er-Yb fiber laser". *IEEE Photon. Technol. Lett.*, **10**, no. 9, pp. 1247–1249 (1998).
- [99] L. Lefort, J. H. V. Price, D. J. Richardson, G. J. Spühler, R. Pashotta, U. Keller, A. R. Fry, and J. Weston. "Practical low-noise stretched-pulse Yb³⁺-doped fiber laser". *Opt. Lett.*, **27**, no. 5, pp. 291–293 (2002).
- [100] B. Ortaç, A. Hideur, T. Chartier, M. Brunel, C. Özkul, and F. Sanchez. "90 fs generation from a stretched-pulse ytterbium doped fiber laser". *Opt. Lett.*, **28**, no. 15, pp. 1305–1308 (2003).
- [101] H. Lim, A. Chong, and F. W. Wise. "Environmentally-stable femtosecond ytterbium fiber laser with birefringent photonic bandgap fiber". *Opt. Express*, **13**, no. 9, pp. 3460–3464 (2005).
- [102] T. Clausnitzer, J. Limpert, K. Zöllner, H. Zellmer, H.-J. Fuchs, E.-B. Kley, A. Tünnermann, M. Jupé, and D. Ristau. "Highly efficient transmission gratings in fused silica for chirped-pulse amplification systems". *App. Opt.*, **42**, no. 34, pp. 6934–6938 (2003).

- [103] R. Davey, N. Langford, and A. Ferguson. "Interacting solutions in erbium fibre laser". *Electr. Lett.*, **27**, no. 14, pp. 1251–1259 (1991).
- [104] D. Richardson, R. Laming, D. Payne, V. Matsas, and N. Phillips. "Pulse repetition rates in passive, self starting, femtosecond soliton fibre laser". *Electr. Lett.*, **27**, no. 16, pp. 1451–1453 (1991).
- [105] J. Limpert, A. Liem, M. Reich, T. Schreiber, S. Nolte, H. Zellmer, A. Tünnermann, J. Broeng, A. Petersson, , and C. Jakobsen. "Low-nonlinearity single-transverse-mode ytterbium-doped photonic crystal fiber amplifier". *Opt. Express*, **12**, no. 7, pp. 1313–1319 (2004).
- [106] J. Limpert, N. Deguil-Robin, I. Manek-Hönninger, F. Salin, F. Röser, A. Liem, T. Schreiber, S. Nolte, H. Zellmer, A. Tünnermann, J. Broeng, A. Petersson, and C. Jakobsen. "High-power rod-type photonic crystal fiber laser". *Opt. Express*, **13**, no. 4, pp. 1055–1058 (2005).
- [107] K. Aiso, Y. Tashiro, T. Suzuki, and Yagi. "Development of Er/Yb Co-doped Fiber for High-Power Optical Amplifiers". *Furukawa Review*, , no. 20, pp. 41–45 (2001).
- [108] T. A. Birks, J. C. Night, and P. S. J. Russel. "Endlessly single-mode photonic crystal fiber". *Opt. Lett.*, **22**, no. 13, pp. 961–963 (1997).
- [109] G. Chang, A. Galvanauskas, H. G. Winful, and T. B. Norris. "Dependence of parabolic pulse amplification on stimulated Raman scattering and gain bandwidth". *Opt. Lett.*, **29**, no. 22, pp. 2647–2649 (2004).
- [110] T. Schreiber, F. Röser, O. Schmidt, J. Limpert, R. Iliew, F. Lederer, A. Petersson, C. Jakobsen, K. P. Hansen, J. Broeng, and A. Tünnermann. "Stress-induced single-polarization single-transverse mode photonic crystal fiber with low nonlinearity". *Opt. Express*, **13**, no. 19, pp. 7621–7630 (2005).
- [111] F. Röser, J. Rothhard, B. Ortac, A. Liem, O. Schmidt, T. Schreiber, J. Limpert, and A. Tünnermann. "131 W 220 fs fiber laser system". *Opt. Lett.*, **30**, no. 20, pp. 2754–2756 (2005).
- [112] T. Schreiber, F. Röser, A. Liem, H. Zellmer, and A. Tünnermann. "High average power femtosecond parabolic pulse fiber amplifier". *OSA Trends in Optics and Photonics, Advanced Solid-State Photonics*, **98** (2005).
- [113] G. Imeshev, I. Hartl, and M. E. Fermann. "Chirped pulse amplification with a nonlinearly chirped fiber Bragg grating matched to the Treacy compressor". *Opt. Lett.*, **29**, no. 7, pp. 679–681 (2004).
- [114] V. I. Kruglov, A. C. Peacock, J. M. Dudley, and J. D. Harvey. "Self-similar propagation of high-power parabolic pulses in optical fiber amplifiers". *Opt. Lett.*, **25**, no. 24, pp. 1753–1755 (2000).

- [115] V. I. Kruglov, A. C. Peacock, and J. D. Harvey. "Exact Self-similar Solutions of the Generalized Nonlinear Schrödinger Equation with Distributed Coefficients". *Phys. Rev. Lett.*, **90**, no. 113902 (2003).
- [116] M. Perry, T. Ditmire, and B. Stuart. "Self-phase modulation in chirped-pulse amplification". *Opt. Lett.*, **19**, no. 24, pp. 2149–2151 (1994).
- [117] F. Parmigiani, P. Petropoulos, M. Ibsen, and D. J. Richardson. "Pulse retiming based on XPM using parabolic pulses formed in a fiber Bragg grating". *IEEE Photon. Technol. Lett.*, **18**, no. 7, pp. 829–831 (2006).
- [118] L. Shah, Z. Liu, I. Hartl, G. Imeshev, G. C. Cho, and M. E. Fermann. "High energy femtosecond Yb cubicon fiber amplifier". **13**, no. 12, pp. 4717–4722 (2005).
- [119] R. Herda and O. G. Okhotnikov. "Dispersion compensation-free fiber laser mode-locked and stabilized by high-contrast saturable absorber mirror". *IEEE J. Quantum Electron.*, **40**, no. 7, pp. 893–899 (2004).
- [120] J. K. Ranka, R. S. Windeler, and A. J. Stentz. "Visible continuum generation in air-silica microstructured optical fibers with anomalous dispersion at 800 nm". *Opt. Lett.*, **25**, no. 1, pp. 25–27 (2000).
- [121] C. Dunsby, P. M. P. Lanigan, J. McGinty, D. S. Elson, J. Requejo-Isidro, I. Munro, N. Galletly, F. McCann, B. Treanor, B. Önfelt, D. M. Davis, M. A. A. Neil, and P. M. W. French. "An electromechanically tunable laser source applied to fluorescence imaging and fluorescence lifetime imaging microscopy". *J. Phys. D.*, **37**, no. 23, pp. 3296–3303 (2004).
- [122] T. Schreiber, J. Limpert, H. Zellmer, A. Tünnermann, and K. P. Hansen. "High average power supercontinuum generation in photonic crystal fibers". *Opt. Commun.*, **228**, no. 1-3, pp. 71–78 (2003).
- [123] W. J. Wadsworth, N. Joly, J. C. Knight, T. A. Birks, F. Biancalana, and P. S. J. Russel. "Supercontinuum and four-wave mixing with Q-switched pulses in endlessly single-mode photonic crystal fibers". *Opt. Express*, **12**, no. 2, pp. 299–309 (2004).
- [124] E. Rääkkönen, G. Genty, O. Kimmelma, M. Kaivola, K. P. Hansen, and S. C. Buchter. "Supercontinuum generation by nanosecond dual-wavelength pumping in microstructured optical fibers." *Opt. Express*, **14**, no. 17, pp. 7914–7923 (2006).
- [125] T. Schreiber, T. V. Andersen, D. Schimpf, J. Limpert, and A. Tünnermann. "Supercontinuum generation by femtosecond single and dual wavelength pumping in photonic crystal fibers with two zero dispersion wavelengths". *Opt. Express*, **13**, no. 23, pp. 9556–9569 (2005).

- [126] M. Jiang, D. J. Harter, G. D. Sussha, and M. E. Fermann. "Resonant fabry-perot semiconductor saturable absorbers and two photon absorption power limiters". *US patent*, , no. US 2001/0001006 A1 (2001).
- [127] K. W. Chang, D. K. Donald, and H. Lin. "Polarization independent picosecond fiber laser". *US patent*, , no. US 5.448.579 (1995).
- [128] M. E. Fermann and D. J. Harter. "Environmentally stable passively mod-locked fiber laser pulse source". *US patent*, , no. US 5.689.519 (1997).
- [129] M. E. Fermann and D. J. Harter. "Environmentally stable passively mod-locked fiber laser pulse source". *US patent*, , no. US 5.923.686 (1999).
- [130] M. Yoshida-Dierolf. "Operator algebra for birefringence and mirror reflection". *Opt. Commun.*, **203**, no. 1-2, pp. 79–85 (2002).
- [131] A. Yariv. "Operator algebra for propagation problems involving phase conjugation and nonreciprocal elements". *App. Opt.*, **26**, no. 21, pp. 4538–4540 (1987).
- [132] M. Martinelli. "A universal compensator for polarization changes induced by birefringence on a retracing beam". *Opt. Commun.*, **72**, no. 6, pp. 341–344 (1989).
- [133] E. P. Ippen and H. A. Haus. "Self-starting condition for additive-pulse mode-locked lasers". *Opt. Lett.*, **15**, no. 3, pp. 183–185 (1990).
- [134] H. A. Haus and E. P. Ippen. "Self-starting of passively mode-locked lasers". *Opt. Lett.*, **16**, no. 17, pp. 1331–1333 (1991).
- [135] S. V. Chernikov, Y. Zhu, J. R. Taylor, and V. P. Gapontsev. "Supercontinuum self-Q-switched Ytterbium fiber laser". *Opt. Lett.*, **22**, no. 5, pp. 298–300 (1997).
- [136] A. A. Fotiadi, R. V. Kiyan, and O. V. Shakin. "The Effect of Passive Q-switching Observed in an Erbium-Doped Fiber Laser at a Low Pumping Power". *Tech. Phys. Lett.*, **27**, no. 5, pp. 434–436 (2001).
- [137] A. A. Fotiadi, P. Mégret, and M. Blondel. "Dynamics of a self-Q-switched fiber laser with a Rayleigh-stimulated Brillouin scattering ring mirror". *Opt. Lett.*, **29**, no. 10, pp. 1078–1080 (2004).
- [138] A. Othonos and K. Kalli. *Fiber Bragg Gratings. Fundamentals and Applications in Telecommunications and Sensing..* Artech House Optoelectronics Library (1999).
- [139] D. von der Linde. "Characterization of the Noise in Continuously Operating Mode-Locked Lasers". *Appl. Phys. B*, **39**, no. 4, pp. 201–217 (1986).

- [140] C. Vinegoni, M. Wegmuller, B. Huttner, and N. Gisin. “Measurements of nonlinear polarization rotation in a highly birefringent optical fibre using a Faraday mirror”. *J. Opt. A:Pure Appl. Opt.*, **2**, no. 4, pp. 314–318 (2000).